JSCSEN 72 (7)635–735(2007)

UDC 54:66

ISSN 0352–5139

Journal of the Serbian Chemical Society 72, No. 7, 635-735 (2007)

Journal of the Serbian Chemical Society

VOLUME 72

NO 7

BELGRADE 2007

ISSN 0352–5139
J. Serb. Chem. Soc. Vol. 72, No. 7 (2007)

CONTENTS

Published by the Serbian Chemical Society
Karnegijeva 4/III, 11120 Belgrade, Serbia
Printed by the Faculty of Technology and Metallurgy
Karnegijeva 4, P.O. Box 35-03, 11120 Belgrade, Serbia

J. Serb. Chem. Soc. 72 (7) 635–641 (2007) UDC 547–304.9+547.4:615.28
JSCS–3596 *Original scientific paper*

Studies on bioactive bis-1,3,5-triazinyl dithiocarbamates

V. D. LUNAGARIYA, R. M. DESAI and V. H. SHAH*

Department of Chemistry, Saurashtra University, Rajkot–360 005, Gujarat, India

(Received 9 November 2005, revised 4 May 2007)

Abstract: The compounds bis(4,6-dichloro/bis[(*p*-methoxyphenyl)amino]-1,3,5--triazin-2-yl)1,2-hydrazine-1,2-dicarbodithioate/1,4-phenylenebis(carbamodithioate)/(1,1'-biphenyl)-4,4'-diylbis(carbamodithioate)/(sulphonyldi-4,1-phenylene)-bis(carbamodithioate/1,2-ethanediylbis(carbamothioate) **4a**–**j** were synthesized by two different methods. In the first method (**A**) for the preparation of **4a**–**e**, 2,4,6-trichloro-1,3,5-triazine **1** was condensed with diammonium 1,2-hydrazine-1,2-dicarbodithioate/1,4-phenylenebis(carbamodithioate)/(1,1'-biphenyl)-4,4'diylbis(carbamodithioate)/(sulphonyl-di-4,1-phenylene)-bis(carbamodithioate)/1,2-ethanediylbis(carbamodithioate) **3a**–**e** to afford **4a**–**e** which undergo reaction with *p*-methoxyaniline to afford **4f**–**j**. In the second method (**B**) of preparation, **1** was condensed with *p*-methoxyaniline to yield **2** followed by the action of **3a**–**e** to yield **4a**–**j**. The structure of the newly synthesized compounds **4a**–**j** was established on the basis of elemental analyses, as well as IR and ^{1}H-NMR spectroscopy. The antimicrobial activities of compounds **4a**–**j** were determined by the cup-plate method against gram-positive bacteria, gram-negative bacteria and fungi. All the synthesized compounds showed significant antimicrobial activity.

*Keywords***:** 1,3,5-triazine, dicarbamodithioates, antimicrobial activity.

INTRODUCTION

Certain dithiocarbamate derivatives have been found to possess a wide range of biological activities, *i.e*., anti-bacterial,[1] tuberculostatic,[2] anti-diuretic,[3] anti-hypertensive,[4] *etc*. *s*-Triazine derivatives also possess biological activities, such as anti-tubercular,[5] antitumor,[6] anti-cancer,[7] sedative,[8] anti-inflammatory[9] and anthelmintic[10] activities. In comparison with a previous publication on 1,3,5-triazinyl dithiocarbamates,[11] in which only one molecule of cyanuric chloride was involved in the reported molecules, a recent literature survey revealed that not a single method for the synthesis of bis(4,6-dichloro-1,3,5-triazin-2-yl) 1,2-hydrazine-1,2--dicarbodithioate **4a**, 1,4-phenylenebis(carbamodithioate) **4b**, (1,1'-biphenyl)-4,4'--diylbis(carbamodithioate) **4c**, (sulfonyldi-4,1-phenylene)bis(carbamodithioate) **4d** and 1,2-ethanediylbis(carbamodithioate) 4e, nor of bis{4,6-bis[(p-methoxyphe-

* Corresponding author. E-mail: shah_v_h@yahoo.com
doi: 10.2298/JSC0707635L

nyl)amino]-1,3,5-triazin-2-yl} esters of the respective acids (**4f–j**) has been reported to date. The present paper reports a mild and facile synthetic method for the condensation of 2,4,6-trichloro-1,3,5-triazine[12] **1** with diammonium 1,2-hydrazine-1,2-dicarbodithioate/1,4-phenylenebis(carbamodithioate)/(1,1'-biphenyl)-4,4'--diylbis(carbamodithioate)/(sulfonyldi-4,1-phenylene)bis(carbamodithioate)/1,2--ethanediylbis(carbamodithioate), followed by reaction with *p*-methoxyaniline. The compounds **4a–j** were evaluated for their biological activities against gram positive and gram negative bacteria (antibacterial activity) and fungi (antifungal activity), as possible potential biological agents. The synthesis of compounds **4a–j** can be achieved in several ways as described in the results and discussion section.

RESULTS AND DISCUSSION

In the first route (**A**), the synthesis of **4a–j** was achieved by the condensation of 1 mole of diammonium 1,2-hydrazine-1,2-dicarbodithioate/1,4-phenylene-bis-(carbamodithioate)/(1,1'-biphenyl)-4,4'-diylbis(carbamodithioate)/(sulfonyldi-4,1--phenylene)bis(carbamodithioate)/1,2-ethanediylbis(carbamodithioate) **3a–e** with 2 moles of 2,4,6-trichloro-1,3,5-triazine **1** at 0 °C in dry acetone for 3 h to afford bis(4,6-dichloro-1,3,5-triazin-2-yl) 1,2-hydrazine-1,2-dicarbodithioate/1,4-phenylene-bis(carbamodithioate)/(1,1'-biphenyl)-4,4'-diylbis(carbamodithioate)/(sulfonyldi--4,1-phenylene)-bis(carbamodithioate)/1,2-ethanediylbis(carbamodithioate) **4a–e** by the removal of 2 moles of ammonium chloride. Subsequently, the action of 4 moles of p-methoxyaniline in dry acetone at 35 °C and 58 °C for 3 h afforded **4f–j** with the removal of 2 moles of hydrochloric acid by maintaining the pH neutral through the addition of a saturated solution of sodium bicarbonate. The compounds **4f–j** were also synthesized by a second route (**B**) involving the chemical reaction between 2 moles of p-methoxyaniline with **1** in dry acetone at 0 °C and 35 °C for 3 h to afford 2,4-bis[(p-methoxyphenyl)amino]-6-chloro-1,3,5-triazine **2** by the removal of 2 moles of hydrochloric acid by maintaining the pH neutral through the addition of a saturated solution of sodium bicarbonate, followed by the action of 0.5 mole of diammonium 1,2-hydrazine-1,2-dicarbodithioate/1,4--phenylenebis(carbamodithioate)/(1,1'-biphenyl)-4,4'-diylbis(carbamodithioate)/(sulfonyldi-4,1-phenylene)bis(carbamodithioate)/1,2-ethanediylbis(carbamodithioate) **3a–e** in dry acetone at 58 °C for 3 h to afford **4f–j**, with the removal of 1 mole of ammonium chloride. A schematic representation of the reaction pathways for the synthesis of compounds **4a–j** are outlined in Scheme 1.

Synthesis of **4a–j** can be achieved by applying both the routes **A** and **B**. A theoretical mechanistic approach for the synthesis of the compounds can be found in a previously published article.[11]

The antimicrobial activity was assayed using the cup-plate agar diffusion method by measuring the zones of inhibition in mm. All the compounds were screened in vitro for their antimicrobial activity against a variety of bacterial strains. Standard drugs such as ampicillin, chloramphenicol, norfloxacin and griseofulvin were used for comparison purposes.

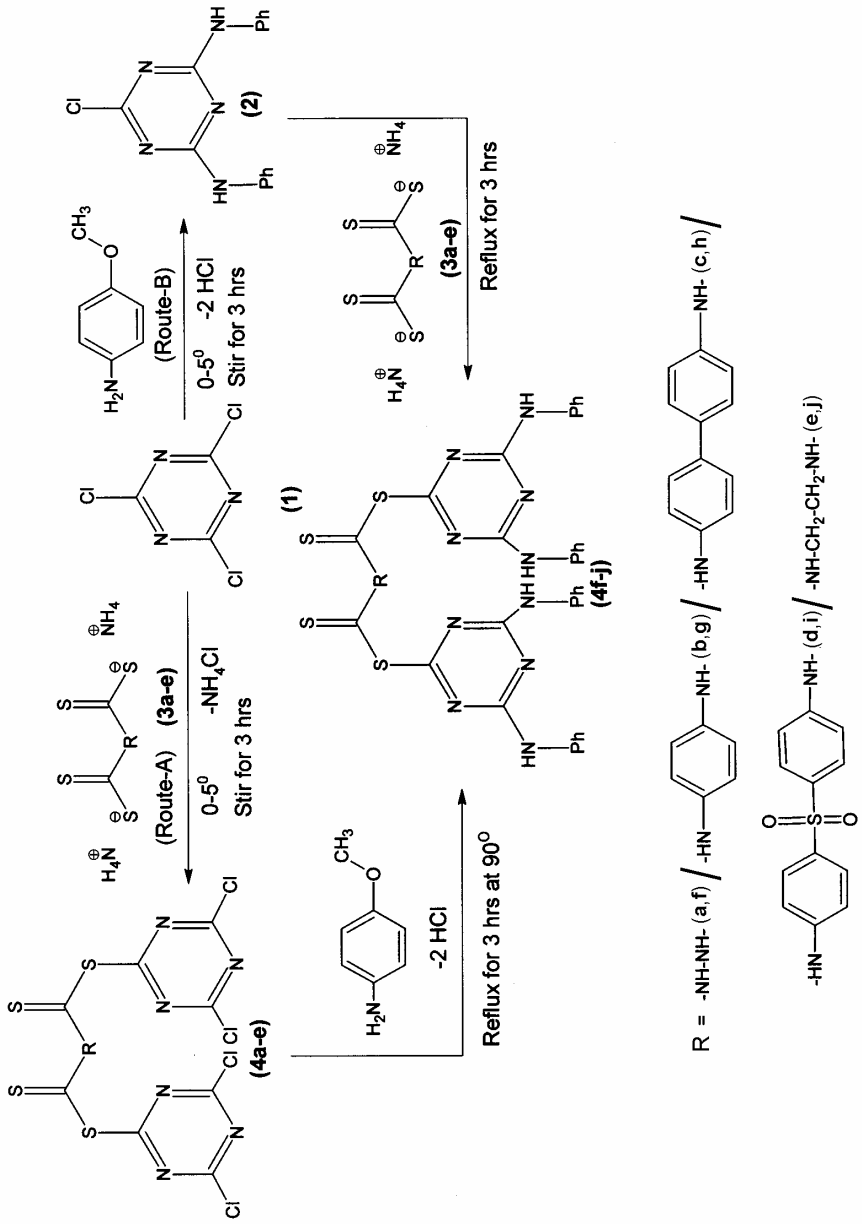
(Route-A) (3a-e) 0-5⁰ -NH4Cl Stir for 3 hrs
(Route-B) 0-5⁰ -2 HCl Stir for 3 hrs
Reflux for 3 hrs at 90⁰
-2 HCl
Reflux for 3 hrs
(4a-e)
(1)
(2)
(3a-e)
(4f-j)
R = -NH-NH- (a,f) / -HN
-NH- (b,g) / -HN
-NH- (c,h) /
-NH- (d,i) / -NH-CH2-CH2-NH- (e,j)

Scheme 1.

From the antimicrobial screening of compounds **4a**–**j**, it was observed that **4a**, **4g** and **4h** were more active than the other prepared compounds, but less active in comparison to known standard antibiotics. According to the structural activity relationship of the compounds, when R is an aromatic nucleus, the antimicrobial activity was higher with respect to the aliphatic analogues. In the case of antifungal screening, **4b** and **4i** exhibited more promising activity, whereby **4b** showed a fairly comparable antifungal activity to that of griseofulvin.

EXPERIMENTAL

The melting points of all the synthesized compounds were measured in open glass capillaries and are uncorrected. The yield is presented in percentage. The IR absorption spectra were recorded on a Shimadzu 435-IR spectrophotometer using the KBr pellet method. The ^{1}H-NMR spectra were recorded on a JEOL ^{1}H-NMR spectrophotometer (90 MHz) using TMS as the internal reference. Elemental analyses of the newly synthesized compounds were carried on a Carlo Erba 1108 analyzer and were found to be in the range of the theoretical value. The physical data and antimicrobial activity of the various compounds are presented in Tables I–III. The purity of the compounds was routinely checked by TLC using silica gel G.

Preparation of diammonium 1,2-ethanediylbis(carbamodithioate) ***3e***

A mixture of ethylenediamine (0.01 mol), carbon disulfide (0.02 mol) and ammonium hydroxide (20 ml) was vigorously stirred mechanically at 0 °C for 3 h. The obtained solid was filtered, washed with water and dried. The product was crystallized from ethanol. Yield: 83 %, m.p. 185 °C. IR (KBr) (ν / cm^{-1}): 3364 (N−H str.), 3032 (C−H str. aromatic), 2958 (C−H str. asym.), 1576 (C=S str.), 1554 (N−H str. def), 1300 (C−N str.), 705 (C−S str.); ^{1}H-NMR ($CDCl_3$) (δ / ppm): 7.58 (*s*, 2H, N−H), 2.53 (*s*, 4H, $-CH_2$).

Similarly, the other alkyl/aryl amines were stirred with carbon disulfide and ammonium hydroxide. The physical data of the obtained compounds are reported in Table I.

TABLE I. Physical data of compounds **3a**–**e**

Cpd.	Mol. formula	M.p. / °C	Yield / %	Nitrogen % (Calcd./Found)
3a	$C_2H_{10}N_4S_4$	222	80	25.68/25.65
3b	$C_8H_{14}N_4S_4$	200	82	19.05/19.00
3c	$C_{14}H_{18}N_4S_4$	280	49	15.13/15.02
3d	$C_{14}H_{14}O_2N_4S_5$	143	81	12.90/12.87
3e	$C_4H_{14}N_4S_4$	185	83	22.76/22.70

Route ***A****: Preparation of bis(4,6-dichloro-1,3,5-triazin-2-yl) 1,2-hydrazine-1,2-dicarbodithioate* ***4a***

Diammonium 1,2-hydrazine-1,2-dicarbodithioate **3a** (0.01 mol) dissolved in acetone (15 ml) was added gradually over 3 h to 2,4,6-trichloro-1,3,5-triazine **1** (0.02 mol) suspended in acetone (30 ml) at 0 °C. The obtained solid was filtered, washed with water and dried. The product was crystallized from ethanol. Yield: 72 %, m.p. 310 °C. IR (KBr) (ν / cm^{-1}): 3400 (N−H str.), 1562 (C=S str.), 1547 (N−H str. def), 1311 (C−N str.), 807 (C_3N_3 str. *s*-triazinyl), 726 (C−Cl str.), 660 (C−S str.), 682, 645 (Ar C−H out-of-plane bend); ^{1}H-NMR ($CDCl_3$)(δ / ppm): 6.58 (*s*, 2H, N−H).

Similarly, the other compounds **4b**–**e** were prepared as above. The physical data are reported in Table II.

TABLE II. Physical data of compounds **4a**–**j**

Cpd.	Mol. formula	M.p. / °C	Yield / %	Nitrogen % (Calcd./Found)
4a	$C_8H_2N_8S_4Cl_4$	310	72	23.33/23.31
4b	$C_{14}H_6N_8S_4Cl_4$	302	75	20.14/20.11
4c	$C_{20}H_{10}N_8S_4Cl_4$	307	68	17.72/17.70
4d	$C_{20}H_{10}O_2N_8S_5Cl_4$	310	72	16.09/15.95
4e	$C_{10}H_6N_8S_4Cl_4$	234	65	21.62/21.61
4f	$C_{36}H_{34}O_4N_{12}S_4$	260	68	20.33/20.32
4g	$C_{42}H_{38}O_4N_{12}S_4$	298	71	18.62/18.60
4h	$C_{48}H_{42}O_4N_{12}S_4$	259	72	17.17/17.15
4i	$C_{48}H_{42}O_6N_{12}S_5$	260	68	16.12/15.95
4j	$C_{38}H_{38}O_4N_{12}S_4$	210	65	19.44/19.42

*Preparation of bis{4,6-bis[(*p*-methoxyphenyl)amino]-1,3,5-triazin-2-yl} 1,2-hydrazine-1,2-dicarbodithioate (**4f**)*

A mixture of bis-(4,6-dichloro-1,3,5-triazin-2-yl) 1,2-hydrazine-1,2-dicarbodithioate **4a** (0.01 mol) and 4-methoxyaniline (0.04 mol) in dioxane (50 ml) was stirred for 3 h and then the mixture was refluxed for 3 h at 85–90 °C on a water bath. The content was poured onto crushed ice. The obtained solid was filtered, washed with water and dried. The product was crystallized from ethanol. Yield: 68 %, m.p. 260 °C. IR (KBr) (ν / cm^{-1}): 3404 (N–H str.), 3030 (C−H str. aromatic), 2958 (C−H str. asym.), 2921 (C−H str. CH_2), 2848 (C−H str. CH_3), 1575 (N−H str. def.), 1325 (C−N str.), 1248 (Ar−O−C str.), 818 (C_3N_3 str. *s*-triazinyl), 667 (C−S str.); ^{1}H-NMR ($CDCl_3$) (δ / ppm): 8.67 (*s*, 2H, N−H), 6.62−7.89 (*m*, 16H, Ar−H), 3.79 (*s*, 12H, −OCH_3).

Similarly, the other compounds **4f**–**j** were prepared as above. The physical data are reported in Table II.

*Route **B**: Preparation of 2-chloro-4,6-bis[(*p*-methoxyphenyl)amino]-1,3,5-triazine **2***

A mixture of 2,4,6-trichloro-1,3,5-triazine **1** (0.01 mol) and 4-methoxyaniline (0.02 mol) in dry acetone (50 ml) was stirred at 0 °C for 3 h. The content was poured onto crushed ice. The obtained solid was filtered, washed with water and dried. The product was crystallized from ethanol. Yield: 83 %, m.p. 200 °C. IR (KBr) (ν / cm^{-1}): 3350 (N−H str.), 3050 (C−H str. aromatic), 2970 (C−H str. asym. CH_3), 2850 (C−H str. sym. CH_3), 1580 (C=S str.), 1550 (N−H str. def.), 1310 (C−N str.), 1250 (Ar−O−C str.), 820 (C_3N_3 str. 1,3,5-triazinyl), 705 (C−Cl str.); ^{1}H-NMR ($CDCl_3$) (δ / ppm): 8.87 (*s*, 2H, −N−H), 6.67−7.70 (*m*, 8H, Ar−H), 3.40−4.00 (*s*, 6H, −OCH_3).

*Preparation of bis{4,6-bis[(*p*-methoxyphenyl)amino]-1,3,5-triazin-2-yl]} 1,2-hydrazine-1,2-dicarbodithioate **4f***

2-Chloro-4,6-bis[(*p*-methoxyphenyl)amino]-1,3,5-triazine **2** (0.02 mol) dissolved in dioxane was added to diammonium 1,2-hydrazine-1,2-carbodithioate **3a** (0.01 mol) suspended in dioxane (50 ml) and the mixture was refluxed on a water bath for 3 h. The content was poured onto crushed ice. The obtained solid was filtered, washed with water and dried. The product was crystallized from ethanol. Yield: 68 %, m.p. 260 °C. IR (KBr) (ν / cm^{-1}): 3404 (N−H str.), 3030 (C−H str. aromatic), 2958 (C−H str. asym.), 2921 (C−H str. CH_2), 2848 (C−H str. CH_3), 1325 (C−N str.), 1575 (N−H str. def.), 1248 (Ar−O−C str.), 818 (C_3N_3 str. 1,3,5-triazinyl), 667 (C−S str.); ^{1}H-NMR ($CDCl_3$) (δ / ppm): 8.67 (*s*, 2H, N−H), 6.62–7.89 (*m*, 16H, Ar−H), 3.79 (*s*, 12H, −OCH_3).

Similarly, the other compounds **4g**–**j** were prepared as above. The physical data are reported in Table II.

Antimicrobial activity

Compounds **4a**–**j** were screened for their antibacterial activity against *Bacillus subtilis* (MTCC-441), *Streptococcus pyogenes* (MTCC-442) (gram positive bacteria), *Escherichia coli* (MTCC-443) (gram negative bacteria) and antifungal activity against *Aspergillus niger* (MTCC-282) at a concentration of 50 μg ml^{-1} by the cup-plate method[13] using DMF as the solvent. The zone of inhibition was measured in mm and is presented in Table III.

TABLE III. Antimicrobial activity of compounds **4a**–**j**

Cpd.	Antibacterial Activity			Antifungal Activity
	B. subtilis MTCC-441	*S. pyogenes* MTCC-442	*E. coli* MTCC-443	*A. niger* MTCC-282
4a	14	18	18	16
4b	12	13	14	20
4c	15	15	13	17
4d	14	14	12	13
4e	16	15	16	12
4f	15	14	14	13
4g	18	13	18	15
4h	18	14	19	15
4i	16	18	14	18
4j	16	16	15	11
Ampicillin	22	26	24	–
Chloramphenicol	28	22	19	–
Norfloxacin	19	24	25	–
Griseofulvin	–	–	–	20

Acknowledgement: The authors are thankful to the Professor and Head, Department of Chemistry, Saurashtra University, Rajkot for providing the research facilities.

И З В О Д

ИСПИТИВАЊА БИОАКТИВНИХ БИС-1,3,5-ТРИАЗИНИЛ-ДИТИОКАРБАМАТА

V. D. LUNAGARIYA, R. M. DESAI и V. H. SHAH

Department of Chemistry, Saurashtra University, Rajkot-360 005, Gujarat, India

Две различите методе коришћене су за добијање једињења бис{4,6-дихлоро/бис[(*p*-метоксифенил)амино]-1,3,5-триазин-2-ил}-1,2-хидразин-1,2-дикарбодитиоат/1,4-фенилен-бис(карбамодитиоат)/(1,1'-бифенил)-4,4'-диил-бис(карбамодитиоат)/(сулфонил-ди-4,1-фенилен)-бис(карбамодитиоат)/1,2-етан-диил-бис(карбамодитиоат) **4a**–**j**. У првом методу (**A**) за припрему **4a**–**e**, 2,4,6-трихлоро-1,3,5-триазин **1** кондензован је са диамонијум-1,2-хидразин-1,2-дикарбодитиоатом/1,4-фенилен-бис(карбамодитиоатом)/(1,1'-бифенил)-4,4'-диил-бис(карбамодитиоатом)/(сулфонил-ди-4,1-фенилен)-бис(карбамодитиоатом)/1,2-етан-диил-бис(карбамодитиоатом) **3a**–**e** да би се добили **4a**–**e,** који подлежу реакцији са *p*-метоксианилином чиме се добијају **4f**–**j**. У другој методи добијања (**B**), **1** је кондензован са *p*-метоксианилином да би се добио **2** уз накнадно учешће **3a**–**e** да би се добили **4a**–**j**. Структуре новодобијених једињења **4a**–**j** установљене су на основу елементалне анализе, као и IR и ^{1}H-NMR спектро-

скопијама. Антимикробне активности једињења **4a**–**j** на грам-позитивне и грам-негативне бактерије и гљиве одређене су методом бунарчића у агару. Сва добијена једињења показала су знатну антимикробну активност.

(Примљено 9. новембра 2005, ревидирано 4.маја 2007)

REFERENCES

1. V. H. Shah, N. A. Chauhan, A. R. Parikh, *J. Inst. Chem.* **59** (1987) 249
2. V. Gvozdakova, Z. Oderova, T. Gogh, *Chem. Zvesti* **33** (1979) 129; *C. A.* **91** (1979) 102808r
3. M. L. Korablav, M. A. Events, *Farmakol. Toksikol*. **40** (1977), 603 (in Russian); *C. A.* **87** (1977) 177859j
4. I. Matusumoto, J. Yoshizawa, H. Hidaka, JP51105073, **76** (1976); *C.A.* **86** (1977) 89610v
5. N. A. Langalia, K. A. Thaker, *J. Indian Chem. Soc.* **59** (1982) 1099; *C. A.* **98** (1983) 89321z
6. D.–C. Thang, N. Hoang–Nam, H. Hellinger, L. Puchat, *J. Labelled Compd. Radiopharm.* **20** 779–83; *C. A.* **99** (1983) 212500g
7. Andereoli Rovati, Ramao, Lloveras Parera, Pere, Rius Palleiro, Javier, Mendleta Cadena, Luis *Span. Es.* **510** (1983) 970
8. A. Kreutzberger, M. Loch, *Arch. Pharm*. **319** (1986) 275; *C. A.* **105** (1983) 6439w
9. A. S. Tomfuck, A. E. Sloboda, (American Cyanamid Co) USP 4261, 892; **95** (1981) 62269
10. Z. Budensinsky, J. Sluka, J. Navak, Zech CS, 193, 949, (1982); *C. A.* **96 (**1982) 181315g
11. R. M. Desai, N. R. Ravat, V. H. Shah, *Indian J. Chem.* **43B** (2004) 367
12. A. Serullas, *Ann. Chim. Phys.* **38** (1928) 379
13. A. L. Barry, *The Antimicrobic susceptibility test, Principle and Practices* 4^{th} *ed.*, ELBS, London; (1976) p. 180.

J. Serb. Chem. Soc. 72 (7) 643–654 (2007) UDC 547.822:544.021+66.011:615:519.876.5
JSCS–3597 *Original scientific paper*

Location of the hydrophobic pocket in the binding site of fentanyl analogs in the μ-opioid receptor

LJILJANA DOŠEN–MIĆOVIĆ*#, MILOVAN IVANOVIĆ# and VUK MIĆOVIĆ#

Faculty of Chemistry, University of Belgrade, Studentski trg 16, P.O.Box 158, 11000 Belgrade and Center for Chemistry, ICTM, 11000 Belgrade, Serbia

(Received 20 June 2006, revised 20 February 2007)

Abstract: Fentanyl is a highly potent and clinically widely used narcotic analgesic. The synthesis of its analogs remains a challenge in an attempt to develop highly selective μ-opioid receptor agonists with specific pharmacological properties. In this paper, the use of flexible molecular docking of several specific fentanyl analogs to the μ-opioid receptor model, in order to test the hypothesis that the hydrophobic pocket accommodates alkyl groups at position 3 of the fentanyl skeleton, is described. The stereoisomers of the following compounds were studied: *cis*- and *trans*-3-methylfentanyl, 3,3-dimethylfentanyl, *cis*- and *trans*-3-ethylfentanyl, *cis*- and *trans*-3-propylfentanyl, *cis*-3-isopropylfentanyl and *cis*-3-benzylfentanyl. The optimal position and orientation of these fentanyl analogs in the binding pocket of the μ-receptor, explaining their enantiospecific potency, were determined. It was found that the 3-alkyl group of *cis*-3*R*,4*S* and *trans*-3*S*,4*S* stereoisomers of all the active compounds occupies the hydrophobic pocket between TM5, TM6 and TM7, made up of the amino acids Trp318 (TM7), Ile322 (TM7), Ile301 (TM6) and Phe237 (TM5). However, the fact that this hydrophobic pocket can also accommodate the bulky 3-alkyl substituents of the two inactive compounds: *cis*-3-isopropylfentanyl, and *cis*-3-benzylfentanyl, indicates that this hydrophobic pocket in the employed receptor model is probably too large.

Keywords: molecular modeling, fentanyl analogs, ligand–receptor interactions, docking simulation

INTRODUCTION

The exceptional opioid analgesic activity of fentanyl (**1**) and its analogs has been well documented in the past forty years.[1] Combined with various anesthetics, they have been employed in surgeries under general anesthesia, to manage postoperative pain and in transdermal patches to control chronic cancer pain.[2,3] Some, such as carfentanil, are in use as veterinary analgesics for the sedation of wild animals. Numerous fentanyl analogs have been synthesized[4] as potential can-

* Corresponding author. E-mail: lmicovic@chem.bg.ac.yu
# Serbian Chemical Society member.
doi: 10.2298/JSC0707643D

didates for novel drugs but the synthesis of the new analogs remains a challenge because drugs with specific pharmacological properties and with minimal side effects are required.

Molecular modeling of drug–receptor interactions assisted in identifying major functional groups participating in drug–receptor interactions. This may be useful as leading information in a synthesis of new, more specific drugs with increased potency. Modeling may also determine the position of a drug molecule in a receptor and identify the major amino acids participating in the formation of a drug–receptor complex, thus suggesting possible mechanisms of drug action.

In a previous paper,[5] flexible molecular docking was used to study complexes between series of active fentanyl analogs and the μ-opioid receptor. The optimal position and orientation of the fentanyl analogs in the binding pocket were determined. The model explained the high enantiospecific potency and binding of some fentanyl analogs in the binding pocket.

In this paper, flexible molecular docking of the 3-substituted fentanyl analogs **1** to **10** to the model of a μ-opioid receptor is employed in order to test the hypothesis of the hydrophobic pocket in the binding site which accommodates alkyl groups at position 3 of the fentanyl skeleton, Table I.

TABLE I. The studied fentanyl analogs

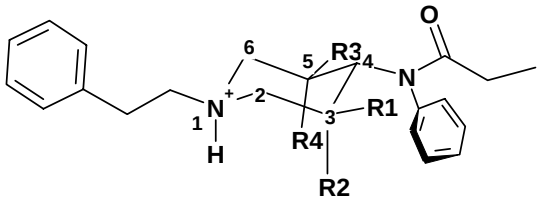

	Compound	R1	R2	R3	R4
1	Fentanyl	H	H	H	H
2	*cis*-3-Methylfentanyl				
	3*R*,4*S*	H	CH_3	H	H
	3*S*,4*R*	H	H	H	CH_3
3	*trans*-3-Methylfentanyl				
	3*S*,4*S*	CH_3	H	H	H
	3*R*,4*R*	H	H	CH_3	H
4	3,3-Dimethylfentanyl				
	4*S*	CH_3	CH_3	H	H
	4*R*	H	H	CH_3	CH_3
5	*cis*-3-Ethylfentanyl				
	3*R*,4*S*	H	CH_2CH_3	H	H
	3*S*,4*R*	H	H	H	CH_2CH_3

TABLE I. Continued

6	*trans*-3-Ethylfentanyl				
	3*S*,4*S*	CH_2CH_3	H	H	H
	3*R*,4*R*	H	H	CH_2CH_3	H
7	*cis*-3-Propylfentanyl				
	3*R*,4*S*	H	$CH_2CH_2CH_3$	H	H
	3*S*,4*R*	H	H	H	$CH_2CH_2CH_3$
8	*trans*-3-Propylfentanyl				
	3*S*,4*S*	$CH_2CH_2CH_3$	H	H	H
	3*R*,4*R*	H	H	$CH_2CH_2CH_3$	H
9	*cis*-3-Isopropylfentanyl				
	3*R*,4*S*	H	$CH(CH_3)_2$	H	H
	3*S*,4*R*	H	H	H	$CH(CH_3)_2$
10	*cis*-3-Benzylfentanyl				
	3*R*,4*S*	H	$CH_2C_6H_5$	H	H
	3*S*,4*R*	H	H	H	$CH_2C_6H_5$

The μ-opioid receptor is the primary site of action in the brain for opioid drugs. It is a member of the seven trans-membrane (TM) domains, G protein-coupled (GPCR) receptor superfamily, which are believed to share a common topology and a common mechanism of action. Their 3D structures are at present unknown. One hypothesis [6,7] suggests an agonist binding to G protein-coupled receptors promotes a conformational change which leads to the formation of the activated receptor state. Another hypothesis[8] suggests that a rigid body movement of helices relative to one another is the key step in receptor activation. However, the character of these changes, which link agonist binding and G protein coupling and activation, is not known. It is a subject of intensive modeling[9] and experimental studies, including receptor cloning, site-directed mutagenesis and affinity labeling studies.[10]

Therefore, in order to obtain detailed insight into the key interactions between a ligand and a receptor, molecular models, based on bacteriorhodopsin or rhodopsin templates, of various GPCRs have been developed.[6,9a,9b] Despite inherent difficulties in modeling opioid receptors at the molecular level, several models of μ-opioid receptor are available.[9d,9i,11–13] The earlier studies[9d,9k,11] used "manual docking" to a predefined binding cavity[9k,11] or rigid ligand docking.[9d] The resultant bound conformation and orientation of *cis*-3-methylfentanyl were different in these studies. In our own previous study,[5] flexible molecular docking was used to define the optimal position and orientation of fentanyl analogs in the binding pocket of a μ-opioid receptor and to explain their enantiospecific potency and binding.

In this study, another sequence of fentanyl analogs, Table I, were flexibly docked to a model of the human μ-receptor. The goal was to evaluate the binding orien-

tations and conformations of compounds **1** to **10** and to test the hypothesis of the hydrophobic pocket existing in the receptor which accomodates the 3-alkyl group of a ligand. The results were compared to the available experimental data, Table II.

TABLE II. Experimental potencies (relative to fentanyl) of **1**–**10** for the μ-opioid receptor

Name	Compound	Potency[a]
Fentanyl	**1**	1
cis-3-Methylfentanyl	(±)-**2**	6.1
	(3*R*,4*S*)-**2**	19
	(3*S*,4*R*)-**2**	0.16
trans-3-Methylfentanyl	(±)-**3**	1.17
	(3*S*,4*S*)-**3**	3.3
	(3*R*,4*R*)-**3**	0.8
3,3-Dimethylfentanyl	**4**	nd[b]
cis-3-Ethylfentanyl	(±)-**5**	1.49
trans-3-Ethylfentanyl	(±)-**6**	0.9
cis-3-Propylfentanyl	(±)-**7**	0.55
trans-3-Propylfentanyl	(±)-**8**	0.27
cis-3-Isopropylfentanyl	(±)-**9**	inactive
cis-3-Benzylfentanyl	(±)-**10**	0.0079

[a]Ref. 21, unless otherwise stated; [b]nd–not determined.

COMPUTATIONAL METHODS

All computations were performed using a P4/Celeron at 1.5 GHz. The μ-receptor model used in this study was the one built by Ferguson and co-workers,[9d] and kindly made available through www.opiod.umn.edu. The rigid receptor model was used. The automated flexible ligand docking experiments were made with the AutoDock 3.0.5 program.[14] The starting geometries of the neutral ligands were taken from previous studies.[15a,b] The geometries satisfy the suggested fentanyl pharmacophore,[15] by having the piperidine ring in the chair conformation, the *N*-phenethyl and *N*-phenylpropanamide substituents both equatorial and the anilido phenyl α-oriented. The amide bond had the *trans* configuration and the *N*-phenethyl substituent adopted an extended conformation, Table I. Based on the pK_a values of several fentanyl derivatives,[16] the starting geometries were protonated and the protonated geometries of compounds **1**–**10** were optimized using the semi-empirical AM1 method of the HyperChem program.[17] The Gasteiger charges were assigned to the ligand automatically by the AutoDock program. The 60×60×60 grid was centered on one of the Asp147 oxygen atoms and the Lamarckian genetic algorithm (LGA) was used in all docking calculations. The docking process was performed in two steps. In the first short step, consisting of 200 LGA runs, the initial position of the ligand was random. The population was 50, the maximum number of generations was 27,000 and the maximum number of energy evaluations was limited to 250,000. The best ligand orientation in the first step, based on the score criteria, was used as the input position for the second docking step, where the number of energy evaluations was 2.5×10^6. The second step provided the most probable ligand geometries and orientations in the binding pocket. The resultant ligand orientations and conformations were scored based on the docking and binding energies, and on the distance of Asp147 to the protonated nitrogen of the ligand. The cut-off value for the energies was 8.4 kJ mol^{-1}, and the cutoff value for the distance was 0.45 nm. Site-directed mutagenesis studies[18] have shown that Asp147 to Ala/Asn or Glu point mutations lead to di-

minished binding affinities, presumably due to the loss of a salt bridge or an electrostatic interaction between the negatively charged Asp147 and the protonated nitrogen of the ligand.

RESULTS AND DISCUSSION

As was described in a previous paper,[5] automated docking of some active analogs of fentanyl to the TM domain of the μ-opioid receptor resulted in several plausible docking orientations and conformations for each ligand. The resulting ligand orientations and conformations were scored based on the docking and binding energies and the distance between Asp147 and the protonated nitrogen of the ligand and only a few met the criteria and they were further evaluated based on experimental results indicating the important amino acids constituting the ligand binding site within the receptor.

The best fentanyl (**1**) docking orientation positions the piperidine ring nearly perpendicular to the membrane surface in the region between transmembrane helices TM3, TM5, TM6 and TM7. The protonated nitrogen is close to Asp147 of TM3 (the HN^+–O^- distance is 0.34 nm). The *N*-phenylpropanamide group is oriented toward the extracellular side of the cavity, while the *N*-phenethyl group adopts a *gauche* conformation, placing the phenyl group between TM6 and TM7. This position and orientation of a ligand in the binding pocket of the μ-opioid receptor has been supported by a number of site directed mutagenesis experiments.[5] All the other active analogs of fentanyl studied here adopted very similar conformations and alignments in the binding pocket, Figs. 1 and 2.

It is interesting to note that the results of our studies of the docking of fentanyl analogs to the other available model of the μ-opioid receptor[20] confirmed the location of the binding pocket in the region between the trans-membrane helices TM3, TM5, TM6 and TM7, as well as the position and orientation of the fentanyl ligands within the binding pocket. This adds support to our model of binding of fentanyl analogs and of the activation of the μ-opioid receptor.

*3-Methylfentanyls (**2,3**)*

Substitution at position 3 of the piperidine ring produced some of the most potent fentanyl analogs. The (3*R*,4*S*)-*cis*-3-methylfentanyl, (3*R*,4*S*)-**2**, is about twenty times more potent than fentanyl. However the potency of 3-alkylfentanyls is highly stereosensitive, hence the (3*S*,4*S*)-*trans* isomer, (3*S*,4*S*)-**3**, is only three times more active than fentanyl, while the (3*S*,4*R*)-**2** and (3*R*,4*R*)-**3** are both less active than fentanyl. The potency is known to depend on the size of the alkyl group: 3-propyl- and 3-allyl- substitution leads to diminished activity,[1a] suggesting the existence of a small hydrophobic pocket in the receptor. According to previous docking studies,[5] the geometries of the three isomers of low potency, (3*S*,4*R*)-**2**, (3*S*,4*S*)-**3** and (3*R*,4*R*)-**3**, in the binding pocket are very similar and overlap the "best" fentanyl orientation, while the most potent of the 3-methylfentanyls, (3*R*,4*S*)-**2,** is different.

The molecule of (3*S*,4*S*)-**3** overlaps that of fentanyl and places the equatorial 3-methyl group toward the hydrophobic pocket surrounded by Trp318 (TM7), Ile322 (TM7), Ile301 (TM6) and Phe237 (TM5), *i.e.*, between the transmembrane helices TM5, TM6 and TM7. It was found earlier[5] that Ile 322 in TM7 is the key residue for discrimination among the stereoisomers of 3-methylfentanyl. Its location near the 3-H_{ax} in the "best" fentanyl orientation makes this orientation inaccessible to any analog with a voluminous subsistent at the 3-*ax* position, forcing such a molecule to adopt a different orientation. The increased potency of the (3*S*,4*S*)-**3** isomer, relative to fentanyl, is probably due to the favorable hydrophobic interactions of the methyl group in the pocket.

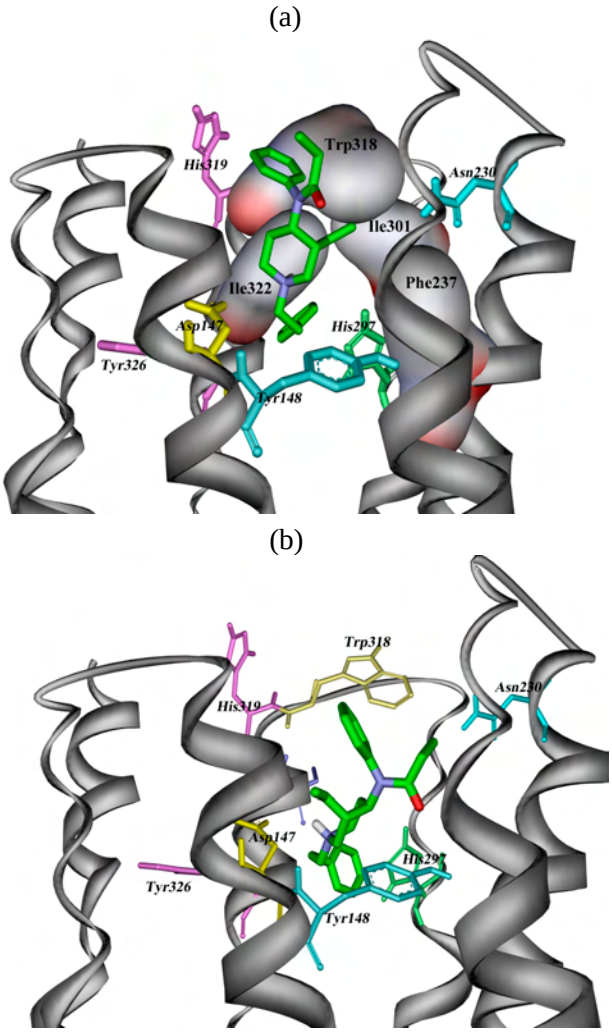

Fig. 1. The two enantiomers of *cis*--3-ethylfentanyl (**5**) in the binding pocket: a) (3*R*,4*S*)-**5**; b) (3*S*,4*R*)-**5**.

The two least active 3-methylfentanyls, the (3*S*,4*R*)-**2** and the (3*R*,4*R*)-**3**, overlap the "best" fentanyl orientation but the 3-methyl group is oriented away from the hydrophobic pocket and towards Asp147, with which it has unfavorable steric interactions.

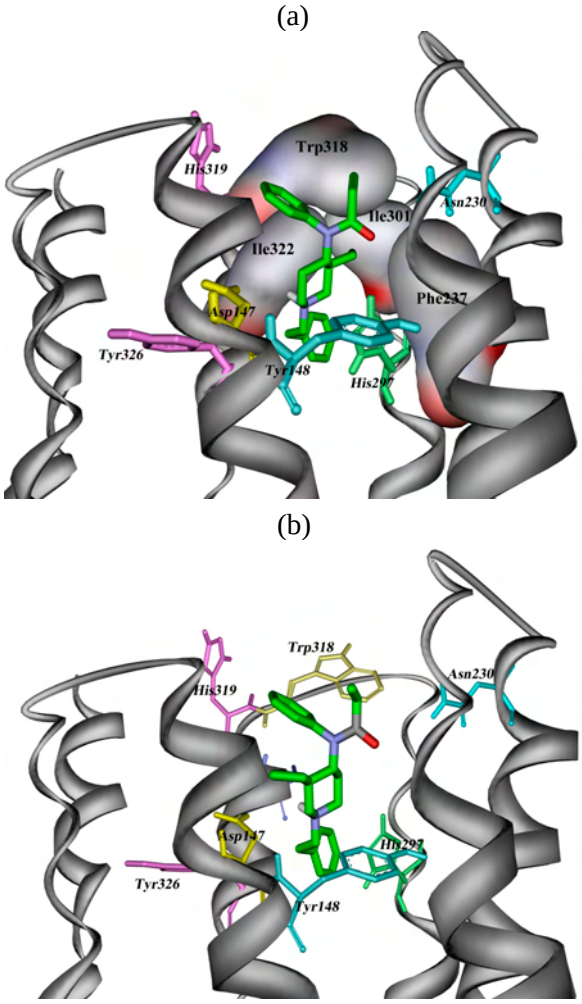

Fig. 2. The two enantiomers of *trans*--3-ethylfentanyl (**6**) in the binding pocket: a) (3*S*,4*S*)-**6**; b) (3*R*,4*R*)-**6**.

The most potent of the four stereoisomers is (3*R*,4*S*)-**2**. Although it occupies the same binding pocket as the other three isomers, it is rotated and shifted[5] relative to the other three isomers, in order to relieve the steric interactions of the axial 3-methyl group and Ile322 (TM7) in the hydrophobic pocket between helices TM5, TM6 and TM7. While maintaining a good salt bridge (HN^+–O^- distance 0.373 nm), a molecule in this orientation connects TM3 and TM6 through the *N*-phenethyl group, which has favorable edge-to-face interactions with the imidazole ring

in His297 (TM6). Simultaneously, the *N*-phenylpropanamide phenyl group is much closer to Trp318 (TM7) and His319 (TM7) than in the case of fentanyl itself. Considering the importance of the boundary region between TM6, TM7 and the third extracellular loop for both activity and selectivity of opioid ligands, this proximity explains the exceptional potency of this isomer of 3-methylfentanyl.

*3,3-Dimethylfentanyl (**4**)*

Although 3,3-dimethylfentanyl was synthesized,[19] its pharmacological activity and binding constant have never been determined. Both enantiomers 4*S* and 4*R* of 3,3-dimethylfentanyl were considered in the docking studies reported here. The position and orientation of (4*S*)-**4** in the binding pocket is similar to the most potent of the 3-methylfentanyl isomers, (3*R*,4*S*)-**2**. (4*R*)-**4** is similar to the other three, less potent 3-methylfentanyl isomers and to fentanyl itself. Therefore, it is to be expected that (4*R*)-**4** would have a potency comparable to that of fentanyl, and that (4*S*)-**4** would be even more active.

However, the present major goal was to investigate the binding profile of ligands with voluminous 3-alkyl substituents, in order to confirm the position and to determine the size of the hydrophobic pocket in the binding site of the fentanyl analogs in the μ-opioid receptor.

*3-Ethylfentanyl (**5,6**)*

As with the 3-methylfentanyls, the *cis* isomer (**5**) of the 3-ethylfentanyl is more active than the *trans* isomer (**6**), Table II. One of the two enantiomers of **5**, (3*R*,4*S*)-**5,** Fig. 1a, has the same position and orientation in the binding pocket as the most potent of the stereoisomers of 3-methylfentanyl, (3*R*,4*S*)-**2,** with the 3-ethyl group extending deep into the hydrophobic pocket and toward Asn230. The position and orientation of (3*S*,4*R*)-**5** resembles that of fentanyl (**1**), Fig. 1b. This means that, as in the case of 3-methylfentanyl, the (3*R*,4*S*)-**5** isomer is expected to be the more potent of the two *cis* stereoisomers of 3-ethylfentanyl. The position and orientation of the two *trans* isomers of 3-ethylfentanyl (**6**) in the binding pocket are close to that of fentanyl (**1**), Fig. 2. Therefore they are expected to have activities comparable to that of fentanyl.

*3-Propylfentanyl (**7,8**)*

The molecule of (3*R*,4*S*)-**7** has two orientations in the binding pocket with nearly equal energies. One is similar to the position of the highly potent (3*R*,4*S*)-**2** and the other one to the position of fentanyl. This may be the reason for the reduced potency of **7** relative to **2** and **5**. The other reason for the low potency of **7** is inability of (3*S*,4*R*)-**7** to adopt a fentanyl-like orientation, *i.e.*, an active orientation because of the steric bulk of the *n*-propyl group and its steric interactions with Asp147. Yet another reason for the diminished potency of **7** may be the size of the *n*-propyl group, which is probably too big compared to the size of the hy-

drophobic pocket. However, this was not obvious from our calculations where the *n*-propyl group, adopting *gauche* conformation, fits well to the relatively big hydrophobic pocket surrounded by the trans-membrane helices TM5, TM6 and TM7.

In the case of the *trans* isomer of 3-propylfentanyl (**8**), the (3*S*,4*S*)-**8** enantiomer adopts a fentanyl-like orientation. However, the complete inability of the other enantiomer (3*R*,4*R*)-**8** to adopt any fentanyl-like orientation in the binding pocket may be the reason for the measured low activity of **8**, which is about three times less active than fentanyl.

*3-Isopropylfentanyl (**9**) and 3-benzylfentanyl (**10**)*

As the *cis* isomers are the more potent stereoisomers of the known 3-alkylfentanyls, the pharmacological activities of only *cis*-3-isopropylfentanyl (**9**) and *cis*-3-benzylfentanyl (**10**) were determined.[19] Both were inactive or had very low activity, Table II.

According to the docking studies, (3*S*,4*R*)-**9** and (3*S*,4*R*)-**10** cannot adopt any fentanyl-like orientation due to steric crowding. Thus, they cannot be active according to our model. However, (3*R*,4*S*)-**9** and (3*R*,4*S*)-**10** adopt a position and orientation in the binding pocket similar to those of a molecule of the very potent (3*R*,4*S*)-**2**. Therefore their experimentally determined lack of activity was unexpected. The reason for this discrepancy might be the high values of log*P* for these compounds, especially for compound **10**, which may affect the bioavailability of a compound. However, compounds **7** and **9** have similar values of log*P* and yet different potencies. Another reason might be the oversized hydrophobic pocket in the employed receptor model, which would enable the accommodation of even bulky substituents, such as an isopropyl or a benzyl group. The oversized hydrophobic pocket may be the consequence of *in vacuo* modeling of the receptor structure. According to recent work[22] on simulations of the molecular dynamics of the μ-opioid receptor in a membrane–aqueous system, the arrangement of the α-helices of the transmembrane receptor domain became more compact relative to an isolated receptor. The atoms in the upper portion of TM3, TM5 and TM6 shifted inward from 0.02 to 0.38 nm, yielding a more compact binding pocket.

CONCLUSION

In the present study an automated docking procedure was applied in order to determine the optimal position and orientation of the ten fentanyl analogs in the binding pocket of the μ-opioid receptor, and to confirm the existence of the hydrophobic pocket accommodating the non-polar substituents at position 3 of the fentanyl skeleton. The quality of the model of the receptor–ligand complexes was estimated on the basis of their binding and docking energies, the distance between Asp147 (TM3) and the protonated amine nitrogen of the ligand, and the agreement with point-mutation experimental data, as described earlier.[5]

It was shown that all the active compounds occupy the same binding pocket in the receptor, located near the extracellular region and between the transmembrane helices TM3 to TM7. The ligand molecule is parallel to the transmembrane helices, with the 4-phenylpropanamide group pointing to the extracellular region and the *N*-phenethyl group placed deep in the pocket in the region between TM6 and TM7.

3-Alkyl substituted fentanyl stereoisomers with the 4*R* configuration and the alkyl substituent bulkier than the ethyl group cannot adopt a fentanyl-like orientation due to steric crowding, and, according to our model, cannot be active.

3-Alkyl substituted fentanyl stereoisomers with the 4*S* configuration can adopt a fentanyl-like, active orientation. All the 3-alkyl substituents of the stereoisomers with 4*S* configuration occupy the same hydrophobic pocket located between TM5, TM6 and TM7, and surrounded by the amino acids Trp318 (TM7), Ile322 (TM7), Ile301 (TM6) and Phe237 (TM5). However, in the employed receptor model, this hydrophobic pocket seems to be too large, accommodating even bulky groups such as isopropyl and benzyl and suggested that 3-isopropyl and 3--benzylfentanyl could be moderately active.

Acknowledgement: This work was supported by the Ministry of Science and Environmental Protection of the Republic of Serbia, project No.142074.

И З В О Д

ПОЛОЖАЈ ХИДРОФОБНОГ МЕСТА ЗА ВЕЗИВАЊЕ АНАЛОГА ФЕНТАНИЛА ЗА μ-ОПИОИДНИ РЕЦЕПТОР

ЉИЉАНА ДОШЕН–МИЋОВИЋ, МИЛОВАН ИВАНОВИЋ и ВУК МИЋОВИЋ

Хемијски факултет, Универзитет у Београду, Студентски трг 16, п.пр. 158, 11000 Београд и Центар за хемију, ИХТМ, 11000 Београд

Фентанил је наркотички аналгетик високе активности и широке клиничке примене. Добијање његових аналога, у смислу да се развију високо селективни агонисти μ-опиоидног рецептора одређених фармаколошких својстава, и даље је изазов, како за експерименталну тако и за теоријску хемију. У овом раду описано је флексибилно уклапање молекула неколико аналога фентанила у μ-опиоидни рецептор, у циљу провере претпоставке да у скелету рецептора постоји хидрофобно место које прихвата алкил групе у положају 3 код аналога фентанила. Испитивани су стереоизомери следећих једињења: *cis*- и *trans*-3-метилфентанил, 3,3-диметилфентанил, *cis*- и *trans*-3-етилфентанил, *cis*- и *trans*-3-пропилфентанил, *cis*-3-изопропилфентанил и *cis*-3-бензилфентанил. Одређени су оптимални положај и оријентација ових аналога фентанила у месту везивања у μ-рецептору који објашњавају њихову енантиоспецифичну активност. Нађено је да 3-алкил група *cis*-3*R*,4*S* и *trans*-3*S*,4*S* стереоизомера свих активних једињења заузима хидрофобно место између TM5, TM6 и TM7, које чине аминокиселине Trp318 (TM7), Ile322 (TM7), Ile301 (TM6) и Phe237 (TM5). Међутим, чињеница да ово хидрофобно место може да прихати и волуминозне 3-алкил супституенте два неактивна једињења, *cis*-3-изопропилфентанила и *cis*-3-бензилфентанила, указује на то да је оно у случају коришћеног модела рецептора вероватно веће него у природном рецептору.

(Примљено 20. јуна 2006, ревидирано 20. фебруара 2007)

REFERENCES

1. a) A. F. Casy, R. T. Parfitt, *Opioid Analgesics*, Plenum Press, New York, 1986, pp. 287–301; b) A. F. Casy, "Opioid Receptors and Their Ligands"in *Advances in Drug Research*, B. Testa, Ed., Vol 18, Academic Press, London, 1980, pp. 178–272; c) M. Williams, E. A. Kowaluk, S. P. Americ, *J. Med. Chem*. **42** (1999) 1481
2. G. Capogna, M. Camorcia, M. O. Columg, *Anesth. Analg*. **96** (2003) 1178
3. a) W. Jeal, P. Benfield, *Drugs* **53** (1997) 109; b) http://www.duragesic.com
4. V. D. Kiricojević, M. D. Ivanović, I. V. Mićović, J. B. Djordjević, G. M. Roglić, Lj. Došen–Mićović, *J. Serb. Chem. Soc.* **67** (2002) 793; b) I. V. Mićović, M. D. Ivanović, S. M. Vučković, M. Š. Prostran, Lj. Došen–Mićović, V. D. Kiricojević, *Bioorg. Med. Chem. Lett.* **10** (2000) 2011; c) I. V. Mićović, M. D. Ivanović, S. M. Vučković, D. Jovanović–Mićić, D. Beleslin, Lj. Došen–Mićović, V. D. Kiricojević, *Heterocyclic Commun*. **4** (1998) 171 and references cited therein; d) I. V. Mićović, G. M. Roglić, M. D. Ivanović, Lj. Došen–Mićović, V. D. Kiricojević, J. B. Djordjević, *J. Chem. Soc., Perkin Trans. 1* (1996) 2041; e) U.S. Patent 5,489,689 (1996); f) U.S. Patent 4,179,569 (1979); g) Van Daele, M. F. L. DeBruyn, J. M. Boey, S. Sanczuk, J. T. M. Agten, P. A. J. Janssen, *Arzneim-Forsch. (Drug. Res.)* **26** (1976) 1521; h) L. V. Kudzma, S. A. Sevemak, M. J. Benvenga, E. F. Ezell, M. H. Ossipov, V. V. Knight, F. G. Rudo, H. K. Spencer, T. C. Spaulding, *J. Med. Chem*. **32** (1989) 2534; i) M. D. Ivanović, *Ph.D. Thesis*, Chemistry Dept., University of Belgrade, 1998 (in Serbian)
5. Lj. Došen–Mićović, M. Ivanović, V. Mićović, *Bioorg. Med. Chem.* **14** (2006) 2887, and references therein.
6. J. A. Bikker, S. Trumpp–Kallmeyer, C. Humblet, *J. Med. Chem*. **41** (1998) 2911, and references therein.
7. a) Z. X. Wang, Y. C. Zhu, W. Q. Jin, X. J. Chen, C. Jie, R.Y. Ji, Z. Q. Chi, *J. Med. Chem.* **38** (1995) 3652; b) Y. F. Lu, H. Xu, L. Y. Liu–Chen, C. Chen, J. Partilla, G. A. Brine, F. I. Carroll, K. C. Rice, J. Lai, F. Porreca, W. Sadee, R. B. Rothman, *Synapse* **28** (1998) 117
8. D. L. Farrens, C. Altenbach, K. Yang, W. L. Habbell, H. G. Khorana, *Science* **274** (1996) 768
9. a) A.G. Beck–Sickinger, *Drug Discovery Today* **1** (1996) 502; b) D. R. Flowe, *Biochim. Biophys. Acta* **1422** (1999) 207; c) G. Subramanian, M. G. Paterlini, P. S. Portoghese, D. M. Ferguson, *J. Med. Chem*. **41** (1998) 4777; d) G. Subramanian, M. G. Paterlini, D. L. Larson, P. S. Portoghese, D. M. Ferguson, *J. Med. Chem.* **43** (2000) 381; e) A. Lavecchia, G. Greco, E. Novellino, F. Vittorio, G. Ronsisvalle, *J. Med. Chem*. **43** (2000) 2124; f) H. I. Mosberg, C. B. Fowler, *J. Peptide Res*. **60** (2002) 329; g) M. Aburi, P. E. Smith, *Protein Sci.* **13** (2004) 1997; h) I. D. Pogozheva, A. L. Lomize, H. I. Mosberg, *Biophys. J.* **72** (1997) 1963; i) M. Filizola, M. Carteni-Farina, J. J. Perez, *J. Comput.-Aided Mol. Design* **12** (1998) 111; j) J. Li, P. Huang, C. Chen, J. K. de Riel, H. Weinstein, L.-Y. Liu-Chen, *Biochemistry* **40** (2001) 12039; k) H. L. Jiang, X. Q. Huang, S. B. Rong, X. M. Luo, J. Z. Chen, Z. Tang, K. X. Chen, Z. C. Zhu, W.Q. Jin, Z. Q. Chi, Y. J. Ru, Y. Cao, *Int. J. Quantum Chem.* **78** (2000) 285
10. a) H. Kong, K. Raynor, K. Yasuda, S. T. Moe, P. S. Portoghese, *J. Biol. Chem.* **286** (1993) 23055; b) C. K. Surratt, P. S. Johnson, A. Moriwaki, B. K. Seidleck, C. J. Blaschak, J. B. Wang, G. R. Uhl, *J. Biol. Chem*. **269** (1994) 20548; c) J. Zhu, J.–C. Xue, P.–Y. Law, P. A. Claude, L.–Y. Luo, J.–L. Yin, C.–G. Chen, L.–Y. Liu–Chen, *FEBS Lett.* **384** (1996) 198; d) J. Heerding, K. Raynor, H. Kong, L. Yu, T. Reisine, *Reg. Pept.* **54** (1994) 119
11. I. D. Pogozheva, A. L. Lomize, H. I. Mosberg, *Biophys. J.* **75** (1998) 612
12. J. McFadyen, T. Metzger, G. Subramanian, G. Poda, E. Jorvig, D. M. Ferguson, *Prog. Med. Chem.* **40** (2002) 107
13. H. I. Mosberg, C. B. Fowler, *J. Peptide Res*. **60** (2002) 329

14. G. M. Morris, D. S. Goodsell, R. S. Halliday, R. Huey, W. E. Hart, R. K. Belew, A. J. Olson, *J. Comput. Chem*. **19** (1998) 1639
15. a) Lj. Došen–Mićović, I. V. Mićović, *J. Serb. Chem. Soc*., **61** (1996) 1117; b) Lj. Došen–Mićović, M. D. Ivanović, G. Roglić, I. V. Mićović, *Electron. J. Theor. Chem. (EJTC)* **1** (1996) 199
16. a) P. S. A. Glass, *J. Clin. Anes.* **7** (1995) 558; b) J. P. Tollenaere, H. Moereels, M. van Loon, *Prog. Drug Res.* **30** (1986) 91
17. Hypercybe, Inc., 419 Phillip St., Waterloo, ON N2L 3X2, Canada
18. a) J. Heerding, K. Raynor, H. Kong, L. Yu, T. Reisine, *Reg. Pept.* **54** (1994) 119; b) K. Befort, L. Tabbara, S. Bausch, C. Chavkin, C. Evans, B. Kieffer, *Mol. Pharmacol.* **49** (1996) 216
19. I. V. Mićović, G. M. Roglić, M. D. Ivanović, Lj. Došen–Mićović, V. D. Kiricojević, J. B. Popović, *J. Serb. Chem. Soc*. **61** (1996) 849
20. A. L. Lomize, I. D. Pogozheva, I. H. Mosberg, *J. Comput. Aided Mol. Des.* **13** (1999) 325
21. M. D. Ivanović, I. V. Mićović, S. Vučković, M. Prostran, Z. Todorović, V. D. Kiricojević, J. B. Djordjević, Lj. Došen–Mićović, *J. Serb. Chem. Soc***. 69** (2004) 511
22. Y. Zhang, Y. Y. Sham, R. Rajamani, J. Gao, P. S. Portoghese, *Chem. Biochem.* **6** (2005) 1.

J. Serb. Chem. Soc. 72 (7) 655–663 (2007) UDC 54.724:547.7+547.831+547.652:534.24
JSCS–3598 *Original scientific paper*

Partitioning of π-electrons in rings of aza-derivatives of naphthalene

IVAN GUTMAN*#, BORIS FURTULA and RADMILA KOVAČEVIĆ

Faculty of Science, University of Kragujevac, P.O.Box 60, 34000 Kragujevac, Serbia

(Received 23 August 2006, revised 9 February 2007)

Abstract: A recently proposed method for calculating the π-electron contents (*EC*) of rings of heteroatom-containing polycyclic conjugated molecules was applied to the aza-derivatives of naphthalene. The main finding was that a nitrogen atom in position α (resp. β) diminishes (resp. increases) the *EC*-value of the respective ring. Such a regularity in the displacement of π-electrons can be (qualitatively) rationalized by means of resonance-theoretical reasoning.

Keywords: π-electron content of ring, heterocyclic conjugated molecules, quinoline, isoquinoline, resonance theory.

INTRODUCTION

In 2004, a method for the partitioning of π-electrons in the rings of polycyclic conjugated hydrocarbons was suggested by means of which the π-electron content of a ring can be assessed by examining the Kekulé structures.[1,2] The method is based on an earlier observation[3,4] that instead of the standard way of drawing a Kekulé structure (by specifying the position of the double bonds,[5,6] it may be represented by indicating the count of π-electrons in each ring.

The construction of so-called "algebraic Kekulé structures" is achieved as follows.[3,4] The number *EC*(R,k) of π-electrons in ring R of the Kekulé structure k is defined as two times the number of double bonds that belong solely to R plus the number of double bonds that are shared by R and another ring; a simple example is found in Fig. 1.

The π-electron content *EC*(R) of a ring R is defined as the arithmetic average of the *EC*(R,k)-values,[1,2] *i. e.*

$$EC(\mathrm{R}) = \frac{1}{K}\sum_{k} EC(\mathrm{R},\mathrm{k}) \qquad (1)$$

* Corresponding author. E-mail: gutman@kg.ac.yu
# Serbian Chemical Society member.
doi: 10.2298/JSC0707655G

where the summation in (1) goes over all K Kekulé structures of the conjugated molecule considered.

It was immediately recognized[7] that the right-hand side of (1) can be expressed in terms of the Pauling bond orders, P_{rs}(Pauling), so that:

$$EC(\mathrm{R}) = 2\sum_{*} P_{rs}(\mathrm{Pauling}) + \sum_{**} P_{rs}(\mathrm{Pauling}) \qquad (2)$$

where $\sum$ indicates summation over those bonds rs which belong solely to ring R, whereas $\sum^{*}$ indicates summation over the bonds rs which are shared by ring R and another $\sum^{**}$ ring.

A large number of studies and applications of the EC-concept were reported. Most of these were concerned with the six-membered rings of benzenoid and coronoid systems.[1,2,7–26] Only in a few papers[27,28] were non-benzenoid hydrocarbons considered and none in which heteroatom-containing conjugated species were studied.

The reason for avoiding the study of the EC-values of heteroatom-containing conjugated molecules is simple: It is not legitimate to apply the model based on Eqs. (1) and (2) to heteroatom-containing conjugated systems. Namely, the employment of these two equations would give results identical to those for the parent hydrocarbon, which is an evident chemical nonsense.

A way out of this difficulty was recently proposed.[29]

Calculating the π-electron contents of rings of heteroatom-containing conjugated molecules

The essence of the method, put forward by one of the present authors,[29] is that instead of Eq. (2), calculation of the π-electron content of a ring R is achieved by means of the expression:

$$EC'(\mathrm{R}) = 2\sum_{*} P_{rs}(\mathrm{HR})' + \sum_{**} P_{rs}(\mathrm{HR})' \qquad (3)$$

where P_{rs}(HR)' is a modified version of the Ham–Ruedenberg bond order[30–32] (for details see below). As in the case of benzenoid hydrocarbons, the Ham–Ruedenberg and the Pauling bond orders coincide,[33,34] the π-electron contents obtained *via* Eqs. (2) and (3) also coincide. On the other hand, the Ham–Ruedenberg bond order can be, without any difficulty, calculated for any heteroatom-containing conjugated system (except those possessing non-bonding molecular orbitals). Therefore, by means of Eq. (3), the π-electron contents can be calculated for rings of any heteroatom-containing conjugated molecule (except in the rare and chemically insignificant cases when the π-electron system considered has non-bonding molecular orbitals).

For the sake of completeness we briefly repeat the definition of the Ham–Ruedenberg bond orders.[30]

Let $C_i = (C_{i1}, C_{i2},\ldots C_{in})$ be a normalized eigenvector of the adjacency matrix $A = \|A_{ij}\|$ of the molecular (Hückel) graph representing the conjugated system under consideration,[35,36] here n stands for the number of vertices of the molecular graph. There exist n linearly independent eigenvectors and, therefore, $i = 1,2,\ldots n$. Let λ_i be the eigenvalue of A, corresponding to the eigenvector C_i, $i = 1, 2,\ldots n$.

Within the Hückel molecular orbital (HMO) theory, C_i and λ_i are in a simple manner related to, respectively, the i-th molecular orbital and the i-th molecular orbital energy level. Let g_i be the occupation number of the i-th MO. Then the Ham–Ruedenberg bond order is defined as:

$$P_{rs}(\mathrm{HR}) = \sum_{i=1}^{n} g_i \frac{C_{ir} C_{is}}{\lambda_i}$$

where it is assumed that no eigenvalue is equal to zero (*i.e.*, that there are no non-bonding MOs). The modified Ham–Ruedenberg bond order, used in Eq. (3), is defined as:

$$P_{rs}(\mathrm{HR})' = P_{rs}(\mathrm{HR}) + \frac{A_{rr}}{\delta_r} P_{rr}(\mathrm{HR}) + \frac{A_{rr}}{\delta_s} P_{ss}(\mathrm{HR})$$

where δ_r and δ_s are, respectively, the degrees (number of first neighbors)[35] of the vertices r and s.

In the case of conjugated hydrocarbons, all diagonal elements of the adjacency matrix A are equal to zero and then there is no difference between the Ham–Ruedenberg bond order P_{rs}(HR) and its modified version P_{rs}(HR)'. If heteroatoms are present, then some diagonal elements of the adjacency matrix are different from zero, implying that $P_{rs}(\mathrm{HR}) \neq P_{rs}(\mathrm{HR})'$.

More details on P_{rs}(HR) and P_{rs}(HR)' can be found in the literature.[29]

TWO SIMPLEST EXAMPLES: QUINOLINE AND ISOQUINOLINE

In order to obtain some experience with the application of formula (3) to the partitioning of π-electrons in polycyclic, heteroatom-containing, conjugated molecules, two monoaza-derivatives of naphthalene, namely quinoline (1-azanaphthalene) and isoquinoline (2-azanaphthalene), were examined.

The numbering of the sites of naphthalene (according to the IUPAC rules) and the labeling of its two rings are shown in Fig. 1.

The *EC*-values of naphthalene are determined by symmetry: since the total number of π-electrons is ten, the π-electron content of each ring must be 5.00. This result is, of course, obtained also by using Eqs. (1) or (2) or (3).

In order to compute the analogous π-electron contents of the aza–derivatives of naphthalene (which can be done only by means of Eq. (3)), an appropriate parametrization for the diagonal elements of the adjacency matrix had to be used. We employed the standard HMO parameters,[37] namely:

$$A_{rr} = \begin{cases} 0.5 & \text{if the atom in position } r \text{ is nitrogen} \\ 0.0 & \text{if the atom in position } r \text{ is carbon} \end{cases} \quad (4)$$

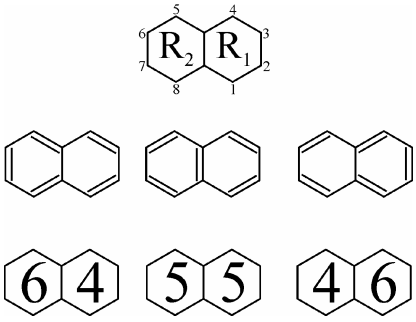

Fig. 1. The numbering of the sites of naphthalene (according to the IUPAC rules) and the labeling of its two rings. In this paper, the sites 1, 4, 5, and 8 are referred to as α and the sites 2, 3, 6, and 7 as β. Also shown are the three Kekulé structures of naphthalene and the corresponding "algebraic Kekulé structures".[3,4] According to the Randić–Balaban method,[1,2] Eq. (1), the π-electron content of each ring is equal to the arithmetic average of the respective numerals inscribed in the "algebraic Kekulé structures". For instance, $EC(R_1) = (4+5+6)/3 = 5.00$.

The results thus obtained are shown in Fig. 2.

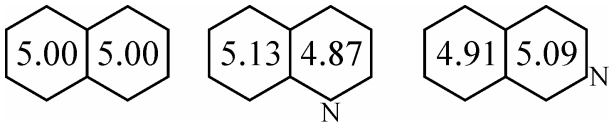

Fig. 2. The partitioning of the ten π-electrons of naphthalene, quinoline, and isoquinoline in their rings. Note that the value 5.00 for the rings of naphthalene is a consequence of molecular symmetry.

As seen from Fig. 2, the nitrogen atom in quinoline (belonging to ring R_1) causes a decrease of the π-electron content of R_1 and therefore an increase of the π-electron content of R_1. The analogous effects in isoquinoline are opposite. As explained below (see the data in Table I), the partitioning of the π-electrons in the rings of quinoline and isoquinoline reflect a more general regularity: a nitrogen atom in position α decreases and in position β increases the π-electron content of the ring to which it belongs.

At this point it is legitimate to ask if the partitioning of π-electrons as shown in Fig. 2 is chemically sound and in agreement with existing chemical theories. In the subsequent section it is demonstrated that the present results agree with the (qualitative) predictions of the resonance theory.[38]

A RESONANCE-THEORETICAL ANALYSIS

Isoquinoline is examined first, because its resonance-theoretical analysis is somewhat simpler.

The nine relevant resonance structures of isoquinoline are depicted in Fig. 3. (Because nitrogen is more electronegative than carbon, only those charge-separated resonance forms in which the negative charge is located at the nitrogen are considered.)

It is plausible to assume[38] that the most significant resonance forms of isoquinoline are those in which there is no (formal) charge separation, namely the

structures **1**, **2** and **3**. If only these were taken into account, then the π-electron contents of the rings R_1 and R_2 would be predicted to be equal to those in naphthalene. Therefore, it is necessary to include into the consideration also the charge-separated species. As already explained, it is assumed that the negative charge is located at the nitrogen atom.

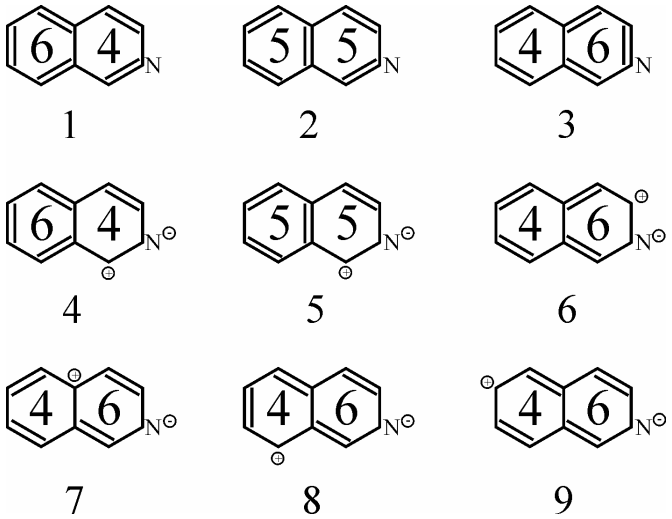

Fig. 3. The significant resonance forms of isoquinoline. The numerals in the rings indicate the count of π-electrons that belong to the particular ring. These are fully analogous to the *EC*(R,*k*)-values described in the text and illustrated in Fig. 1.

Of the six possible resonance structures of this kind, those in which the charge separation is minimal (namely **4**, **5** and **6**) are the most significant. These, however, also imply equal π-electron contents of the rings R_1 and R_2. Therefore attention needs to be focused on the energetically less favorable resonance structures **7**, **8** and **9**, in which the charges are at greater distance. In the latter three resonance structures there are more π-electrons in ring R_1 than in R_2 (*cf.* Fig. 3).

In summary, by taking into account all the nine resonance structures **1**–**9** of isoquinoline, it can be concluded that some displacement of the π-electrons occurs from ring R_2 into the ring R_1. This (qualitatively) agrees with what was found by the calculations.

The case of quinoline is somewhat more perplexing. Its relevant resonance forms are depicted in Fig. 4.

Again, if only the resonance structures **1**, **2** and **3** (with no charge separation) and **4**, **5** and **6** (with charge separation at minimum distance) are considered, no π-electron displacement would be predicted.

The next two (equally) significant resonance forms of quinoline are **7** and **8**. These imply a shift of the π-electrons from ring R_1 to ring R_2. Thus, structures **7**

and **8** (together with **1–6**) imply that the π-electron content of ring R_1 of quinoline is less than that of ring R_2.

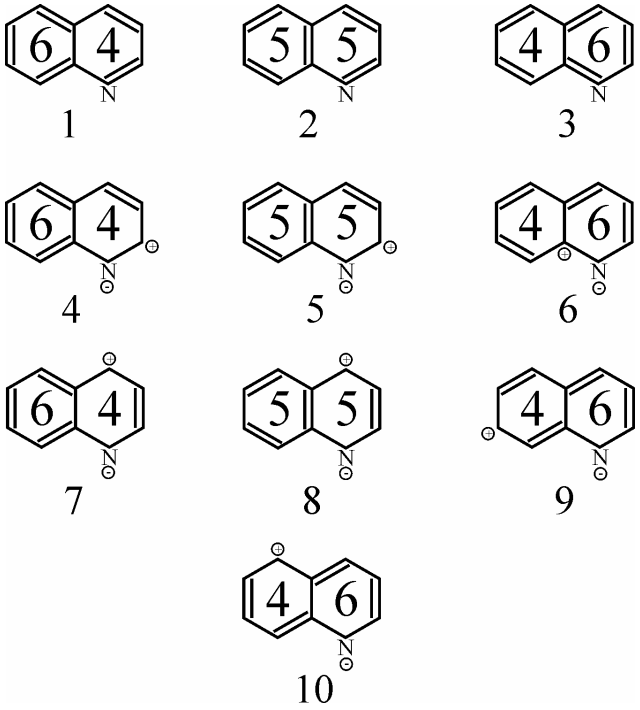

Fig. 4. Same as in Fig. 3, for quinoline.

However, quinoline has two more resonance structures, **9** and **10**, in which ring R_1 has a greater π-electron content than ring R_2. The charge separation in **9** and **10** is greater than in **7** and **8**. Consequently, **9** and **10** are energetically less favorable than **7** and **8** and, therefore, their influence on the partition of the π-electrons should be less pronounced. Thus, if it is accepted that the effect of the resonance structures **9** and **10** can be neglected, relative to the effect of **7** and **8**, then the present findings agree with resonance theory.

NUMERICAL WORK AND DISCUSSION

Using Eq. (3) and the parametrization specified by Eq. (4), the electron contents of the rings of all aza-derivatives of naphthalene were computed. The results for monoaza-, diaza-, triaza- and tetraaza-naphthalenes are given in Table I, whereas the results for (chemically less realistic) pentaaza-, hexaaza- and heptaaza-naphthalenes can be obtained from the authors (R. K.) upon request.

The data in Table I enable several regularities in the partition of the π-electrons in the rings to be envisaged. Of these, the most remarkable are the following:

TABLE I. π-Electron contents, calculated by means of Eq. (3), of the rings R_1 and R_2 of monoaza-, diaza-, triaza-, and tetraaza-derivatives of naphthalene. P. N. A. = position of the nitrogen atom(s), according to the numbering shown in Fig. 1, in which the labeling of the rings (R_1, R_2) is also indicated.

P. N. A.	*EC*'(R_1)	*EC*'(R_2)	P. N. A.	*EC*'(R_1)	*EC*'(R_2)
1	4.8742	5.1258	2	5.0907	4.9093
1,2	5.1823	4.8177	1,3	4.9706	5.0294
1,4	4.9040	4.0960	1,5	5.0000	5.0000
1,6	4.7995	5.2005	1,7	4.7614	5.2386
1,8	5.0000	5.0000	2,3	5.1565	4.8435
2,6	5. 0000	5.0000	2,7	5.0000	5.0000
1,2,3	5.2472	4.7528	1,2,4	5.3243	4.6757
1,2,5	5.3385	4.6615	1,2,6	5.0832	4.9168
1,2,7	5.0970	4.9030	1,2,8	5.3133	4.6867
1,3,5	5.1049	4.8951	1,3,6	4.8954	5.1056
1,3,7	4.8455	5.1545	1,3,8	5.0804	4.9196
1,4,5	5.0300	4.9700	1,4,6	4.7824	5.2176
1,6,7	4.7938	5.2062	2,3,6	5.0370	4.9630
1,2,3,4	5.4945	4.5055	1,2,3,5	5.3205	4.6795
1,2,3,6	5.0877	4.9123	1,2,3,7	5.1430	4.8570
1,2,3,8	5.2993	4.7007	1,2,4,5	5.4494	4.5506
1,2,4,6	5.2118	4.7882	1,2,4,7	5.2448	4.7552
1,2,4,8	5.4826	4.5174	1,2,5,6	5.0000	5.0000
1,2,5,7	5.2573	4.7427	1,2,5,8	5.3638	4.6362
1,2,6,7	5.0796	4.9204	1,2,6,8	5.2183	4.7817
1,2,7,8	5.0000	5.0000	1,3,5,7	5.0000	5.0000
1,3,5,8	5.0839	4.9161	1,3,6,7	4.8940	5.1060
1,3,6,8	5.0000	5.0000	1,4,5,8	5.0000	5.0000
1,4,6,7	4.7927	5.2073	2,3,6,7	5.0000	5.0000

Rule 1. Nitrogen atoms in positions α decrease and in position β increase the π-electron content of the ring to which they belong.

Not a single violation of Rule 1 was found. Quinoline and isoquinoline are the simplest examples illustrating Rule 1. Another convincing example is *EC'*(R_1) = 4.80 and *EC'*(R_1) = 4.76 in 1,6-diaza- and 1,7-diaza-naphthalene, respectively, which should be compared with *EC'*(R_1) = 4.87 in the case of 1-aza-naphthalene. It can be seen that a nitrogen atom in a position in ring R_2 additionally decreases the π-electron content of ring R_1.

Rule 2. Two α nitrogen atoms in the same ring have almost identical effects as a single α nitrogen atom. The same holds for nitrogen atoms in the β position.

Illustrations of Rule 2 are $EC'(R_1) = 4.90$ for 1,4-diazanaphthalene, compared with $EC'(R_1) = 4.87$ for 1-azanaphthalene (two and one α nitrogen atoms), and $EC'(R_1) = 4.78$ for 1,4,6-triazanaphthalene, to be compared with $EC'(R_1) = 4.79$ for 1,4,6,7-tetraazanaphthalene (one and two β nitrogen atoms).

There seems to be no generally valid answer to the obvious question: which effect, α or β is stronger. For instance, the ring R_1 in both 1,2-diaza- and 1,3-diaza-naphthalene possess an α and a β nitrogen atom. Yet, the π-electron contents of R_1 is greater than 5 in 1,2-diaza- and smaller than 5 in 1,3-diaza-naphthalene.

CONCLUDING REMARKS

In this paper, the results of the first study of the partitioning of π-electrons in rings of polycyclic conjugated molecules with heteroatoms are reported. For obvious reasons, the simplest possible such species, aza derivatives of naphthalene, were chosen to be examined. Already for these conjugated system, possessing only two rings, the number of isomers is enormous (*cf.* Table I). Extending such studies to systems with more than two rings promises to be rather difficult. Nevertheless, it is our plan to continue along these lines.

Acknowledgement: This work was supported by the Serbian Ministry of Science and Environmental Protection, through Grant No. 144015G, and Project "Graph Theory and Mathematical Programming with Applications to Chemistry and Engineering".

И З В О Д

ПОДЕЛА π-ЕЛЕКТРОНА У ПРСТЕНОВИМА АЗА-ДЕРИВАТА НАФТАЛЕНА

ИВАН ГУТМАН, БОРИС ФУРТУЛА и РАДМИЛА КОВАЧЕВИЋ

Природно–математички факултет, Универзитет у Крагујевцу, п. пр. 60, 34000 Крагујевац, Србија

Недавно предложена метода за рачунање π-електронског садржаја (*EC*) прстенова у полицикличним коњугованим молекулима који садрже хетероатоме примењена је на аза-деривате нафталена. Најважнија уочена правилност је да азотов атом у положају α умањује *EC*-вредност одговарајућег прстена, док азотов атом у положају β ову вредност повећава. Овакво померање π-електрона може се (квалитативно) објаснити помоћу теорије резонанције.

(Примљено 23. августа 2006, ревидирано 9. фебруара 2007)

REFERENCES

1. M. Randić, A. T. Balaban, *Polyc. Arom. Comp.* **24** (2004) 173
2. A. T. Balaban, M. Randic, *J. Chem. Inf. Comput. Sci.* **44** (2004) 50
3. M. Randić, *J. Chem. Inf. Comput. Sci.* **44** (2004) 365
4. I. Gutman, D. Vukičević, A. Graovac, M. Randić, *J. Chem. Inf. Comput. Sci.* **44** (2004) 296
5. S. J. Cyvin, I. Gutman. *Kekulé Structures in Benzenoid Hydrocarbons*, Springer-Verlag, Berlin, 1988

6. I. Gutman, S. J. Cyvin, *Introduction to the Theory of Benzenoid Hydrocarbons*, Springer-Verlag, Berlin, 1989
7. I. Gutman, T. Morikawa, S. Narita, *Z. Naturforsch*. **59a** (2004) 295
8. A. T. Balaban, M. Randi, *New J. Chem.* **28** (2004) 800
9. I. Gutman, B. Furtula, S. Radenković, *Z. Naturforsch.* **59a** (2004) 699
10. I. Gutman, *Indian J. Chem.* **43A** (2004) 1615
11. I. Gutman, Ž. Tomović, K. Müllen, J. P. Rabe, *Chem. Phys. Lett.* **397** (2004) 412
12. A. T. Balaban, M. Randić, *J. Math. Chem.* **37** (2005) 443
13. I. Gutman, S. Gojak, N. Turković, B. Furtula, *MATCH Commun. Math. Comput. Chem.* **53** (2005) 139
14. I. Gutman, B. Furtula, N. Turković, *Polyc. Arom. Comp.* **25** (2005) 87
15. I. Gutman, M. Randić, A. T. Balaban, B. Furtula, V.Vučković, *Polyc. Arom. Comp.* **25** (2005) 215
16. I. Gutman, G. Stojanović, Ž. Bošković, N. Radulović, P. Rašić, *Polyc. Arom. Comp.* **25** (2005) 345
17. I. Gutman, B. Furtula, S. Jeremić, N. Turković, *J. Serb. Chem. Soc.* **70** (2005) 1199
18. I. Gutman, A. T. Balaban, M. Randić, C. Kiss Tóth, *Z. Naturforsch.* **60a** (2005) 171
19. I. Gutman, N. Turković, *Monatsh. Chem.* **136** (2005) 713
20. B. Furtula, I. Gutman, N. Turković, *Indian J. Chem.* **44A** (2005) 9
21. I. Gutman, S. Milosavljević, B. Furtula, N. Cmiljanović, *Indian J. Chem.* **44A** (2005) 13
22. I. Gutman, A. Vodopivec, S. Radenković, B. Furtula, *Indian J. Chem.* **45A** (2006) 347
23. I. Gutman, N. Turković, B. Furtula, *Indian J. Chem.* **45** (2006) 1601
24. I. Gutman, S. Gojak, N. Radulović, B. Furtula, *Monatsh. Chem.* **137** (2006) 277
25. M. Randić, A. T. Balaban, *J. Chem. Inf. Model.* **46** (2006) 57
26. I. Gutman, B. Furtula, *Z. Naturforsch.* **61** (2006) 281
27. A. T. Balaban, M. Randić, *J. Chem. Inf. Comput. Sci.* **44** (2004) 1701
28. I. Gutman, B. Furtula, *J Mol. Struct. (Theochem)* **770** (2006) 67
29. I. Gutman, *MATCH Commun. Math. Comput. Chem.* **56** (2006) 345
30. N. S. Ham, K. Ruedenberg, *J. Chem. Phys.* **29** (1958) 1215
31. K. Ruedenberg, *J. Chem. Phys.* **29** (1958) 1232
32. K. Ruedenberg, *J. Chem. Phys.* **34** (1961) 1884
33. N. S. Ham, *J. Chem. Phys.* **29** (1958) 1229
34. D. Cvetković, I. Gutman, N. Trinajstić, *J. Chem. Phys.* **61** (1974) 2700
35. I. Gutman, O. E. Polansky, *Mathematical Concepts in Organic Chemistry*, Springer-Verlag, Berlin, 1986
36. J. R. Dias, *Molecular Orbital Calculations Using Chemical Graph Theory*, Springer-Verlag, Berlin, 1993
37. A. Streitwieser, *Molecular Orbital Theory for Organic Chemists*, Wiley, New York, 1961
38. G. W. Wheland, *Resonance in Organic Chemistry*, Wiley, New York, 1955.

J. Serb. Chem. Soc. 72 (7) 665–671 (2007) UDC 547.537:541.6+512.62:539.194
JSCS–3599 *Original scientific paper*

Relating resonance energy with the Zhang–Zhang polynomial

SABINA GOJAK[1], IVAN GUTMAN[2*#], SLAVKO RADENKOVIĆ[2#] and ANDREJ VODOPIVEC[3]

[1]*Faculty of Science, University of Sarajevo, Bosnia and Herzegovina,* [2]*Faculty of Science, University of Kragujevac, P. O. Box 60, 34000 Kragujevac, Serbia,* [3]*Department of Mathematics, IMFM, 1000 Ljubljana, Slovenia*

(Received 23 October 2006, revised 9 February 2007)

Abstract: The Zhang–Zhang polynomial $\zeta(x)$ is a recently conceived tool in the mathematical apparatus of theoretical chemistry. It combines (in a quantitative manner) the Kekulé- and Clar-structure-based features of benzenoid molecules. It is shown that the topological resonance energy (*TRE*) can be accurately approximated as $TRE \approx a\sqrt{\zeta(x)} + b$, where $x \approx 0.5$, by which fact a significant insight is gained into the structure-dependence of *TRE* of benzenoid molecules.

Keywords: benzenoid hydrocarbons, Kekulé structures, Clar structures, Zhang–Zhang polynomial, resonance energy

INTRODUCTION

A few years ago, the Chinese mathematicians Heping Zhang and Fuji Zhang introduced a polynomial that is based on the Kekulé and Clar structures of benzenoid molecules.[1–3] Although these authors reported some chemical applications of their polynomial,[4,5] intensive research along these lines started only relatively recently.[6–9]

In what follows, the polynomial conceived by Zhang and Zhang will be referred to as the *Zhang–Zhang polynomial*, and will be denoted by $\zeta(\mathrm{B},x)$ or $\zeta(x)$, with B symbolizing the underlying benzenoid molecule.

The Zhang–Zhang polynomial is defined in the following manner. Let B be a benzenoid system *i.e.*, a graph representing the carbon-atom skeleton of a benzenoid hydrocarbon; for details see the book.[10] It is assumed that B is Kekuléan, *i.e.*, that it has at least one Kekulé structure. Consider the so-called "*Clar covers*" of B, subgraphs in which all vertices are covered by either isolated edges or by disjoint hexagons. Let $z(\mathrm{B},k)$ be the number of Clar covers of B, containing exactly k hexagons. Then

$$\zeta(\mathrm{B},x) = \zeta(x) = \sum_{k\geq 0} z(\mathrm{B},k)\, x^k \,.$$

* Corresponding author. E-mail: gutman@kg.ac.yu
# Serbian Chemical Society active member.
doi: 10.2298/JSC0707665G

An example illustrating this definition is given in Fig. 1. According to it, the Zhang–Zhang polynomial of pyrene is $6+6x+x^2$. More details on the Zhang–Zhang polynomial can be found elsewhere,[1–9] especially in the chemist-friendly review.[8]

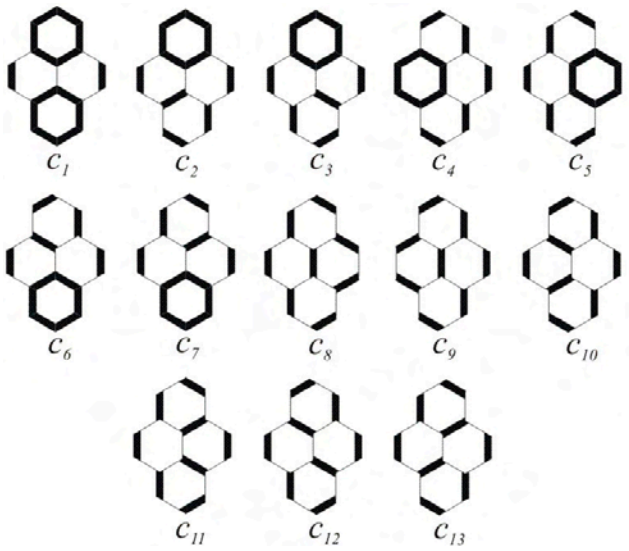

Fig. 1. The Clar covers of pyrene; the chosen edges and hexagons are indicated by heavy lines. One should note that s_1 corresponds to the Clar aromatic sextet formula of pyrene, whereas c_8–c_{13} correspond to its six Kekulé structures. Only the Clar cover c_1 possesses two hexagons; therefore $z(B,2) = 1$. Six Clar covers: c_2, c_3, c_4, c_5, c_6, c_7 possess a single hexagon; therefore $z(B,1) = 6$. Six Clar covers: c_8, c_9, c_{10}, c_{11}, c_{12}, c_{13} do not possess any hexagon; therefore $z(B,0) = 6$. The Zhang–Zhang polynomial of pyrene is thus $z(B,0) + z(B,1)\,x + z(B,2)\,x^2 = 1 + 6x + 6x^2$.

The Zhang–Zhang polynomial unifies the Kekulé- and Clar-theory-based features of the respective benzenoid hydrocarbon. Therefore, its chemical applications should, first of all, be sought in those parts of the theory of benzenoid hydrocarbons in which Kekulé and Clar formulas play a significant role.[10–12] One possible way in which the Zhang–Zhang polynomial can be applied is the following.

An elementary property of the Zhang–Zhang polynomial is that $\zeta(B,0)$ is equal to the number K of Kekulé structures of the benzenoid molecule B. Suppose now that a certain property $\boldsymbol{P}$ of B can be (at least approximately) calculated from the respective K-value:

$$\boldsymbol{P} \approx f(K)$$

which is tantamount to

$$\boldsymbol{P} \approx f(\zeta(0)) \tag{1}$$

Now, if instead of $\zeta(0)$, the Zhang–Zhang polynomial for some other value of x is substituted into formula (1), it may happen that this will result in a better approximation for $\boldsymbol{P}$ than $f(\zeta(0))$.

In this work, the topological resonance energy (*TRE*) and its dependence on the Zhang–Zhang polynomial is examined. Recall,[13,14] that *TRE* is a variant of the Dewar resonance energy[15,16] in which no additional semi-empirical parameters are used for the calculation of the reference energy. More details on *TRE* can be found in the recent reviews[17,18] and in the references cited therein.

DEPENDENCE OF THE TOPOLOGICAL RESONANCE ENERGY ON THE KEKULÉ STRUCTURE COUNT

Although *TRE* has been known for 30 years, and although numerous of its mathematical properties were established, its dependence on the number of Kekulé structures was never properly analyzed. The dominant factor determining the value of *TRE* (as well as of any other kind of resonance energy) is the number of π–electrons[17,18] which, in the case of conjugated hydrocarbons, is determined by the number of carbon-atoms and carbon–carbon bonds. Therefore, in order to examine the influence of other structural factors on *TRE* it is necessary to restrict the consideration to sets of isomers (in which all members have equal number of carbon atoms and equal number of carbon–carbon bonds).[19]

In this work, the results obtained for six sets of benzenoid isomers, those with formulas $C_{22}H_{14}$ (12 isomers), $C_{24}H_{14}$ (13 isomers), $C_{26}H_{14}$ (9 isomers), $C_{26}H_{16}$ (36 isomers), $C_{28}H_{16}$ (62 isomers), and $C_{30}H_{18}$ (118 isomers), are reported. In each of these sets, all possible isomers were taken into consideration.

In earlier works,[5–7] the dependence of *TRE* on *K* (and, consequently, the dependence of *TRE* on $\zeta(x)$) was postulated to be logarithmic. This assertion is a consequence of non-critically accepting that a logarithmic approximation for the original Dewar resonance energy[20] can be applied also to *TRE*. This turned out to be a mistake, since – as seen from Fig. 2 – the dependence of *TRE* on *K* is essentially linear, and by no means logarithmic.

In order to learn about the dependence of *TRE* of benzenoid molecules on their Kekulé structure count, first a typical plot of *TRE vs*. *K* is shown in Fig. 2.

From Fig. 2, it can be seen that there is a good linear correlation between *TRE* and *K*. Such results are found for all the examined sets of benzenoid isomers. However, these correlations can be somewhat improved if, instead of *K*, *TRE* is correlated with K^{λ}. Surprisingly, the values of the exponent λ for which the best correlations are obtained are significantly different from unity. A characteristic example is shown in Fig. 3.

The λ-values that minimize the average relative error of the approximation

$$TRE \approx a\,K^{\lambda} + b \tag{2}$$

are given in Table I. The λ-values for which the correlation coefficients become maximal are close, yet not identical, to those given in Table I. In formula (2) and later in the text *a* and *b* are coefficients calculated by least-squares fitting (differing, of course, for each of the examined six sets). Their values can be obtained from the authors (I.G. & S.R.) upon request.

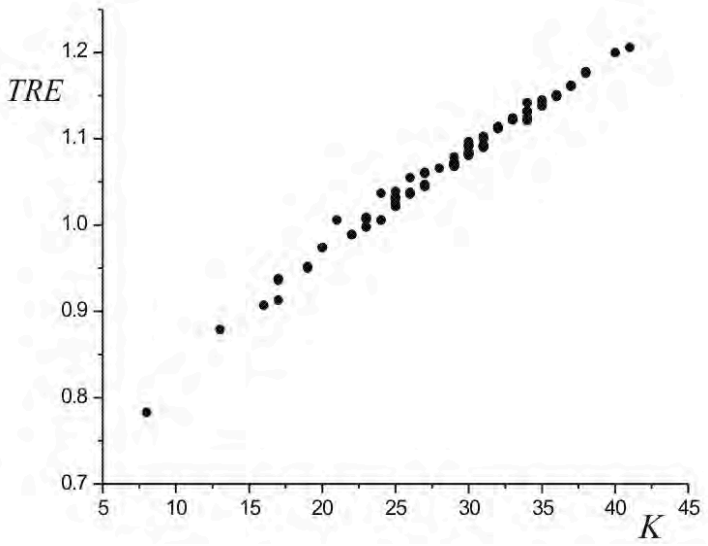

Fig. 2. The topological resonance energies of the heptacyclic catacondensed benzenoid isomers $C_{30}H_{18}$ plotted versus the Kekulé structure count *K*. The correlation appears to be linear. Indeed, the correlation coefficient is 0.993, and the approximation $aK + b$ (with *a* and *b* determined by least-squares fitting) reproduces the *TRE* with an average relative error of 0.55 %. Yet, a slight curvilinearity in these correlations can be observed, and *TRE* is better reproduced by a linear function of K^{λ}, $\lambda \neq 1$, see Fig. 3.

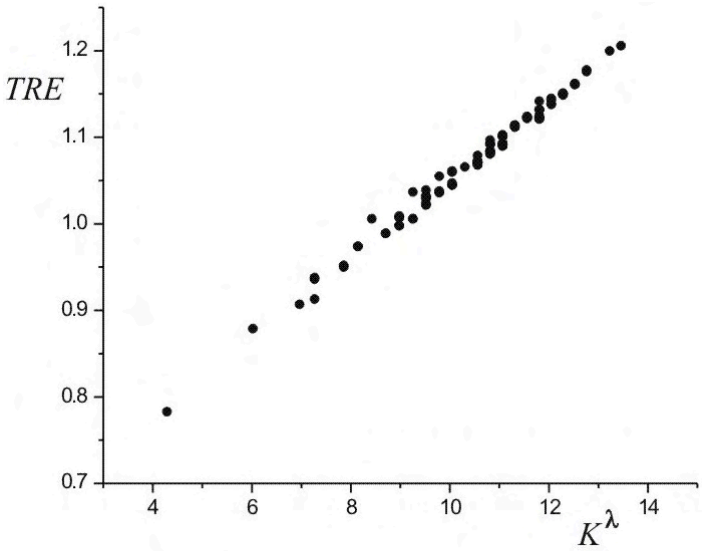

Fig. 3. Same *TRE* values as in Fig. 2 plotted versus K^{λ}, $\lambda = 0.70$. This value of the exponent lambda minimizes the average relative error (= 0.50 %).

TABLE I. Data on the dependence of the topological resonance energy on the Kekulé structure count, of the form given by Eq. (2), for six sets of benzenoid isomers. *N.I.* = the number of Kekuléan isomers of the benzenoid systems with the given formula; all these isomers were contained in the sets considered; *AERR*(λ) = average relative error for the given (optimal) value of the parameter λ; *AERR*(λ = 1) = average relative error of formula (2) for λ = 1, *i. e.*, for the linear dependence of *TRE* on *K*

Formula	*N.I.*	λ	*AERR*(λ) / %	*AERR*(λ = 1) / %
$C_{22}H_{14}$	12	0.89	0.37	0.39
$C_{24}H_{14}$	13	1.53	0.55	0.71
$C_{26}H_{14}$	9	0.75	0.44	0.46
$C_{26}H_{16}$	36	0.77	0.46	0.50
$C_{28}H_{16}$	62	1.24	0.71	0.75
$C_{30}H_{18}$	118	0.70	0.50	0.55

DEPENDENCE OF TOPOLOGICAL RESONANCE ENERGY ON THE ZHANG–ZHANG POLYNOMIAL

The findings outlined in the previous section suggest that in the case of topological resonance energy, the approximation of type (1) should be chosen to have the form

$$TRE \approx a\,\zeta(x)^{\lambda} + b \tag{3}$$

where the parameters λ and x should be used for optimization. The optimal values of these parameters (determined so as to minimize the average relative error) are given in Table II.

TABLE II. Data on the dependence of the topological resonance energy on the Zhang–Zhang polynomial, of the form given by Eq. (3), for the same benzenoid isomers as in Table I. *AERR*(λ,x) = = average relative error for the given (optimal) values of the parameters λ and x; *ERR*(max) = = maximal relative error observed

Formula	λ	x	*AERR*(λ,x) / %	*ERR*(max) / %
$C_{22}H_{14}$	0.65	0.31	0.33	0.56
$C_{24}H_{14}$	0.33	0.69	0.41	1.16
$C_{26}H_{14}$	0.34	0.86	0.31	0.78
$C_{26}H_{16}$	0.51	0.30	0.39	1.15
$C_{28}H_{16}$	0.64	0.54	0.71	0.75
$C_{30}H_{18}$	0.45	0.36	0.50	0.55

Both the optimal λ- and optimal x-values given in Table II vary to a great extent from sample to sample. Nevertheless, it appears as if both the λ- and the x-va-

lues "oscillate" around the value 0.5. Indeed, the approximation (3) will not lose much of its precision if one sets $\lambda = 0.5$ and also $x = 0.5$. If so, then one arrives at the expression

$$TRE \approx a\sqrt{\zeta(1/2)} + b \qquad (4)$$

Statistical data pertaining to formula (4) are given in Table III. As seen by comparing the columns *AERR* and *AERR*(min), the accuracies of formula (4) and of the optimized formula (3) are practically the same. One should, nevertheless, bear in mind that the exponent $\lambda = 0.5$, leading to the expression (4) was chosen only because of simplicity. Other values for this exponent could serve as well, but then the form of the resulting approximation would be somewhat more complicated.

TABLE III. Data on the dependence of the topological resonance energy on the Zhang–Zhang polynomial, of the form given by Eq. (4), for the same benzenoid isomers as in Table I. *AERR* = average relative error for $\lambda = x = 0.5$; *ERR*(max) = maximal relative error observed; *AERR*(min) = the (minimal) *AERR*-value, attained for the optimal choices of λ and x (same as *AERR*(λ,x) in Table II).

Formula	*AERR* / %	*ERR*(max) / %	*AERR*(min) / %
$C_{22}H_{14}$	0.35	0.67	0.33
$C_{24}H_{14}$	0.43	1.17	0.41
$C_{26}H_{14}$	0.33	0.66	0.31
$C_{26}H_{16}$	0.42	1.10	0.39
$C_{28}H_{16}$	0.56	2.56	0.52
$C_{30}H_{18}$	0.46	2.73	0.41

CONCLUSIONS

By means of formula (4), the *TRE*–values may be reproduced with an error that is (on average) around 0.5 % or below, and (in the worst case) less than 2–3 %. This aspect of Eq. (4) may be viewed as something not particularly valuable. In our opinion, *the true value of the formula (4) is* not so much in its ability to estimate *TRE*, but *in the insight that it gives* into the structure–dependence of *TRE* and, consequently,[13–19] *into the structure-dependence of the stability and "aromaticity" of benzenoid molecules*. In particular, formula (4) provides a *quantitative* connection between Clar-theory-based structural features and resonance energy. Recall that in the original Clar aromatic sextet theory,[11] all considerations were non-quantitative, and that until now very few quantitative Clar-theory-based approaches have been put forward.[21]

The fact that in formulas (3) and (4) the parameter x is significantly different from zero indicates that not only the Kekulé structures (*via* z(B,0)), but also the cyclic Clar covers (*via* z(B,1), z(B,2), ...) influence the value of the topological resonance energy. As $x \approx 1/2$, it can be seen that the (stabilizing) effect of a Clar

cover with a single hexagon is about 50 % of the effect of a Kekulé structure, the effect of a Clar cover with two hexagons is about 25 % of the effect of a Kekulé structure, etc.

ИЗВОД

ВЕЗА ЕНЕРГИЈЕ РЕЗОНАНЦИЈЕ СА ЖАНГ–ЖАНГОВИМ ПОЛИНОМОМ

SABINA GOJAK[1], ИВАН ГУТМАН[2], СЛАВКО РАДЕНКОВИЋ[2] и ANDREJ VODOPIVEC[3]

[1]*Faculty of Science, University of Sarajevo, Bosnia and Herzegovina,* [2]*Природно–математички факултет Универзитета у Крагујевцу, Крагујевац и* [3]*Department of Mathematics, IMFM, 1000 Ljubljana, Slovenia*

Жанг–Жангов полином $\zeta(x)$ је један недавно предложени објекат који се примењује у математичком формализму теоријске хемије. Он повезује (на квантитативан начин) особине засноване на Кекулеовим и Кларовим структурама бензеноидних молекула. Показано је да се тополошка енергија резонанције (*TRE*) може веома тачно апроксимирати формулом $TRE \approx a\sqrt{\zeta(x)} + b$, где је $x \approx 0{,}5$.

(Примљено 23. октобра 2006, ревидирано 9. фебруара 2007)

REFERENCES

1. H. Zhang, F. Zhang, *Discrete Appl. Math.* **69** (1997) 147
2. H. Zhang, *Discrete Math.* **172** (1997) 163
3. H. Zhang, F. Zhang, *Discrete Math.* **212** (2000) 261
4. H. Zhang, *MATCH Commun. Math. Comput. Chem.* **29** (1993) 189
5. F. Zhang, H. Zhang, Y. Liu, *Chin. J. Chem.* **14** (1996) 321
6. I. Gutman, S. Gojak, B. Furtula, *Chem. Phys. Lett.* **413** (2005) 396
7. I. Gutman, S. Gojak, S. Stanković, B. Furtula, *J. Mol. Struct. (Theochem)* **757** (2005) 119
8. I. Gutman, A. T. Balaban, B. Furtula, *Polyc. Arom. Comp*. **26** (2006) 17
9. I. Gutman, S. Gojak, B. Furtula, S. Radenković, A. Vodopivec, *Monatsh. Chem.*, **137** (2006) 1127
10. I. Gutman, S. J. Cyvin, *Introduction to the Theory of Benzenoid Hydrocarbons*, Springer-Verlag, Berlin, 1989
11. E. Clar, *The Aromatic Sextet*, Wiley, London, 1972
12. M. Randić, *Chem. Rev*. **103** (2003) 3449
13. J. Aihara, *J. Am. Chem. Soc*. **98** (1976) 2750
14. I. Gutman, M. Milun, N. Trinajstić, *J. Am. Chem. Soc*. **99** (1977) 1692
15. M. J. S. Dewar, C. de Llano, *J. Am. Chem. Soc*. **91** (1969) 789
16. N. C. Baird, *J. Chem. Educ*. **48** (1971) 509
17. L. J. Schaad, B. A. Hess, *Chem. Rev*. **101** (2001) 1465
18. M. K. Cyranski, *Chem. Rev*. **105** (2005) 3773
19. I. Gutman, S. Radenković, N. Trinajstić, A. Vodopivec, *Z. Naturforsch.* **61a** (2006) 345
20. R. Swinborne–Sheldrake, W. C. Herndon, I. Gutman, *Tetrahedron Lett*. (1975) 755
21. W. C. Herndon, H. Hosoya, *Tetrahedron* **40** (1984) 3987.

J. Serb. Chem. Soc. 72 (7) 673–678 (2007) UDC 546.36*137+582.293.378+66.061+54–145.15
JSCS–3600 *Original scientific paper*

Extraction of ^{137}Cs from *Cetraria islandica* lichen using acid solutions

ANA ČUČULOVIĆ[1]*#, DRAGAN VESELINOVIĆ[2#] and ŠĆEPAN S. MILJANIĆ[2]

[1]*INEP-Institute for the Application of Nuclear Energy, Banatska 31b, 11080 Zemun and*
[2]*University of Belgrade, Faculty of Physical Chemistry,11001 Belgrade, P.O. Box 137, Serbia*

(Received 17 April 2006, revised 1 December 2006)

Abstract: The extraction of ^{137}Cs sorbed in samples of *C. islandica* using acid solutions was investigated. An equation describing the reduction of the ^{137}Cs content in a dry lichen sample with the number of volumes of acid solutions used for successive extractions was used. The possibility of the existence of two different types of sorption of ^{137}Cs in the lichen was confirmed. Acid rains were shown to influence the extraction of ^{137}Cs.

Keywords: ^{137}Cs sorption, extraction of ^{137}Cs from lichen, *C. islandica* lichen, acid solutions.

INTRODUCTION

Lichen react with ozone, SO_2 and ammonia which are present in air as the pollutants.[1–5] Acid rains, which contain H_2SO_4 and HNO_3, formed from SO_2 and NO_2 in air, can result in the extinction of lichen. The problems of the influence of acid rain on lichens have been reported in the literature.[6–9] In a previous study,[10] the desorption of ^{137}Cs from the lichen *Cetraria islandica* was investigated using distilled water (pH = 6.48). It was found that after five successive extractions, 49.0 % and 59.6 % of the ^{137}Cs had been extracted after equilibration time of 7 and 24 h, respectively. These results indicate lichens as secondary sources of environment pollution with ^{137}Cs.

Since there are no data in the accessible literature on the extraction of ^{137}Cs, or other metals, from lichens by acid rains, the extraction of ^{137}Cs from dried lichen using a solution having the properties of acid rain was investigated in this study.

EXPERIMENTAL

In the present experiments, the apparatus, vessels, sample, extraction procedure and the measurement of the ^{137}Cs activity in the samples were the same as reported previously.[10] The employed sulfuric acid, nitric acid and ammonium sulfate were of *p.a.* grade and were obtained from Merck, Alkaloid and Euro Hemija, respectively.

* Corresponding author. E-mail: anas@inep.co.yu
# Serbian Chemical Society member.
doi: 10.2298/JSC0707673C

Extraction procedure

Four types of solutions were used: A–H_2SO_4; B–HNO_3; C–H_2SO_4–HNO_3 and D–H_2SO_4––HNO_3–$(NH_4)_2SO_4$. Solutions A and B were made of 200 cm^3 of distilled water into which the required concentrated acid was added until the desired pH value were attained: 2.00; 2.87 and 3.75 (solutions A_1, A_2, A_3 and B_1, B_2, B_3). Solutions C was obtained by mixing 100 cm^3 of solution A and 100 cm^3 of solution B, with the same pH values (solutions C_1, C_2 and C_3). Solution D was obtained by adding 1 g of ammonium sulfate to 100 cm^3 of solution C and adjusting the pH value with concentrated sulfuric acid. After measuring the activity, 200 cm^3 of the required solution was poured over 10 g of dried lichen. The extractions were performed at room temperature (~22 °C) and lasted 24 h with occasional mixing. The lichen material was recovered by filtration and its activity remeasured. All extractions were repeated twice and the mean values are given in the Tables I–IV.

RESULTS AND DISCUSSION

The ^{137}Cs content in every sample is expressed as the percentage of the cesium remaining in the sample after every extraction and in relation to its content in the initial sample. The results of the measurements are given in Tables I–IV, as mean values with a standard measurement error of 2.1 (Table I) and 2.5 % (Tables II and III).

TABLE I. Activity* of ^{137}Cs (Bq/kg) in *C. islandica* lichen before extraction and the percentage of remaining ^{137}Cs after each of five consecutive extractions with solutions at pH 2.00. Room temperature (~22 °C). Mean measurement error 2.5 %.

Starting activity of ^{137}Cs in lichen before extraction *A* / Bq kg^{-1}	2603	2310	2295	3166
Extraction solution**	A	B	C	D
Extraction	Percentage of remaining ^{137}Cs in lichen after each extraction in relation to the starting content (100 %)			
I	61.1	60.3	51.8	46.5
II	49.6	49.9	41.7	34.9
III	45.0	45.8	39.4	34.1
IV	42.6	44.4	39.2	34.0
V	42.1	41.9	36.5	33.6
Total extracted ^{137}Cs from lichen / %	57.9	58.1	63.5	66.4

*mean values, **solution compositions are given in the Experimental

From Tables I–III, it can be seen that changes in the pH value of the solution influence the extraction of radiocesium from lichen, *i.e.*, the significant role of H^+ ion in the exchange of $^{137}Cs^+$ ion. The first extraction was the most significant for the extraction of ^{137}Cs, indicating the presence of the two types of extraction mechanism. Also, regardless of the pH value of the solution, the extractions with solution D were the most efficient, indicating the significant role of NH_4^+ ion in the exchange of Cs^+ ion. In comparison with results obtained with distilled water, it can be seen that the extraction with water was also high (pH = 6.48; total extracted 59.6 %),[10] and that the presence of other cations chan-

ged the total effect of the desorption of Cs^+. No influence of anions was registered, most probably because the Cs^+ ion, as an alkali metal ion, practically does not form complex compounds.

TABLE II. Activity* of ^{137}Cs (Bq kg^{-1}) in *C. islandica* lichen before extraction and the percentage of the remaining ^{137}Cs after each extraction of five consecutive extractions at pH 2.87. Room temperature (~22 °C). Mean measurement error 2.1 %

Starting activity of ^{137}Cs in lichen before extraction *A* / Bq kg^{-1}	2534	2870	2689	2804
Extraction solution**	A	B	C	D
Extraction	Percentage of remaining ^{137}Cs in lichen before each extraction in relation to the starting content (100 %)			
I	60.7	65.0	70.9	39.9
II	56.4	57.6	60.1	32.6
III	54.4	51.5	58.7	32.4
IV	50.7	47.4	58.3	31.7
V	49.7	46.9	55.0	30.6
Total extracted ^{137}Cs from lichen / %	50.3	53.1	45.0	69.4

*mean values, **solution compositions are given in the Experimental

TABLE III. Activity* of ^{137}Cs (Bq/kg) *C. islandica* lichen before extraction and the percentage of the remaining ^{137}Cs after each extraction of five consecutive extractions at pH 3.75. Room temperature (~22 °C). Mean measurement error 2.1 %

Starting activity of ^{137}Cs in lichen before extraction *A* / Bq kg^{-1}	2595	2129	2500	2878
Extraction solution**	A	B	C	D
Extraction	Percentage of remaining ^{137}Cs in lichen before each extraction in relation to the starting content (100 %)			
I	76.6	65.3	70.0	44.5
II	65.9	59.0	62.1	41.7
III	62.2	51.3	61.6	41.2
IV	61.6	50.0	58.6	39.3
V	60.7	46.3	54.6	38.3
Total extracted ^{137}Cs from lichen / %	39.3	53.7	45.4	61.7

*mean values, **solution compositions are given in the Experimental

Using the Origin 7.0 software package, the obtained curves show an exponential dependence of the remaining amount of ^{137}Cs, *i.e.*, extracted amount from the number of successive extractions, regardless of pH value, as presented in Fig. 1 for selected examples. This can be explained by the fact that in the solid state–solution system, the amount of sorbed substance is determined by a distribution coefficient, regardless of whether the sorption–desorption mechanism is based on physical or chemical sorption or ionic exchange. According to this, the extraction process of ^{137}Cs is a process of desorption.

TABLE IV. Values of the starting activity of ^{137}Cs ($C_0^{'}$), determined by extrapolation of the curves in Fig. 3, given as a percentage in relation to the experimentally determined values of C_0 (100 %)*

Extraction solution**	pH	$C_0^{'}$ /%	ΔC_0=100– $C_0^{'}$
A	2.87	68.03	31.97
B	2.87	46.53	53.47
C	3.75	63.12	36.88

*mean values, **solution compositions are given in the Experimental

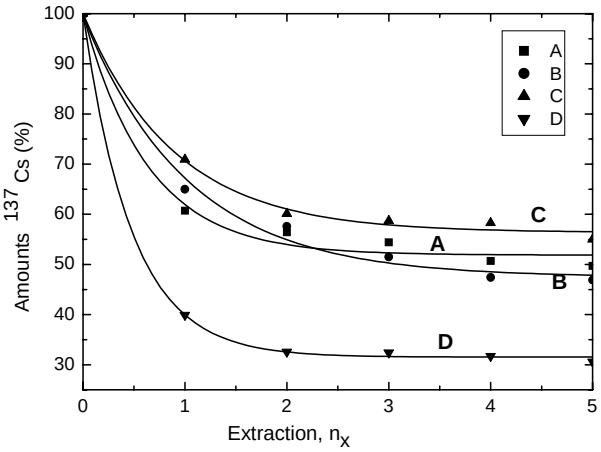

Fig. 1. ^{137}Cs content in lichen (%) in relation to the starting content in dependence on the number of successive extractions, n_x. The lichen was treated with solutions at pH 2.87 for 24 h.

If a series of consecutive extractions of the substance sorbed in the solid phase is performed, the amount of sorbed substance is reduced. For successive extractions with an equal volume of extractant, the change of the sorbed substance with the number of extractions is presented by the following equation:

$$\ln C_x = \ln C_0 - a n_x \quad (1)$$

where C_0 is the concentration of the sorbed substance before extraction.[10]

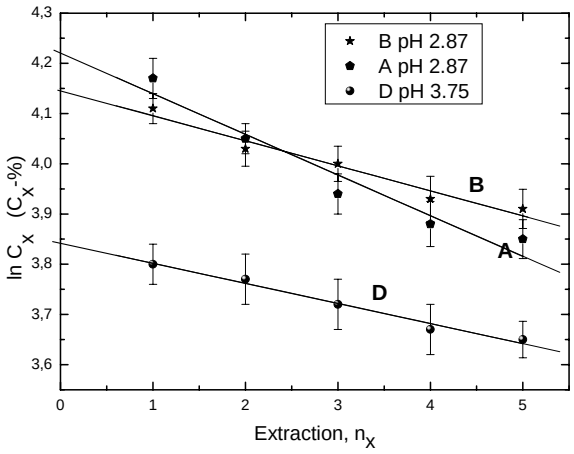

Fig. 2. ^{137}Cs content (%) in the sorbent (*C. islandica*) as a function of the number of successive extractions with solutions at pH 2.87 (A and B) and pH 3.75 (D), (n_x), according to Eq. (1), for an equilibration time of 24 h.

From Eq. (1), it follows that the dependence of the logarithm of the amount of sorbed substance in the solid state is a linear function of the number of successive volumes employed during extraction. For real systems, this is valid when only one type of sorption exists, or if one type is dominant, so that the others can be disregarded (this was the case for extraction with distilled water lasting 1 hour[10]). In other cases, deviations from a straight line occur, indicating that the sorbent can bind the sorbed substance by different types of sorption, *i.e.* different sorbent points.

Using Eq. (1), two types of curves were obtained with the results given in Tables I–III. A linear dependence was obtained when solutions A and B at pH = 2.87 and solution D at pH = 3.75 were used. Extrapolation of the curves (Fig. 2) gave values marked as C_0 given in Table IV. They are smaller than the corresponding initial values given in Tables II and III, indicating that one type of sorption is dominant in these cases, but at least one more type of sorption is present. In the remaining cases, curves were obtained, selected examples of which are given in Fig. 3, demonstrating the presence of at least two types of sorption, but the extraction of cesium when using the corresponding extractant was not differentiated enough to make one of them dominant.

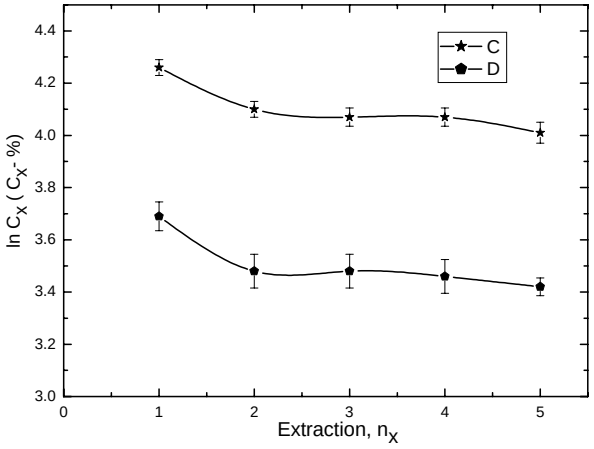

Fig. 3. ^{137}Cs content (%) in the sorbent (*C. islandica*) as a function of the number of successive extractions with solutions B and C, pH 2.87 (n_x), according to Eq. (1), for an equilibration time of 24 h.

Additionally, the obtained results also indicate that ^{137}Cs extraction, to a certain degree, depends on the acidity of rain, *i.e.* its pollution. The obtained changes of the amount of extracted ^{137}Cs range from 0.2 %, when solutions A and B, the most acidic ones (pH = 2.00), were used to 24.4 % when some of the solutions C and D with pH = 2.87 were employed, as can be seen from the data given in Tables I–III. Also, for all pH values covered by the present experiments, the highest percentage of extracted ^{137}Cs was obtained when solution D was used, indicating the role of NH_4^+ ions in the extraction process.

The results obtained show that lichen, *i.e.* its remnants, become sources of secondary pollution with ^{137}Cs, also due to the possibility of accumulation of other elements.

Acknowledgement: The Serbian Ministry of Science and Environmental Protection financed this work, Project No. ON142039.

И З В О Д

ЕКСТРАКЦИЈА ^{137}Cs ИЗ ЛИШАЈА *Cetraria islandica* КИСЕЛИМ РАСТВОРИМА

АНА ЧУЧУЛОВИЋ[1], ДРАГАН ВЕСЕЛИНОВИЋ[2] и ШЋЕПАН С. МИЉАНИЋ[2]

[1]ИНЕП–Институт за примену нуклеарне енергије, Банатска 31б, 11080 Земун и [2]Универзитет у Београду, Факултет за физичку хемију, п.пр. 137, 11000 Београд

Испитивана је екстракција ^{137}Cs сорбованог у узорцима лишаја *C. islandica* киселим растворима. Коришћена је једначина која даје смањење садржаја ^{137}Cs у сувом узорку лишаја са бројем коришћених запремина киселих раствора, при сукцесивним екстракцијама. Показана је могућност постојања различитих типова сорпције ^{137}Cs у лишају, као и утицај киселих киша на екстракцију ^{137}Cs.

(Примљено 17. априла 2006, ревидирано 1. децембра 2006)

REFERENCES

1. J. E. Sloof, *Environmental lichenology: biomonitoring trace-element air pollution*, Ph.D. Thesis, Delft University of Technology, Delft, The Netherlands, 1993
2. V. Ahmadjian, M. E. Hale, *The lichens*, Academic Press, New York, 1973
3. M. Nifontova, *Sci. Total. Environ.* **161** (1995) 747
4. E. Gorham, *Can. J. Botany* **37 (**1959) 327
5. K. J. Puckett, *New Phytol.* **72** (1973) 329
6. R. Piervittori, L. Usai, F. Alessio, M. Maffei, *Lichenologist* **29** (1997) 191
7. T. C. Hutchinson, M. Dixon, M. Scott, *Water Air Soil Pollut.* **31**(1986) 409
8. J. Garty, Z. Karary, J. Harel, *Environ. Exp. Bot.* **32** (1992) 229
9. L. Sigal, J. W. Johnston, *Environ. Exp. Bot.* **26** (1986) 59
10. A. Čučulović, D. Veselinović, Š. S. Miljanić, *J. Serb. Chem. Soc.* **71** (2006) 565.

J. Serb. Chem. Soc. 72 (7) 679–686 (2007) UDC 546.831+546.226:66.095.21.097:66.022.362
JSCS–3601 *Original scientific paper*

Content of sulfates and their stability – key factors determining the catalytic activity of sulfated zirconia catalysts

ALEKSANDRA ZARUBICA[1], PAULA PUTANOV[2] and GORAN BOŠKOVIĆ[1]*#

[1]*Faculty of Technology, University of Novi Sad, Cara Lazara 1, 21000 Novi Sad and* [2]*Serbian Academy of Sciences and Arts, Knez Mihajlova 35, 11000 Belgrade, Serbia*

(Received 27 October 2006)

Abstract: Two series of sulfated zirconia catalysts were synthesized from various precursors using mono- or multi-step sequence preparations under laboratory conditions. Their activities/selectivities in the isomerization reaction of *n*-hexane were correlated to their textural, structural and morphological properties. The slightly higher activity of a commercially sulfated $Zr(OH)_4$-based catalyst is in agreement with the differences in the content of SO_4^{2-} ions and their thermal stability, textural and structural properties, *i.e.*, crystallite size and possible imperfection of the incorporation of sulfate groups in the multi-step synthesis of the catalyst having a nitrate origin. The employment of H_2 as the carrier gas resulted in no catalytic activity, regardless of the catalyst precursor, preparation method and calcination temperature. When the isomerization reaction was performed under He, the relatively short life-times of all catalyst samples were caused by fast deactivation due to coking in the absence of H_2.

Keywords: sulfated zirconia, sulfate contents, isomerization of *n*-hexane, activity, textural, structural and morphological properties

INTRODUCTION

The selective transformation of straight-chain hydrocarbons to high octane number isomers is of great industrial importance, particularly for gasoline blending. Solid acids have become very popular as catalysts for the isomerization of alkanes. Among them, sulfated zirconia (SZ), alone as well as together with promoters, represents a promising solution in view of both activity and stability. Namely, its activity is better than those of zeolite-based catalysts and its poison and water resistance makes the position of SZ somewhere between the previous and traditional chlorinated Pt–alumina catalysts.[1]

Zirconia modified with sulfate ions may behave as a solid acid depending on its preparation method, differing in the synthesis and activation parameters.

* Corresponding author. E-mail: boskovic@uns.ns.ac.yu
# Serbian Chemical Society member.
doi: 10.2298/JSC0707679Z

These are temperature, pH, duration of precursors aging, nature of sulfating agents, *etc*.[1,2] In addition, the order and number of steps in the preparation sequence can affect the final textural and structural features of the catalyst.[3]

The catalytic activities of SZ are found to be different depending on both the pre-calcination and calcination temperature, indicating the importance of an optimal activation temperature for the increase in acidity.[4,5] The correlation of the calcination temperature with activity indicated the importance of the tetragonal phase of SZ and its acidic behavior.[6]

In the present study, two series of SZ catalysts were prepared from different precursors by related preparation methods following calcination. The aim of the work was to link the different amount of sulfates with stability in terms of phase transformation, as well as to compare the catalytic performances of a catalyst fully synthesized under laboratory conditions, including sulfation with another one obtained from a sulfated commercial precursor. Both precursors were calcined at three different temperatures and their characterization was performed in respect to textural and structural properties. These were correlated to catalytic activity tested in the isomerization of *n*-hexane reaction.

EXPERIMENTAL

Two SZ catalysts were prepared from different precursors: 1) from a commercially sulfated zirconium(IV)-hydroxide (Aldrich Co.) by its calcination (catalyst 1), and 2) from zirconium(IV)--oxynitrate (Aldrich Co.) by the precipitation/impregnation method following calcination (catalyst 2). For the preparation of the latter, a watery solution of Zr(IV)-oxynitrate (15 mass %) was permanently stirred at room temperature for 2 h, keeping the pH 9.5 by the addition of 25 % NH_4OH as the precipitating agent. The obtained Zr(IV)-hydroxide was aged for 2 h, filtrated, rinsed with distilled water several times and finely dried at 110 ºC for 24 h. The subsequent sulfation of the hydroxide was realized by impregnation of the dried solid with the desired volume of sulfuric acid (0.5 M H_2SO_4) for the intended sulfur content of 3 mass % S. Finely, both precursors samples were dried at 110 ºC for 3 h and then calcined at either 500, 600 or 700 ºC for 3 h in an air flow of 20 ml min^{-1}. In total, six SZ catalyst samples were obtained, denoted as 1 and 2 depending on the precursor type, followed by A, B or C indicating the applied calcination temperature, 500, 600 or 700 ºC, respectively. The accomplishment of the sulfation of the samples, *i.e.*, the amount of SO_4^{2-}, was checked by the TG method employing a Baehr STA 503 instrument in the temperature range 30 – 1000 ºC using a temperature ramp of 10 ºC min^{-1}.

Surface area and porosity measurements were carried out on a Micromeritics ASAP 2010 apparatus following low temperature N_2 adsorption/desorption and using the BET procedure. Before each measurement, the sample was outgassed at 200 °C for 1 h in order to desorb impurities on its surface. The crystal structure was determined by X-ray diffraction analysis (XRD) using a Philips APD-1700 diffractometer, at 40 kV and 55 mA. Powders of samples were packed in a 20×20 mm polymer frame and exposed to radiation in the 2θ angle range from 20 – 70º. The average crystallite sizes were estimated from the full width at half-maximum employing the Scherrer equation. The surface morphology of catalysts samples previously coated with gold was investigated by scanning electron microscopy (SEM) using a Jeol JSM-6460LV instrument with an acceleration voltage of 25 kV.

The activity testing was carried out on the *n*-hexane isomerization reaction at atmospheric pressure and 300 ºC, using a space velocity $6 \cdot 10^{-2}$ mmol *n*-C_6 g^{-1} min^{-1}. The molar ratio of carrier

gas (He or H_2) and *n*-C_6 was 15.5 at a constant partial pressure of *n*-C_6 of 60.5 mbar. The activation of 0.5 g of fresh sample was performed *in situ*, in a synthetic air flow of 20 ml min^{-1} at 500 ºC for 1 h. The reactor effluent was analyzed by gas chromatography, a HP 5890 equipped with a Pona column and a FID detector. The catalyst activity was calculated as the conversion of *n*-hexane and the selectivity as the sum of the isomerized hydrocarbons. Finally, the yields of the isomers were calculated as the product of conversion and selectivity to C_6-isomers.

RESULTS AND DISCUSSION

The part of X-ray diffractograms of catalysts 1 and 2 including the most characteristic peaks of SZ phases are shown in Fig. 1. The corresponding phase composition and crystallite size, calculated from the XRD-line broadening, are presented in Table I, together with the textural properties of the samples. The prevailing zirconia phase in the samples was estimated from the intensities of the XRD lines of the tetragonal and two monoclinic phases by a procedure given previously.[7] The related catalytic activity performances are given in Table II.

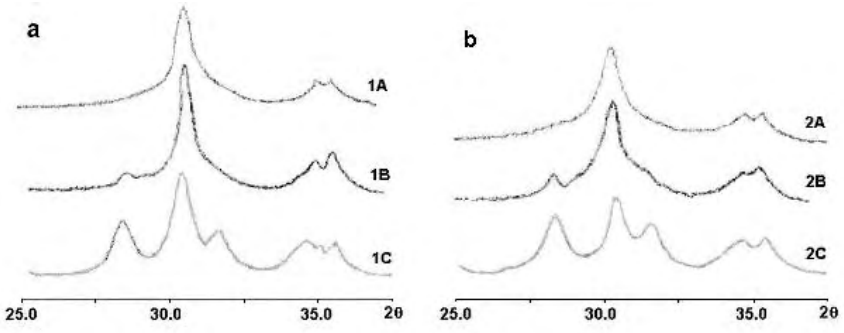

Fig. 1. XRD Pattern of catalysts 1 (a) and 2 (b) after calcination at 500 °C (A), 600 °C (B) and 700 °C (C).

TABLE I. Textural properties, phase composition and crystallite size

Sample	Surface area $m^2\ g^{-1}$	Mean pore diameter nm	SO_4^{2-} mass loss %	Crystallite size* / nm	
				Tetragonal phase	Monoclinic phase
1A	130	2.3	5.0	10.3 (+)	–
1B	103	3.3	3.8	11.8 (+)	11.7
1C	69	5.7	2.1	12.7 (+)**	13.7 (+)**
2A	144	3.2	2.6	8.2 (+)	–
2B	117	4.4	2.6	12.7 (+)	9.1
2C	89	6.0	2.6	13.7	10.2 (+)

*Prevailing phase is denoted with "+" in parentheses, **Equal fractions of both phases

The XRD patterns of samples of series A (samples 1A and 2A in Figs. 1a and 1b) show the presence of only tetragonal SZ phases at $2\theta = 30.30^{o}$, despite the precursor type and the preparation method of the catalysts. On increasing the

calcination temperature to 600 ºC (series B), a new peak appearing at $2\theta = 28.25^{o}$ may be assigned to the monoclinic SZ phase, however its contribution is still minor. A further increase of the calcination temperature to 700 ºC (series C) resulted in an abundance of monoclinic phases (peaks at $2\theta = 28.25^{o}$ and $2\theta = 31.25^{o}$), which finally prevailed, but only in the case of catalyst 2 tailored in the laboratory (sample 2C in Fig. 1b, and Table I).

TABLE II. Catalytic performances of the SZ samples calcined at various temperatures in the isomerization of *n*-hexane at 300 ºC

Sample	*X* %	Selectivity to *i*-C_6 / %	Yield to *i*-C_6 / %	Hydrocarbons composition of the products / %			
				Σ *i*-C_4, *i*-C_5	Σ Cracked C–H	Mono-branched isomers	Di-branched isomers
1A	50.4	12.0	6.0	46.8	41.2	9.5	2.5
1B	22.1	13.5	3.0	39.5	46.7	11.2	2.3
1C	0	–	–	–	–	–	–
2A	40.0	10.3	4.1	41.9	47.7	8.4	1.9
2B	10.5	21.5	2.3	35.2	42.6	18.5	3.0
2C	8.5	39.2	3.3	30.2	29.7	22.7	16.5

An increase of the height/width ratio of the peaks corresponding to both SZ phases in the XRD patterns accompanied the phase transformation, confirming the increase the crystallite size as an indication of the sintering process (Table I). Although the prevailing phase and crystallites sizes of both series of catalysts samples were similar, catalyst 1 was more stable regarding the transformation of the favorable tetragonal phase and retained its smaller crystallites sizes when exposed to higher calcinations temperatures. The activity of the catalysts samples (Table II) are in accordance with a conclusion of the importance of the tetragonal SZ phase in the isomerization reaction of *n*-hexane.[8] The importance of the presence of sulfate groups attached to tetragonal zirconia for the formation of an active SZ catalyst was reported previously.[9] As can be seen from Table I, higher amount of sulfates in the samples of catalyst 1 seems to have been beneficial for retarding the transformation from the tetragonal to the monoclinic phase.

The obtained values of the BET surface areas (Table I) are higher than those obtained by other authors.[5,10] As expected, the BET surface areas declined and the mean pore diameters increased for both catalyst series with increasing calcination temperature. The high BET surface area of sample 2A is in accordance with it having the smallest crystallite size, which obviously influenced its activity/selectivity performances (Table II).

The XRD (Fig. 1) and SEM (Fig. 2) results indicate to the nano-structure of both investigated catalysts. The SEM studies, however, support the assumption based on the dependence of the particle size on the precursor type, preparation procedure and sulfates content. Namely, the SEM microphotographs reveal the

presence of nano-sized particles in both samples originating from the commercial precursor (catalyst 1) after calcination at the higher temperatures, since the majority of the particles were smaller than 100 nm (Figs. 2a and 2b). In contrast, the particles of the catalyst 2 samples, having the same temperature history as catalyst 1, are of different morphology and definitely of larger size (Figs. 2c and 2d). The difference in the particle size and their morphology may be attributed to the different procedures of preparation, *i.e.*, only the calcination step for the preparation of catalyst 1 *versus* a number of steps in the sequence of the synthesis of catalyst 2. The specific change of the morphology observed for both catalysts samples exposed to the highest temperature treatment, reflected in the agglomeration of individual particles to aggregates of larger sizes, confirms the sintering process (series C) (Figs. 2b and 2d).

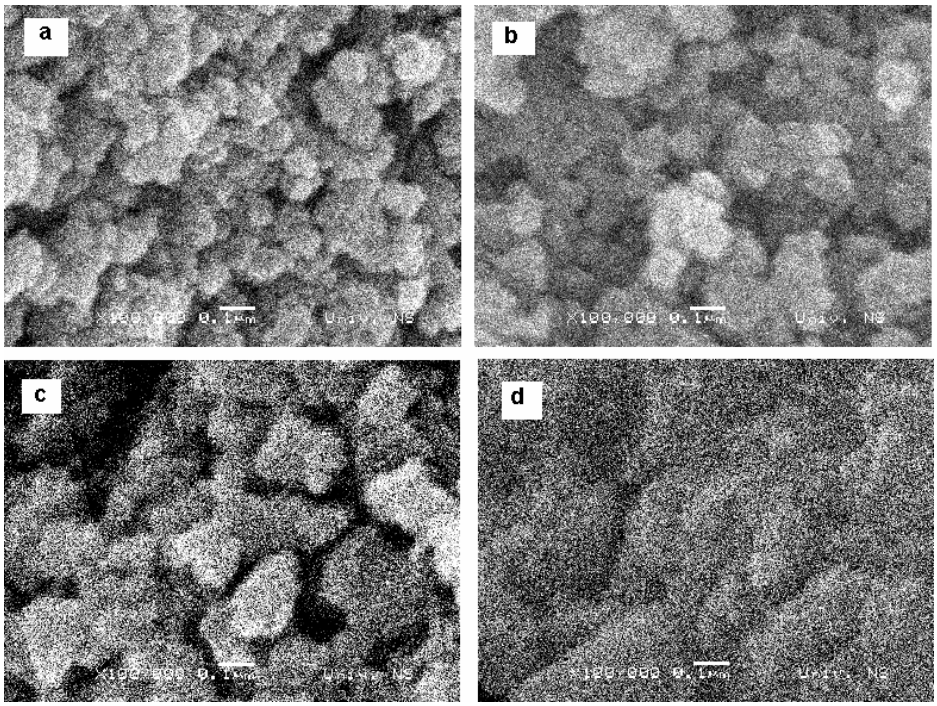

Fig. 2. SEM Images of catalyst 1 calcined at 600 ºC (a) and 700 ºC (b), and catalyst 2 calcined at 600 ºC (c) and 700 ºC (d) (×100,000).

The discussed structural and textural properties of the catalysts have an impact on the corresponding activity and selectivity results of the samples. In experiments performed in He as carrier gas, the catalysts were quite active at the very beginning of the time-on-stream (TOS), but a fast deactivation followed. The reaction tests were performed for as long as activities were recorded (Fig. 3.), *i.e.*, the TOS changed from 30 – 115 min depending on the applied cata-

lyst. The catalyst samples from series A calcined at the lowest temperature exhibited the highest conversions and the longest TOS. The relatively short life-time of all the catalyst samples caused by the fast deactivation can be attributed to the process of coking in the absence of H_2. This was even visually evident by the black color of the samples at the end of the TOS and was proved by the successful regeneration of the deactivated catalysts in an air flow at 500 °C for 2 h. Using H_2 as the carrier gas in the same test-reaction-set-up resulted in no catalytic activity, regardless of the catalyst precursor, amount of sulfates, preparation method and calcination temperature. In contrast, some initial activity of SZ under H_2 was claimed previously but with poor isomerization selectivity.[11]

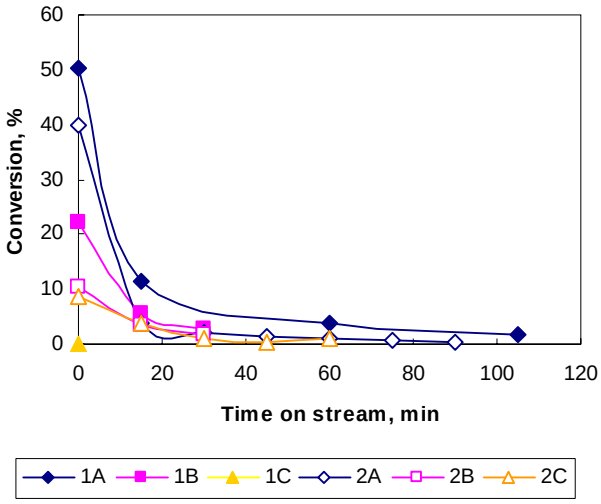

Fig. 3. *n*-Hexane conversion as a function of time-on-stream using He as the carrier gas.

The obtained results of *n*-hexane conversion (Table II) indicate catalysts of similar activities, with significantly higher yield attributed to series A compared to samples exposed to the higher calcination temperatures (series B and C). This is in particular the case with catalyst 1, which showed no activity after calcination at 700 °C. This may be connected to sample 1C having the lowest surface area of all the catalyst samples.

The selectivity profiles for all the samples were, as expected, inversely proportional to their conversions. Cracked hydrocarbons dominated in the composition of the product hydrocarbons, coupled with rather low values of the highly desirable di- and mono-branched C_6-isomers (Table II). Catalyst 2C, however, had a better selectivity in terms of both cracking and C_6–isomers. At the first glance, this could be related to the formation of stronger acidic sites at the higher calcination temperatures, as a general acidity feature reported for some other catalysts,[12,13] avoiding a simultaneous dramatic decrease of the surface area (Table I). In the inert atmosphere employed here, however, a mechanism including

acid sites may be quite questionable. It is more likely that during *n*-hexane isomerization, an oxidative dehydrogenation reaction occurs leading to the reduction of S^{6+} to S^{4+}, water and oxidized hydrocarbon species.[14] The differences in the content and thermal stability of SO_4^{2-} reflected in the difference in the dynamic of their removal (Table I) are in accordance with the higher activity of catalyst 1 samples. The trend of decreasing activity of the samples of catalyst 2, however, having a constant amount of sulfates regardless of the calcination temperature, is due to a weakening of the textural and structural properties with increasing temperature. The inverse activities of samples 1C and 2C indicate the importance of the necessity of a minimum amount of sulfates and advantageous textural properties, which are both absent in the case of the sample 1C.

A general feature of all the investigated samples, revealed as a minor fraction of highly desirable dimethyl butanes in the products, could be understood in terms of the insufficient acidity of the catalysts and the absence of H_2 and metal functions, both necessary for the bifunctional mechanism.[15] The direct isomerization of *n*-hexane is possible through a carbenium ion, which requires a very strong acid site, or a carbonium ion, which demands a high reaction temperature.[16] It is likely that sites of required acidity and/or mandatory reaction conditions were missing in the catalytic runs of the present investigations.

CONCLUSIONS

Two sulfated zirconia catalysts with different amounts of sulfates, prepared by appropriate methods and from different precursors, showed similar activities when calcined at the lower temperature. Both the amount and quality of the sulfate groups incorporated into the zirconia matrix influenced the stability of the catalysts in terms of tetragonal to monoclinic phase transformation. In addition, the manner of catalyst preparation, reflected as the order and number of steps in the preparation sequence, affected the final textural and structural features of the catalyst. As a result, a somewhat lower conversion was obtained in the case of the catalyst completely tailored under laboratory conditions *vs.* a commercially sulfated precursor based catalyst. Both the existence of a minimum amount of sulfates and advantageous textural properties are prerequisites for satisfactory catalyst activity.

In an inert atmosphere and at a relatively low reaction temperature, the isomerization reaction *n*-hexane occurred although by the mechanism of oxidative dehydrogenation rather than by the mechanism including acid sites.

Acknowledgement: The financial support of the Serbian Ministry of Science and Environmental Protection (Project No. 142024: "To Green Chemistry *via* Catalysis") and the Serbian Academy of Sciences and Arts is highly appreciated.

И З В О Д

САДРЖАЈ СУЛФАТА И ЊИХОВА СТАБИЛНОСТ – ОДРЕЂУЈУЋИ ФАКТОРИ АКТИВНОСТИ КАТАЛИЗАТОРА НА БАЗИ СУЛФОНОВАНЕ ЦИРКОНИЈЕ

АЛЕКСАНДРА ЗАРУБИЦА[1], ПАУЛА ПУТАНОВ[2] и ГОРАН БОШКОВИЋ[1]

[1]Технолошки факултет, Универзитет у Новом Саду, Цара Лазара 1, 21000 Нови Сад и [2]Српска академија наука и уметности, Кнез Михајлова 35, 11000 Београд

Две серије катализатора на бази сулфоноване цирконије су синтетисане из различитих прекурсора одговарајућим једно- или више-степеним секвенцама припреме у лабораторијским условима. Њихове активности/селективности у реакцији изомеризације *n*-хексана су корелисане са текстуралним, структуралним и морфолошким особинама. Виша активност катализатора на бази комерцијално сулфонованог $Zr(OH)_4$ је у сагласности са вишим садржајем SO_4^{2-}, њиховом различитом термичком стабилношћу, текстуралним и структуралним својствима. Начин уградње сулфатних група у вишестепеној синтези катализатора нитратног порекла додатно одређује величину кристалита, са негативним утицајем на активност. Коришћење водоника као носећег гаса не даје активан катализатор без обзира на прекурсор, методу синтезе и температуру калцинације. Изомеризација изведена у присуству хелијума резултира релативно кратким животом свих узорака катализатора услед акумулације кокса у реакционим условима који онемогућавају ауторегенерацију.

(Примљено 27. октобра 2006)

REFERENCES

1. G. D. Yadav, J. J. Nair, *Micropor. Mesopor. Mater.* **33** (1999) 1
2. A. Corma, J. M. Serra, A. Chica, *Catal. Today* **81** (2003) 495
3. D. Tichit, B. Coq, H. Armendariz, F. Figueras, *Catal. Lett.* **38** (1996) 109
4. V. Bolis, G. Magnacca, G. Cerrato, C. Morterra, *Topics Catal.* **19** (2002) 259
5. K. Fottinger, G. Kinger, H. Vinek, *Appl. Catal. A: General* **226** (2004) 195
6. T. Yamaguchi, *Appl. Catal. A: General* **61** (1990) 1
7. H. Toraya, M. Yoshimura, S. Somiya, *J. Am. Ceram. Soc.* **67** (1984) C–119
8. M. Signoretto, F. Pinna, G. Strukul, *Catal. Lett.* **36** (1996) 129
9. G. Resofszki, M. Muhler, S. Sprenger, U. Wild, Z. Paal, *Appl. Catal. A: General* **240** (2003) 71
10. M. Benaissa, J. G. Santiesteban, G. Diaz, C. D. Chang, M. Jose–Yacaman, *J. Catal.* **161** (1996) 694
11. S. R. Vaudagna, R. A. Comelli, N. S. Figoli, *Catal. Lett.* **47** (1997) 259
12. G. Boskovic, R. Micic, P. Pavlovic, P. Putanov, *Catal. Today* **65** (2001) 123
13. G. Boskovic, T. Vulic, E. Kis, P. Putanov, *Chem. Eng. Technol.* **3** (2001) 269
14. T. Buchholz, U. Wild, M. Muhler, G. Resofszki, Z. Paal, *Appl. Catal. A: General* **189** (1999) 225
15. H. Liu, H. Lei, W. M. H. Sachtler, *Appl. Catal. A: General* **37** (1996) 167
16. P. A. Jacobs, J. A. Martens, *Stud. Surf. Sci. Catal.* **58** (1991) 445.

J. Serb. Chem. Soc. 72 (7) 687–698 (2007) UDC 669.141.24+678.774:541.183:620.193
JSCS–3602 *Original scientific paper*

Corrosion inhibition of iron in hydrochloric acid by polyacrylamide

DRAGICA CHAMOVSKA, MAJA CVETKOVSKA and TOMA GRCHEV*

Faculty of Technology and Metallurgy, St. Cyril and Methodius University, 1000 Skopje, FYRO Macedonia

(Received 3 August 2006, revised 15 February 2007)

Abstract: The corrosion protection and/or adsorption of polyacrylamide (PAA) of number average molecular weight, $\overline{M}_n$, between 15,000 – 1,350,000 g mol^{-1} on mild steel and iron (99.99 % Fe) in 3 M HCl at room temperature was studied using spectrophotometry (the phenanthroline method), the weight loss method and EIS (Electrochemical Impedance Spectroscopy). It was found that the corrosion protection efficiency of the PAA – adsorbed layers strongly depends on both the molar concentration of PAA in the solution and its molecular weight, reaching limiting values between 85 and 96 %. Simultaneously, it was also concluded that a relatively high surface coverage could be obtained with very low PAA concentrations (0.5 – 2 ppm), indicating the good adsorption characteristics of PAA on mild steel and iron in hydrochloride acid. The experimentally obtained results follow a Langmuir adsorption isotherm. According to the best fitting parameters, the adsorption coefficient B ranged between 2×10^7 and 4×10^8 mol^{-1} and depended strongly on the molecular weight of the PAA: $B = k\,\overline{M}_n^{\alpha}$ (for $\alpha \approx 0.67$ and $k = 2.95\times10^4$) or the size of the polymer coil. As was found by EIS, the thickness of the adsorbed PAA layer was approx. 1.1 nm (for $\varepsilon_r = 15$) and corresponded only to the polymer segments attached to the metal surface. On the other hand, as was found by ellipsometry, the limiting layer of the adsorbed PAA molecules was highly voluminous and relatively thick (100 – 200 nm), containing entangled polymer coils.

Keywords: mild steel, corrosion inhibition, polyacrylamide, electrochemical impedance spectroscopy, adsorption isotherm.

INTRODUCTION

The adsorption of macromolecules at the solid/solution interface differs in many respects from that of small molecules.[1] For example:

i) segments may be "adsorbed" although they are not in direct contact with the surface, *i.e.*, as loops or tails rather than trains;
ii) the nature of the adsorption isotherm differs, *i.e.*, polymer adsorption leads in general to high affinity isotherms;
iii) the polydispersity of polymers affects the adsorption;

* Corresponding author. E-mail: toma@tmf.ukim.edu.mk
doi: 10.2298/JSC0707687C

iv) the adsorption rates are much slower, particularly in the case of higher polydispersity.

It has been observed that a very small amount of certain water soluble polymers, which are effective as flocculating agents, are extremely effective in inhibitting corrosion of ferrous materials in contact with water. Thus, it was found that such polymers in an amount ranging from 5×10^{-6} to 2 wt. % remove the products of corrosion formed prior to treatment and effectively prevent further corrosion.[2]

Therefore, it was of interest to explain the specifity of adsorption of macromolecules and to study their conformational behavior in solution, especially at the metal/solution interface.[3,4] It was shown that using a statistical–mechanical treatment it is possible to estimate the number of conformations during the adsorption of polymer molecules.[5–7]

Previous work on this subject was focused on the conformational behavior of polyacrylamide (PAA) adsorbed on silver and titanium.[6] As shown by ellipsometry, the chemisorption of PAA on a bare silver surface is more pronounced compared with that on a Ti/TiO_2 interface. The presence of PAA in boric–borate buffer, pH 8.4, mostly inhibits the processes in the active region of passivetion of iron.[8] These results show that PAA adsorbs mainly on the bare active metal surface.

Double-layer capacitance measurements of the metal/solution interface can give valuable additional information about the adsorption of polymers. An attempt to correlate the adsorption and/or inhibition characteristics of polyacrylamide with various molecular weights on iron from acidic solutions of HCl (a very important industrial process for the removal of scales from steel surfaces) with its conformational behavior in solution[9] was made in this study.

EXPERIMENTAL

The corrosion protection efficiency of PAA was followed on mild steel coupons (70 mm×15 mm×2 mm) (0.1 % C, 0.012 % S, 0.015 % P, 0.01 % Si, 0.4 % Mn and 0.07 % Cu) in 3 M HCl at room temperature using the weight loss method and the spectroscopic phenanthroline method at 508 nm for the determination of the Fe(II)-ion concentration in the solution. The duration of the corrosion tests was 5 hours.

The impedance measurements for iron in 3 M HCl at the corrosion potential ($E = -250 \pm 10$ mV/SHE) were carried out in the frequency range from 100 kHz to 10 mHz (with an a.c. signal of 5 mV). An iron rod (99.99 % Fe; 0.18 cm^2) mounted in a Teflon holder and platinum foil (10 cm^2) were used as the working electrode and auxiliary electrode, respectively. The potentials were measured *versus* saturated calomel electrode and are referred to the standard hydrogen electrode (SHE). The aqueous solutions of 3 M HCl were prepared from 36 wt % HCl (*p.a.*, Merck) and redistilled water ($\kappa < 2\times10^{-7}$ S cm^{-1}). PAA was obtained by the redox-initiated polymerization of acrylamide. Six fractions of PAA with molecular weights from 15,000 to 1,350,000 g mol^{-1} were used in this study. The polydispersity index of the employed PAA samples ranged from 1.2 to 1.35.

The experimental results were fitted using the Boukamp program.[10]

RESULTS

Spectrophotometric and gravimetric measurements

As it was stated in the Experimental, the rate of corrosion of mild steel in 3 M HCl was following by spectrophotometry and weight loss measurements. PAA with molecular weights from 15,000 to 1,350,000 g mol^{-1} and concentrations from 0.2 to 100 ppm in the solution were used as the corrosion inhibitors. Using the obtained experimental results, the protection efficiency coefficient, η_{prot}, was calculated by means of Eqs. 1 and 2. It should be noted that the assumption $\eta_{\text{prot.}} = \theta$ (where θ is the relative surface coverage with adsorbed PAA molecules or segments), usually used for the adsorption of organic molecules at a metal/solution interface,[11] was made in the present case as well:

$$\eta_{\text{prot.}} = \theta = (\Delta m - \Delta m^{\text{c}}) / \Delta m \qquad (1)$$

where Δm and Δm^{c} represent the weight loss of the steel coupons (mg cm^{-2}) in the absence or in the presence of PAA (with the concentration c_{PAA} in mol dm^{-3}), respectively.

Using the spectrophotometric results for the concentration of Fe(II)-ions in the solution, the corrosion protection efficiency of PAA, or surface coverage (θ) of the steel surface with adsorbed PAA-molecules (or segments) was calculated by means the equation:

$$\eta_{\text{prot.}} = \theta = (c^{0}_{\text{Fe(II)}} - c^{\text{c}}_{\text{Fe(II)}}) / c^{0}_{\text{Fe(II)}} \qquad (2)$$

where $c^{0}_{\text{Fe(II)}}$ and $c^{\text{c}}_{\text{Fe(II)}}$ represent the concentration of Fe(II)-ions in the solution after the corrosion test (μg cm^{-3}) in the absence and in the presence of PAA of concentration c (mol dm^{-3}), respectively.

It should be mentioned that both methods showed fairly good agreement as far as the protection efficiency of PAA is concerned. The experimentally obtained results are presented in Fig. 1, from which it can be seen that the surface coverage of the steel surface (θ) or the corrosion protection efficiency of PAA adsorbed layer depends both on the concentration of PAA in the solution and its molecular weight, reaching limiting values between 0.85 and 0.96. Simultaneously, it can be concluded that a relatively high value of θ can be obtained using very low PAA concentrations (0.5 – 2 ppm), indicating the very good adsorption characteristics of PAA onto mild steel in aqueous solutions of HCl. As it was shown in previous papers,[6,12,13] PAA and/or poly(acrylic acid) are better anodic inhibitors than cathodic ones. The adsorbed polymer layers which inhibit the corrosion process are relatively thick, 100 – 250 nm, and highly voluminous, containing a small amount of solid material (approx. 1 wt. %).

The presented results in Fig. 1 are in good accordance with a Langmuir adsorption isotherm:

$$\theta / (1-\theta) = Bc \quad (3)$$

where B is the adsorption coefficient (mol^{-1}) and c is the concentration of PAA ($mol\ dm^{-3}$) in the solution.

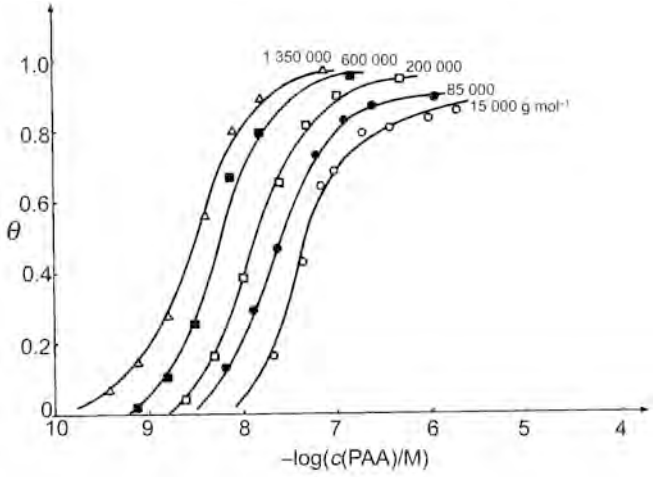

Fig. 1. Adsorption isotherms for PAA from 3 M HCl on mild steel at 293 K.

The best fitting parameters of the obtained experimental results are presented in Table I.

TABLE I. Best fitting parameters for the adsorption of PAA on mild steel from 3 M HCl at 293 K; using a Langmuir adsorption isotherm

$\overline{M}_n$ / g mol^{-1}	B / mol^{-1}	$-\Delta G^{\ominus}$ / kJ mol^{-1}	r
15,000	2.0×10^{7}	50.74	0.978
85,000	6.25×10^{7}	53.51	0.987
200,000	9.8×10^{7}	54.61	0.995
600,000	2.4×10^{8}	56.80	0.992
1, 350,000	4.1×10^{8}	58.09	0.997

The values of $\Delta G^{\ominus}$ were calculated using the equation:[12]

$$-\Delta G^{\ominus} = RT \ln (55.5B) \qquad (\text{J mol}^{-1}) \quad (4)$$

where 55.5 is the concentration of water ($mol\ dm^{-3}$) in the solution.

It can be concluded that the adsorption coefficient B and $\Delta G^{\ominus}$ depend on the molecular weight of the PAA and follow the empirical Equation:[14]

$$B = k\ \overline{M}_n^{\alpha} \quad (\text{for } \alpha \approx 0.67 \text{ and } k = 2.95\times10^{4}) \quad (5)$$

The same type of empirical Equations describe the relationship between the molecular weight of a polymer and its dilute solution viscosity (η),[15] between the adsorbed quantity of the polymer (m)[16] and the radius of gyration of the polymer coil in the solution (R_G).[9]

Electrochemical Impedance Spectroscopy (EIS) study

The adsorption and/or corrosion protection efficiency of PAA on iron from 3 M HCl at room temperature was examined using Electrochemical Impedance Spectroscopy (EIS) at the corrosion potential in the frequency range from 100 mHz to 100 kHz with a.c. signal of 5 mV. These experiments were performed for several molecular weights of PAA (from 15,000 to 1,500,000 g mol^{-1}), usually in the concentration range of PAA from 0.5 to 200 ppm.

Analyzing the obtained Bode plots ($\log Z - \log f$ and $\varphi - \log f$) for PAA adsorption on iron presented in Fig. 2, the following can be concluded:

i) The $\log Z - \log f$ and $\varphi - \log f$ dependences indicate the existence of three main regions. In the first one, at high frequencies (from 25 – 100 kHz), the measured impedance (Z) of approx. 2 Ω or 0.34 Ω cm^{-2}, as well as the phase angle (up to 5 degree) are very low, corresponding to an ohmic resistance of the electrolytic solution (3 M HCl) between the working and the reference electrode.

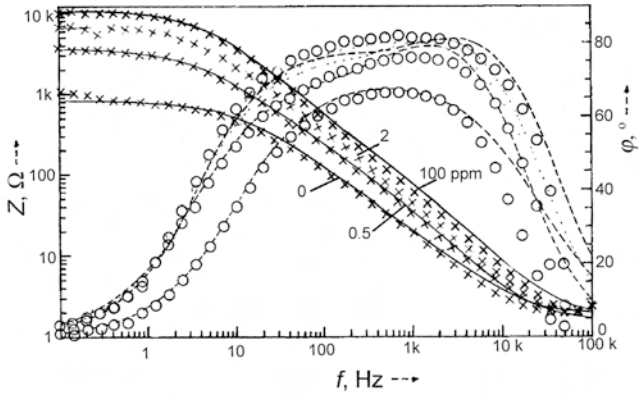

Fig. 2. Bode plots for the adsorption of PAA ($\overline{M}_n$ = 15,000 g mol^{-1}) on iron (A = 0.18 cm^2) from 3 M HCl at room temperature and the corrosion potential.

ii) The second region (from ≈ 8 kHz to 20 Hz) shows a linear $\log Z - \log f$ dependence with a slope, $\partial(\log Z)/\partial(\log f)$, ranging from 0.84 to 0.944 and phase angles between 65 and 82 (non-ideal condenser), depending on the concentration of PAA in the solution and corresponding to the capacitance of the iron/solution interface (in the absence or in the presence of PAA in the solution).

iii) At low frequencies (from 5 Hz to 100 mHz) the measured impedances Z are practically again not influenced by the frequency accompanied with an abrupt decrease of the phase angle ($\varphi \to 0$). Thus, the measured impedances in this region corresponds to the sum of charge transfer and electrolytic resistance ($Z = R_{ct} + R_{el}$).

Evidently, regions 1 and 3 show typical ohmic behavior with $Z_1 = R_{el}$ and $Z_3 = R_{ct} + R_{el}$, respectively. As far as the second region is concerned (linear $\log Z - \log f$ dependences), the impedance for a non-ideal condenser can be represented as:

$$Z = 1/Q\,(j\,\omega)^n \tag{6}$$

and for an ideal condenser (n = 1) as:

$$Z = 1/C_{dl}\,(j\,\omega) \tag{7}$$

where C_{dl} is a capacitance of the electrochemical double layer.

The Fe/3 M HCl-interface is presented in Fig. 3, without (case a) and with PAA in the solution (case b), respectively. The simple equivalent electric circuit (R(QR)) can be used in two cases:

i) For impedance characterization of the Fe/3 M HCl-interface, by determination of R_{ct} (or $j_{corr} = (RT/zF)(1/R_{ct})$) and the values of Q and n(CPE) in the absence of PAA in the solution.

ii) For impedance characterization of the Fe/adsorbed polymer layer/3 M HCl ($\theta \geq 0.7$) with PAA in the solution, which form a compact and stable inhibition layer on the metal surface, Figs. 4 and 5.

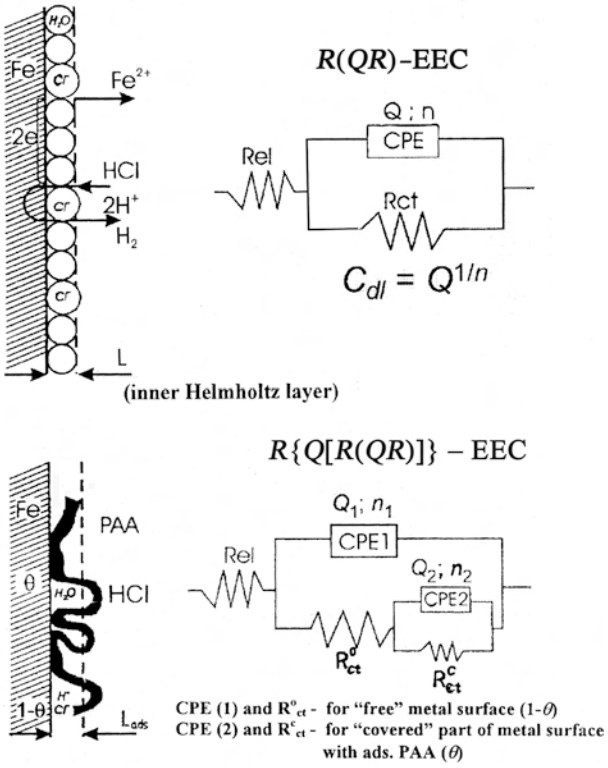

Fig. 3. Schematic representation of the Fe/HCl interface in the absence (a) and in the presence (b) of PAA in the solution.

On the other hand, the more complex $EEC - R\{Q[R(QR)]\}$ takes into account a parallel existence of covered parts of iron surface ($0.1 < \theta < 0.7$) with adsorbed PAA molecules or segments and uncovered parts of the metallic surface ($1-\theta$) which are in direct contact with the electrolyte. In this case, the experi-

mentally obtained impedance results should indicate the existence of two *RC* constants (Q_1R_{ct1} and Q_2R_{ct2}) or two relaxation times ($\tau_1 = 1/C_1R_{ct1}$ and $\tau_2 = 1/C_2R_{ct2}$), Figs. 6 and 7.

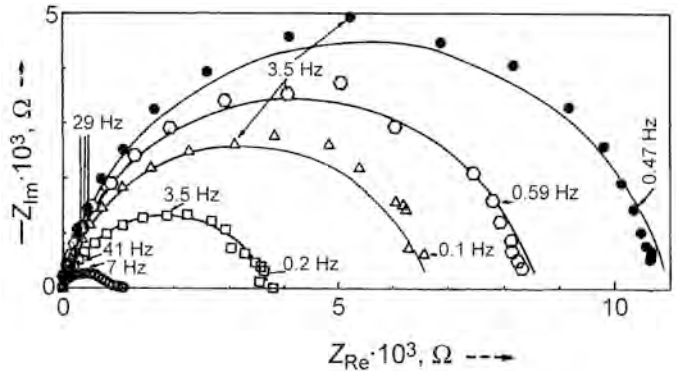

Fig. 4. Experimental (O; □; △; ○;●) and theoretical (—) Nyquist plots for 0, 0.5, 2, 10 and 100 ppm PAA (15,000 g mol^{-1}) adsorption on iron (A = 0.18 cm^2) from 3 M HCl at room temperature using *R*(*QR*) *EEC*.

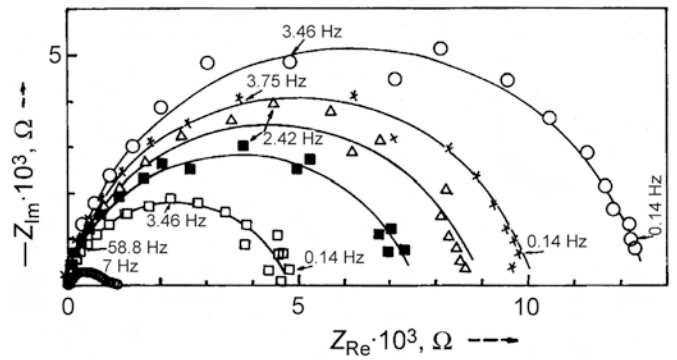

Fig. 5. Experimental (●;□;■;△;★;O) and theoretical (—) Nyquist plots for 0, 0.5, 1, 2, 5 and 100 ppm PAA (600,000 g mol^{-1}) adsorption on iron (A = 0.18 cm^2) from 3 M HCl at room temperature using *R*(*QR*) *EEC*.

The best fitting parameters for PAA adsorption on iron from 3 M HCl at the corrosion potential and room temperature were obtained using the impedance data and the Boukamp program.[10] The results are presented in Tables II and III. These data indicate the following:

i) The values of *Q* (or *C*) are strongly influenced by the PAA concentration in the solution and/or by the coverage of the metal surface (θ) with adsorbed PAA molecules (segments).[17] The limiting values of *Q* (or *C*) for $\theta \rightarrow 1$ are $\approx 26\ \Omega^{-1}\ s^n\ cm^{-2}$ or $\approx 12\ \mu F\ cm^{-2}$ (for $n \approx 0.945$) and they were found to be slightly influenced by the molecular weight of the PAA. According to the two-con-

denser model ($\theta = (C^{\theta=0} - C^{\theta}) / (C^{\theta=0} - C^{\theta=1})$), the limiting values of θ (for $c_{PAA} \rightarrow \infty$) in these cases should be between 0.91 and 0.95.

ii) The obtained values of the charge transfer resistance (R_{ct}) strongly increase in the presence of PAA in the solution, clearly indicating a significant inhibition of the corrosion process. In the absence of PAA in the solution, $R_{ct} = 150\ \Omega\ cm^2$ corresponding to $j_{corr} = 84\ \mu A\ cm^{-2}$, which in a very good agreement with literature data for corrosion rate of iron in 3 M HCl.[18] The limiting value of R_{ct} in the present cases were $\approx 1800\ \Omega\ cm^2$ and $\approx 2200\ \Omega\ cm^2$ for 15,000 g mol^{-1} and 600,000 g mol^{-1} PAA, respectively, indicating again the high degree of coverage θ of the metallic surface ($\theta > 0.9$).

iii) The value of exponent n (degree of surface homogeneity) also increases in the presence of PAA adsorbed at the metal surface by decreasing its micro inhomogeneity.

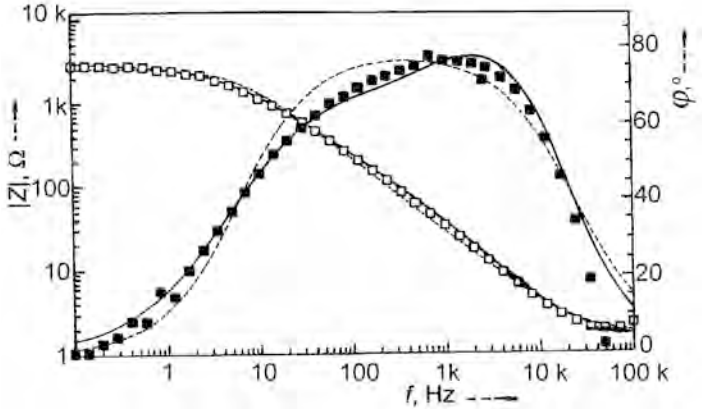

Fig. 6. Experimental and theoretical Bode plots for PAA (600,000 g mol^{-1}; 0.5 ppm) adsorption on iron (A = 0.18 cm^2) from 3 M HCl at room temperature; --- *R*(*QR*) *EEC* and — *R*{*Q*[*R*(*QR*)]} *EEC*.

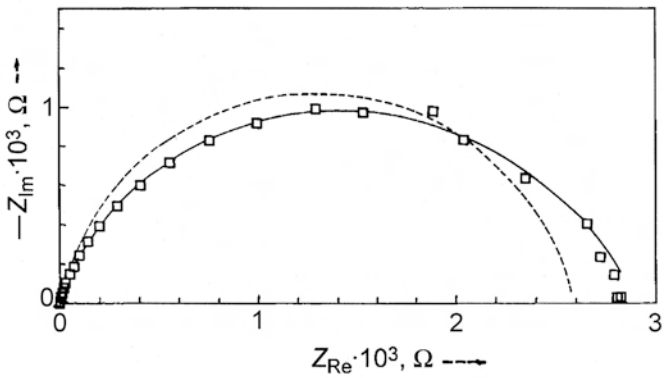

Fig. 7. Experimental and theoretical Nyquist plots for PAA (600,000 g mol^{-1}; 0.5 ppm) adsorption on iron (A = 0.18 cm^2) from 3 M HCl at room temperature;--- *R*(*QR*) *EEC* and — *R*{*Q*[*R*(*QR*)]} *EEC*.

TABLE II. Best fitting parameters for the adsorption of PAA (15,000 g mol^{-1}) on iron from 3 M HCl at the corrosion potential; 293 K

EEC	Elements of EEC	C_{PAA} / ppm								
		0	0.5	1.0	2.0	5.0	10.0	20.0	100.0	200.0
R(QR)	R_{el} / Ω cm^2	0.34	0.31	0.30	0.31	0.31	0.31	0.32	0.32	0.32
	$Q\times10^6$ / Ω^{-1} s^n cm^{-2}	220.6	83.6	59.9	47.0	40.7	35.1	31.0	27.3	25.3
	n	0.840	0.883	0.905	0.919	0.928	0.936	0.942	0.943	0.944
	R_{ct} / Ω cm^2	151	618	906	1125	1302	1471	1633	1793	1894
R{Q[R(QR)]}	R_1 / Ω cm^2		0.36	0.34	0.35	0.34	0.35	0.48	0.36	0.37
	$Q_1\times10^6$ / Ω^{-1} s^n cm^{-2}		24.0	20.3	17.4	17.0	13.4	10.9	11.1	8.5
	n_1		1	1	1	1	1	0,998	1	1
	R_2 / Ω cm^2		31.7	41.9	47.0	2.3×10^{-16}	43.7	2.5×10^{-16}	51.8	31.5
	$Q_2\times10^6$ / Ω^{-1} s^n cm^{-2}		131.7	89.2	60.6	66.8	40.4	34.2	29.9	28.8
	n_2		0.706	0.715	0.743	0.652	0.768	0.791	0.775	0.790
	R_3 / Ω cm^2		648	952	1157	1482	1511	1737	1836	1980

TABLE III. Best fitting parameters for the adsorption of PAA (600,000 g mol^{-1}) on iron from 3 M HCl at the corrosion potential; 293 K

EEC	Elements of EEC	C_{PAA} / ppm							
		0	0.5	1.0	2.0	5.0	10.0	20.0	100.0
R(QR)	R_{el} / Ω cm^2	0.34	0.30	0.31	0.30	0.31	0.30	0.32	0.32
	$Q\times10^6$ / Ω^{-1}s^n cm^{-2}	220.6	85.6	44.4	41.4	36.1	32.2	30.0	28.9
	n	0.840	0.887	0.930	0.930	0.938	0.945	0.944	0.943
	R_{ct} / Ω cm^2	151	450	1152	1503	1710	1980	2088	2160
R{Q[R(QR)]}	R_1 / Ω cm^2		0.35	0.38	0.34	0.34	0.34	0.35	0.35
	$Q_1\times10^6$ / Ω^{-1}s^n cm^{-2}		20.6	9.6	15.7	15.1	14.0	13.4	14.1
	n_1		1	0.990	1	1	1	1	1
	R_2 / Ω cm^2		21.8	2.2×10^{-16}	40.5	43.6	42.7	47.2	61.7
	$Q_2\times10_6$ / Ω^{-1}s^n cm^{-2}		176.1	81.7	52.8	42.2	36.1	29.9	28.8
	n_2		0.681	0.690	0.735	0.747	0.755	0.733	0.758
	R_3 /Ω cm^2		497	1413	1586	1795	2034	2151	2205

DISCUSSION

As was shown by the EIS measurements of the Fe/3 M HCl (PAA) interface, Tables II and III, the value of the minimum capacitance depends mainly on the concentration and molecular weight of the polymer. On the other hand, it was also confirmed that the limiting value of the minimum capacitance (12 μF cm^{-2} for $\theta = 1$) and the effective thickness of the adsorbed layer (1.1 ± 0.05 nm; for $\varepsilon_r = 15$) are insignificantly affected by the molecular weight of the polymer.

In accordance with these statements, it follows that impedance measurements are not sufficient for the determination of the surface concentration (mol cm^{-2}) of the polymer adsorbed at the metal surface (or the surface area occupied by each adsorbed PAA molecule, σ_{PAA} / nm^2), nor the thickness of the adsorbed layer.

However, assuming the same conformations for polymer coil in the solution and in the adsorbed state at the metal surface, several basic parameters, such as surface concentration of the adsorbed polymer (c_s for θ = 1), volume and/or weight of the adsorbed polymer coil (v_c and/or m_c) and the polymer concentration in the coil (wt % PAA$_c$) can be calculated ($R_G = 7.49\times10^{-3}\times \overline{M}_n^{0.64}$ / nm[9]; $R_G^2 \times\pi$/nm^2; $v_c = 4/3\ R_G^3\times\pi$; $m_c = \overline{M}_n/N$; wt. % PAA$_c$ = $m_c/(v_c\ \rho_{sol})\times100$). These values are presented in Table IV.

TABLE IV. Basic parameters for the statistical polymer coil in solution and/or at the metallic surface (assuming a spherical polymer coil)

$\overline{M}_n$ / g mol^{-1}	R_G / nm	σ / nm^2	c_s / mol cm^{-2}	(θ=1) / mg cm^{-2}	v_c / cm^3	m_c / g	w % PAA$_c$
15,000*	3.53*	39.0*	4.28×10^{-12}*	6.42×10^{-5}*	1.84×10^{-19}*	2.49×10^{-20}	≈ 13*
85,000*	10.7*	359.6*	4.62×10^{-13}*	3.93×10^{-5}*	5.13×10^{-18}*	1.41×10^{-19}	≈2.6*
200,000	18.5	1075	1.54×10^{-13}	3.09×10^{-5}	2.65×10^{-17}	3.32×10^{-19}	≈1.19
600,000	37.37	4387	3.78×10^{-14}	2.27×10^{-5}	2.19×10^{-16}	9.96×10^{-19}	≈0.43
1,350,000	62.8	12386	1.34×10^{-14}	1.81×10^{-5}	1.04×10^{-15}	2.24×10^{-18}	≈0.2

It should be mentioned that empirical equation for calculating R_G (given above) was obtained using viscosimetric and/or sedimentation data of dilute solutions of relatively high molecular weight PAA[9] and consequently its application for much lower values of $\overline{M}_n$ (such as 15,000 and 85,000 g mol^{-1}*, Table IV) is questionable.

Evidently, the surface concentration of adsorbed polymer (c_s) is a function of the molecular weight of the polymer and follows the equations:

$$c_s = 9.6\times10^{-7}\times \overline{M}_n^{-1.28} \text{ or } c_s = 5.313\times10^{-11}/R_G^2 \text{ (mol cm}^{-2}\text{)} \qquad (8)$$

where R_G is given in nm.

The same type of empirical equation has already been obtained for the adsorption of many other polymers, mainly at non-metallic surfaces,[16] and implies that the quantity (c_s) of the adsorbed layer, as well as its thickness should depend on the molecular weight of the polymer (Table IV).

On the other hand, the thickness of the adsorbed polymer layer of about 1.1 nm, determined by impedance measurements (for ε_r = 15) corresponds only to the polymer segments directly attached to the metal surface. The other parts of the adsorbed polymer coils (loops and tails) do not significantly contribute to the value of the measured capacitance due to the very low participation of the polymer material (≤ 1 %) in the overall volume of the coil ($\varepsilon_{r,coil} \approx \varepsilon_{r,sol}$). Thus, the

sharp decrease of the dielectric constant (from $\varepsilon_{r,sol} \approx 80$ to $\varepsilon_{r,ads} \approx 15$) occurs in the thin layer of polymer segments adsorbed at the metallic surface.

Relatively high degree of coverage ($\theta > 0.7$) or high "protection" efficiency of the metallic surface most probably results from further involvement of the polymer molecules in the adsorbed layer causing its additional structuring (slow process). Therefore, in the state of limiting coverage, the adsorbed layer is highly voluminous and relatively tick (100 – 200 nm), as it was found by elipsometry,[6,19] and contains entangled polymer coils.

CONCLUSIONS

1. It was found that the efficiency of corrosion protection by adsorbed layers of PAA strongly depends both on the molar concentration of PAA in the solution and its molecular weight, reaching the limiting values between 85 and 96 %. Simultaneously, it was also concluded that a relatively high value of surface coverage can be obtained with very low concentrations of PAA (0.5 – 2 ppm), indicating the good adsorption characteristics of PAA on mild steel and iron in hydrochloride acid.
2. The experimentally obtained results follow a Langmuir adsorption isotherm. According to the best fitting parameters, the adsorption coefficient B ranged between 2×10^7 and 4×10^8 mol^{-1} and strongly depended on the molecular weight of the PAA, $B = k\times \overline{M}_n^{\alpha}$ (for $\alpha \approx 0.67$ and $k = 2.95\times10^4$), or the size of the polymer coil.
3. As found by EIS, the thickness of the adsorbed PAA layer was approx. 1.1 nm (for $\varepsilon_r = 15$), which corresponds only to the polymer segments attached to the metal surface. On the other hand, as found by ellipsometry, the limiting layer of adsorbed PAA molecules was highly voluminous and relatively thick (100 – 200 nm), containing entangled polymer coils.
4. It was also found that the degree of coverage or inhibition efficiency of the metal surface with adsorbed PAA molecules (segments) was strongly influenced by the molecular weight of the PAA, following the relation:

$$B_1/B_2 \equiv (\theta_1/\theta_2)_c \equiv R_{G1}/R_{G2} \equiv (\overline{M}_{n1}/\overline{M}_{n2})^{0.67}$$

where B is the adsorption coefficient and R_G the radius of gyration of the statistical polymer coil in solution.

ИЗВОД

ИХИБИЦИЈА КОРОЗИЈЕ ГВОЖЂА У ХЛОРОВОДОНИЧНОЈ КИСЕЛИНИ ПОЛИАКРИЛАМИДОМ

DRAGICA CHAMOVSKA, MAJA CVETKOVSKA и TOMA GRCHEV

Faculty of Technology and Metallurgy, St. Cyril and Methodius University, 1000 Skopje, FYRO Macedonia

Испитивана је корозиона заштита и/или адсорпција полиакрил-амида (ПАА) средње моларне масе $\overline{M}_n = 15000 – 1350000$ g mol^{-1} на меком челику и гвожђу (99,99 % Fe) у 3 M HCl на собној температури коришћењем спектрофотометрије (фенантролинска метода), методе губитка масе и спектроскопије електрохемијске импеданције (СЕИ). Утврђено је да

ефикасност корозионе заштитите адсорбованог слоја ПАА јако зависи од концентрације ПАА у раствору и његове молекулске масе, достижући граничну вредност између 85 и 96 %. Такође је показано да се релативно високе вредности степена покривености могу добити при веома ниским концентрацијама ПАА (0,5 – 2 ppm), што указује на добре адсорпционе карактеристике ПАА на меком челику и гвожђу у раствору HCl. Експериментално добијене вредности степена покривености следе Ленгмирову адсорпциону изотерму. Адсорпциони коефицијент, B, се креће од 2×10^7 до 4×10^8 mol^{-1} и зависи од величине полимерног клупка, односно од средње моларне масе ПАА према једначини $B = k\times \overline{M}_n^{\alpha}$ (где је $\alpha \approx 0{,}67$ и $k = 2{,}95\times10^4$). Као што су мерења методом СЕИ показала, дебљина адсорбованог слоја ПАА је око 1,1 nm (за $\varepsilon_r = 15$) и одговара сегментима полимерног ланца адсорбованим на површини метала. С друге стране, раније је показано елипсометријском методом да је гранични слој адсорбованих молекула ПАА изразито волуминозан и релативно дебео (100 – 200 nm) и да садржи замршене полимерне ланце.

(Примљено 3. августа 2006, ревидирано 15. фебруара 2007)

REFERENCES

1. B. Vincent, ACS Symposium Series 240, *Polymer Adsorption and Dispersion Stability*, Eds. E.D.Goddard, B.Vincent, Amer. Chem. Soc., Washington D.C., 1984 p.3
2. The Patent Office, London, Patent specification 1, 133,382;28 February 1966, No. 8607–66 (1966)
3. A. El–Sayed, *Corr. Prevent. Control* **43** (1996) 27
4. M. Mekki Daouadji, N. Chelali, *J. Appl. Polym. Sci.* **91** (2004) 1275
5. G. G. Parfitt, C. H. Rochester, *Adsorption from Solution at the Solid-Liquid Interface*, Eds. G. G. Parfitt, C. H. Rochester, Ch. 4, Academic Press, New York, 1983
6. Lj. Arsov, T. Grchev, M. Cvetkovska, Gj. Petrov, *Bull. Soc. Chim.*, Beograd 48 (1983) 417
7. A. Silberberg, *J. Phys. Chem.* **66** (1962) 1872
8. T. Grchev, M. Cvetkovska, 36th ISE Meeting, Ext. Abst. 06070, Salamanca, 1985
9. T. Schwartz, J. Francois, G. Weill, *Polymer* **21** (1980) 247
10. B. A. Boukamp, Solid State Ionics 20 (1986) 31
11. S. Sathiyanarayanan, S. K. Dhawan, D. C. Trivedi, K. Balakrishnan, *Corros. Sci.* **33** (1992) 1831
12. T. Grchev, M. Cvetkovska, T. Stafilov, J. W. Schultze, *Electrochim. Acta* **36** (1991) 1315
13. T. Grchev, M. Cvetkovska, J. W. Schultze, *Corros. Sci.* **32** (1991) 103
14. D. Chamovska, *Ph.D. Thesis*, Sts. Cyril and Methodius University, Skopje, R. Macedonia (2000)
15. E. Collinson, F. S. Daiton, G. S. McNaughton, *Trans. Faraday. Soc.* **53** (1957) 489
16. Yu. S. Lipatov, L. M. Sergeeva, *Adsorption of Polymers*, Ch. 3, John Wiley & Sons, NewYork, 1974
17. K.S. Khairou, A. El–Sayed, *J. Appl. Polym. Sci.* **88** (2003) 866
18. J. O`M. Bockris, B. Yang, *J. Electrochem. Soc.* **138** (1991) 2237
19. A. Takahashi, M. Kawaguchi, K. Hayashy, T. Kato in: *Polymer Adsorption and Dispersion Stability*, Amer. Chem. Soc. (1984) 39.

J. Serb. Chem. Soc. 72 (7) 699–708 (2007) UDC 66.094.1+546.92:544.35:66–911.48
JSCS–3603 *Original scientific paper*

Oxygen reduction at platinum nanoparticles supported on carbon cryogel in alkaline solution

N. R. ELEZOVIĆ[1]*#, B. M. BABIĆ[2], LJ. M. VRAČAR[3]# and N. V. KRSTAJIĆ[3]

[1]*Center for Multidisciplinary Studies, University of Belgrade, P.O. Box 33, Belgrade,* [2]*Vinča Institute of Nuclear Sciences, P.O. Box 522, 11001 Belgrade and* [3]*Faculty of Technology and Metallurgy, University of Belgrade, Belgrade, Serbia*

(Received 19 October 2006, revised 17 January 2007)

Abstract: The oxygen reduction reaction was investigated in 0.1 M NaOH solution, on a porous coated electrode formed of Pt particles supported on carbon cryogel. The Pt/C catalyst was characterized by the X-ray diffraction (XRD), transmission electron microscopy (TEM) and cyclic voltammetry techniques. The results demonstrated a successful reduction of Pt to metallic form and homogenous Pt particle size distribution with a mean particle size of about 2.7 nm. The ORR kinetics was investigated by linear sweep polarization at a rotating disc electrode. The results showed the existence of two E – log j regions, usually referred to polycrystalline Pt in acid and alkaline solution. At low current densities (lcd), the Tafel slope was found to be close to $-2.3RT/F$, while at high current densities (hcd) it was found to be close to $-2\times2.3RT/F$. It is proposed that the main path in the ORR mechanism on Pt particles was the direct four-electron process, with the transfer of the first electron as the rate determining step. If the activities are expressed through the specific current densities, a small enhancement of the catalytic activity for Pt/C was observed compared to that of polycrystalline Pt. The effect of the Pt particle size on the electrocatalysis of oxygen reduction was ascribed to the predominant (111) facets of the platinum crystallites.

Keywords: oxygen reduction reaction, Pt nanoparticles, carbon support, alkaline solutions

INTRODUCTION

The oxygen reduction reaction is one of the most important electrochemical reactions because it is the cathodic reaction in fuel cells and metal air batteries, during aerated media corrosion and in some industrial electrolytic processes. For these reasons, research efforts have been focused on developing a proper catalyst and elucidating the mechanism of this reaction.[1–8] Platinum and platinum alloys are, in spite of efforts to replace them, still the best known electrocatalysts for the oxygen reduction reaction, since they have a high catalytic activity and chemical

* Corresponding author. E-mail: nelezovic@tmf.bg.ac.yu
# Serbian Chemical Society member.
doi: 10.2298/JSC0707699E

stability. Nowdays, researchers are mostly dealing with precious metals, mainly platinum and its alloys, dispersed on high surface area carbon, and their efforts are concentrated on the reduction of the amount of Pt.[9,10]

The electrochemical oxygen reduction reaction has been extensively studied in acid solutions, due to its application in fuel cells with a proton exchange membrane. However, there are few works in alkaline solution,[11–13] especially on platinum nanoparticles.[14,15] According to many authors, the electrochemical reduction of oxygen on Pt occurs by the parallel mechanism with predominantly direct four-electron reduction, even in alkaline solutions. The steady state kinetics in acid solution is characterized by two linear Tafel slopes: $-2.3RT/F$ at low current densities and $-2\times2.3RT/F$ at high current densities. The change in Tafel slopes is, generally, a consequence of a change in the rate determining steps (rds). However, many workers agreed that the different Tafel slopes arose from different adsorption conditions of the reaction intermediates in these two cd regions and that the same first charge transfer step was the rds in both current densities regimes.[2,16–18]

In this study the oxygen reduction reaction was investigated on a Pt/C electrode in alkaline electrolyte and results are compared to those on polycrystalline Pt. Namely, the development of alkaline anion exchange membranes is well advanced[19,20] and such membranes will enable the benefits of the kinetics of the oxygen reduction reaction in alkaline solutions to be employed.

EXPERIMENTAL

Carbon support and catalyst preparation

Home made carbon cryogel synthesized by sol−gel polycondensation and freeze-drying with a specific surface area (BET) of 517 $m^2\ g^{-1}$ was used as a catalyst support.[21] The Pt was deposited on the support by a modified ethylene glycol method.[22]

Electrode preparation

The catalyst ink was prepared using one milligram of Pt/C catalyst ultrasonically suspended in 1.0 ml of a water–methanol mixture (v/v : 1/1) and 50 µl of Nafion solution (5 wt. % solution, Aldrich). Then 12.5 µl of ink was transferred by an injector to a clean gold disk electrode (6 mm diameter, with area of 0.28 cm^2). After volatilization of the water–methanol, the electrode was heated at 80 °C for 10 min.

Characterization of the catalyst

X-Ray diffraction (XRD) analysis, performed on a Siemens D500 X-ray diffractometer using CuKα radiation with a Ni filter, was used for the characterization of the Pt/C catalyst powder. The 2θ angular regions between 5 and 70° were explored at a scan rate of 0.02° s^{-1} with an angular resolution of 0.02° for all XRD tests.

Transmission electron microscopy (TEM) measurements were performed at the National Center for Electron Microscopy (NCEM)[23] using a PEI Phillips instrument. The suspension for transmission electron microscopy, prepared from catalyst powder and ethanol, was dropped onto a clean holey carbon grid and dried in air. The particle size distribution was determined from images of, on average, 20 different regions containing 10 – 20 particles each. The particle shape was determined

by real space crystallography using high-resolution images taken from particles near or on the edge of the carbon black substrate and/or by numerical Fourier filtering of the digitized image intensity spectrum of particles on the top of the carbon.

Electrochemical characterization

A conventional RDE three-compartment all-glass cell was used. The counter electrode was a platinum sheet of 5 cm^2 geometric area. A reversible hydrogen electrode, in the same solution, was used as the reference electrode. The working electrode used in this study was in the form of a rotating disk. The experiments were performed at 25 °C. The electrolytes were 0.1 M NaOH and 0.1 M $HClO_4$ prepared with highly pure water.

The experiments were performed by the potentiodynamic method. A PAR Universal Programmer, Model 175, was used to provide potentiodynamic voltage–time program addressed to a PAR Model 371 Potentiostat/Galvanostat.

RESULTS AND DISCUSSION

XRD and TEM characterization of the catalyst

The XRD results[24] showed three characteristic reflection peaks in all spectra: the peak at $2\theta = 44.2°$ corresponds to the hexagonal graphite structure (100) and the diffraction peaks at about 39°, 46° and 68° correspond to the Pt (111), (200) and (220) planes, respectively. The first peak suggests good graphite characteristics of the carbon cryogel and the diffraction peaks of the fcc Pt demonstrate a successful reduction of the Pt precursor to the metallic form and it represents the typical character of a crystalline Pt face that is in the face-centered cubic (fcc) phase. As there are no other distinct peaks in the investigated 2θ range than the three Pt peaks mentioned above, it can be concluded that all the in-house supported Pt catalysts had a prevailing Pt (fcc) crystal structure.

TEM Micrograph shows very uniform size distribution of the Pt nanoparticles (Fig. 1a), with a mean particle size of about 2.7 nm for the supported Pt catalyst. The atomically resolved image in Fig. 1b shows Pt lattice planes with a spacing corresponding to the (200) and (111) planes of the face-centered cubic Pt nanoparticles, as was indicated in the relevant digital diffractogram. The Pt particles have common cubo-octahedral shapes. Occasionally, twinned particles were observed with the same (111) twinning plane as in some other Pt-based catalysts.[23]

Cyclic voltammetry analysis

The cyclic voltammograms obtained at a Pt/C electrode in N_2 saturated 0.5 M $HClO_4$ and in N_2 saturated 0.1 M NaOH solutions, performed to determine the electrochemically active surface area and to compare the adsorption properties of the catalyst in acid and alkaline solutions, are presented in Fig. 2a and Fig. 2b, respectively. The double layer region in the alkaline solution was not well-defined as in the acid solution, which was also found for Pt single crystal electrodes.[11] The voltammograms in both acid and alkaline solutions also indicate

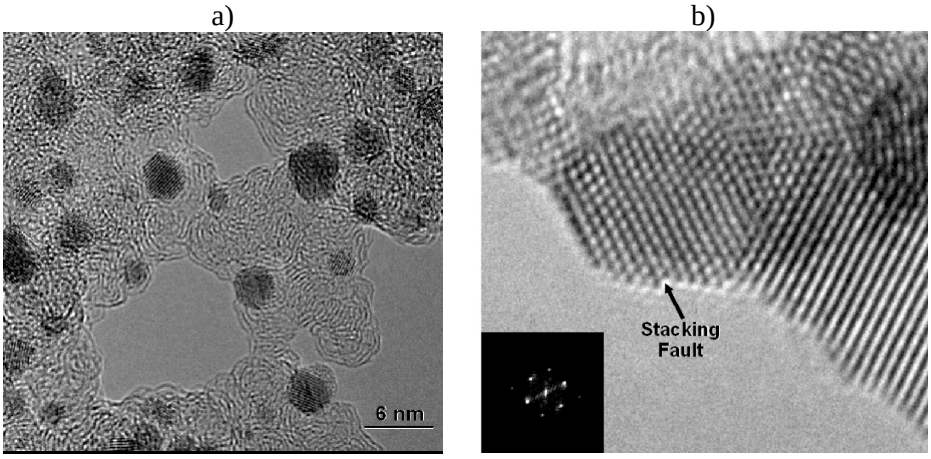

Fig. 1. TEM Images of Pt nanoparticles on carbon substrate. a) An overview showing the distribution of the sizes of the Pt particles on carbon support; b) high resolution image showing a cubo-octahedral shape of Pt particle.

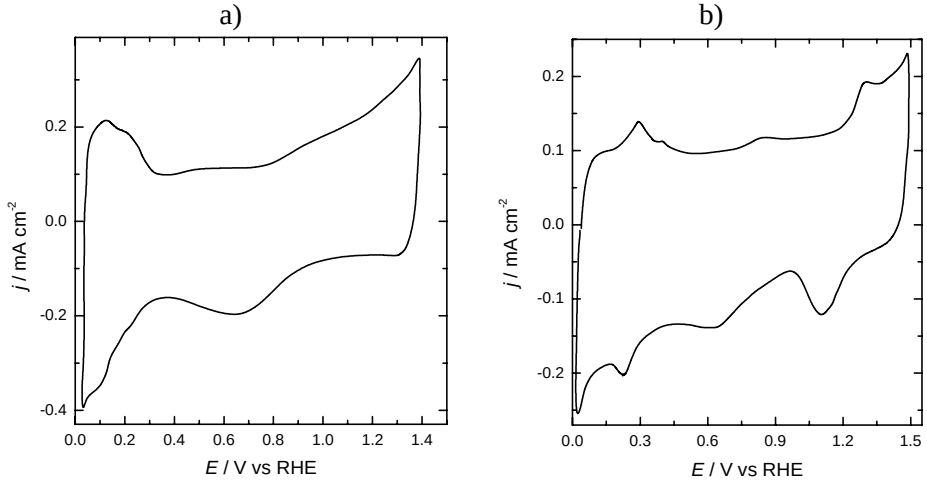

Fig. 2. Cyclic voltammetry curves for Pt/C in: a) N_2 saturated 0.5 M $HClO_4$ solution and b) N_2 saturated 0.1 M NaOH, at a sweep rate of 100 mV s^{-1}.

that there are some differences in the features of the hydrogen desorption process, with respect to those of polycrystalline Pt. In the acid solution, the hydrogen oxidation peak, corresponding to the desorption of the hydrogen atoms from the edge and corner sites of the platinum crystallites, was pronounced[25–27] and this could be attributed to the fact that small platinum particles show an increased number of edge and corner sites, which is a consequence of the change of the fraction of the atomic surface of the (111) and (100) faces.[26] This is consistent with

the fact that for smaller particles, the fraction of the atomic surface of Pt atoms in the (111) face is higher than those for the other orientations.[26] The unclear separation of the hydrogen, oxygen and double layer regions in alkaline solution is a consequence of the fact that the adsorption of oxygen-containing species on different Pt facets starts at potentials close to the hydrogen region. This is the reason why the anodic part of the CV curve is not fully parallel with the potential axis in the conventional double layer region. As a consequence of all this, the desorption charge of hydrogen atoms, after extraction of the double layer charge, was found to be lower in the alkaline solution, as was already reported in the literature.[12] On account of these differences, the real electrode surface area of the Pt catalyst was determined by integrating the charge under the hydrogen desorption curve in acid solution (Fig. 2a), taking the reference value of 210 μC cm^{-2} for full coverage with adsorbed hydrogen species.[28] This calculation gave the value of 68 m^2 g^{-1} for Pt/C electrode.

Kinetics of the oxygen reduction reaction

The rotating disk electrode measurements of the ORR in 0.1 M NaOH were performed to test the catalytic activity of the Pt/C catalyst and compare it with that of polycrystalline Pt. The rotating disk electrode voltammogram of Pt/C in O_2-saturated NaOH solution, at a sweep rate of 20 mV s^{-1}, as a function of the rotation rate is shown in Fig. 3. It can be seen that the onset of the ORR and the half-wave potential were significantly shifted to more positive potentials in the case of the Pt/C electrode, indicating its higher catalytic activity for the reduction of oxygen, compared to that of polycrystalline Pt (Fig. 4). For a mixed control process, the activation and mass-transport controlled current densities are combined to yield the total current density as the sum of reciprocals:

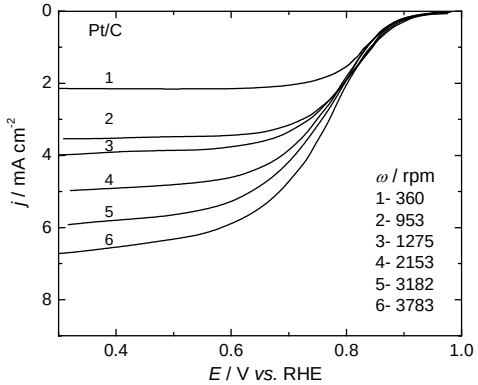

Fig.3. Polarization curves obtained with a rotating disk electrode for O_2 reduction in 0.1 M NaOH solution at Pt/C electrode, at sweep rate of 20 mV s^{-1}.

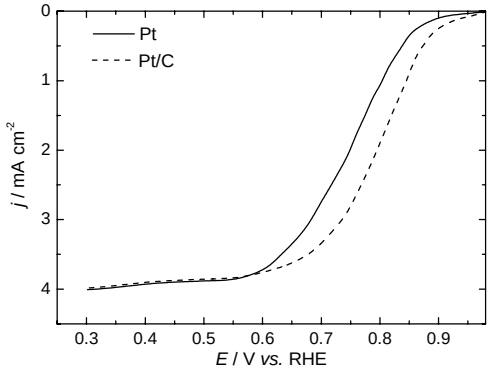

Fig.4. Polarization curves for O_2 reduction on Pt and Pt/C in 0.1 mol dm^{-3} NaOH solution, at a rotating speed of 1280 rpm, with sweep rate of 20 mV s^{-1}.

$$\frac{1}{j} = \frac{1}{j_k} + \frac{1}{B\omega^{1/2}} \tag{1}$$

where j is the measured current density, j_k is the activation controlled current density, ω is the rotation rate of the electrode and B is the Levich slope, the theoretical value of which is given by the Equation:

$$B = 0.62\, n F\, C(O_2) D_{O_2}^{2/3} \nu^{-1/6} \tag{2}$$

where: n is the number of electrons transferred per oxygen molecule, F is the Faraday constant, D_{O_2} is the diffusion coefficient of oxygen (2.22×10^{-5} cm^2 s^{-1}), ν is the kinematics viscosity of the solution (1.1×10^{-2} cm^2 s^{-1}) and $C(O_2)$ is the bulk concentration of oxygen molecules (1.13×10^{-6} mol cm^{-3}). The values of these coefficients are referred to a 0.1 mol dm^{-3} NaOH solution.[29]

From the Koutecky–Levich plots (Eq. (1)), the kinetic currents of oxygen reduction can be calculated from the intercepts of the j^{-1} *vs.* $\omega^{-1/2}$ lines. From the slopes of the lines, the constant B and the number of the electrons exchanged in the reduction can be obtained.

The I^{-1} *vs.* $\omega^{-1/2}$ plots at different potentials for the Pt/C electrode are presented in Fig. 5. These plots are parallel, indicating first order kinetics with respect to molecular oxygen.[30] The slope of these plots gives the value of constant B = 0.021 mA rpm$^{-1/2}$. This value is in good agreement with the theoretical value of 0.019 mA rpm$^{-1/2}$ calculated for a four-electron reduction of oxygen in 0.1 mol dm^{-3} NaOH solution.

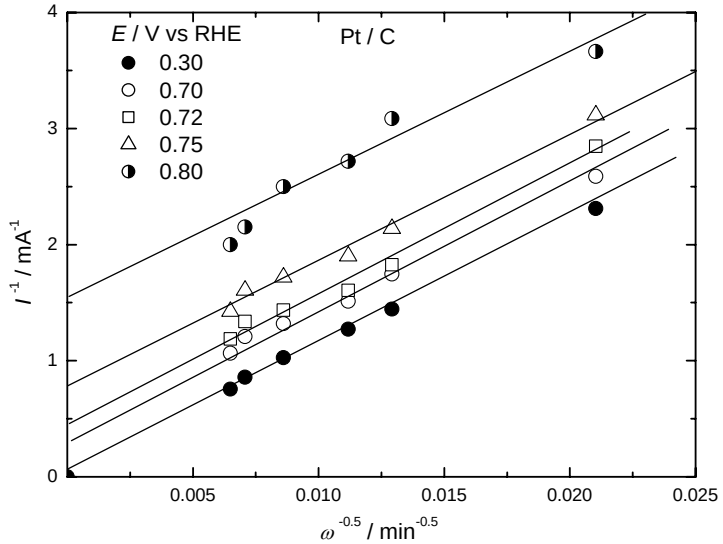

Fig.5. Koutecky−Levich plots for Pt/C electrode at different potentials, obtained from the data in Fig. 3.

The Tafel plots for Pt/C and polycrystalline Pt, obtained from the kinetic currents, are presented in Fig. 6. The current densities were normalized to the electrochemical active surface area (for the polycrystalline Pt, the experimentally determined roughness factor of 2.5 was used). Both electrodes are characterized by two Tafel slopes: one close to $-2.3\times2RT/F$ at high current densities and the other close to $-2.3RT/F$ at low current densities, usually referenced for polycrystalline Pt in alkaline solution.[11]

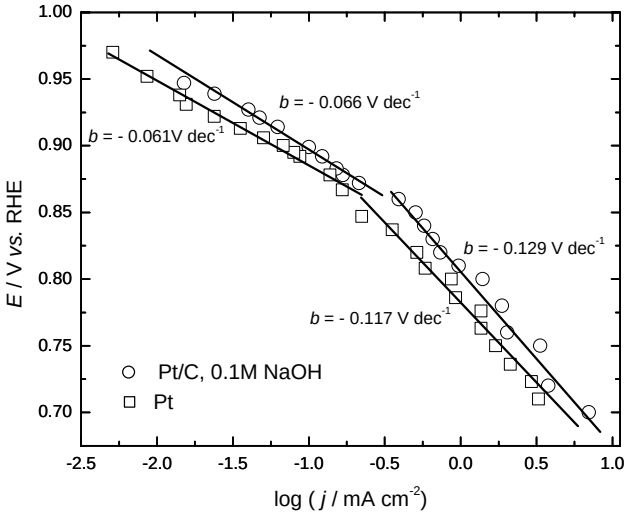

Fig.6. Tafel plots normalized to the electrochemically active surface area for O_2 reduction in 0.1 M NaOH solution at Pt and Pt/C electrodes.

These results show that the kinetics of oxygen reduction on the Pt/C electrode in alkaline solution is described by the same Equations as those on Pt, and also that the four-electron reduction mechanism, with the first charge transfer rate as the rate determining step, is operative over the whole range of potential.

The existence of two slopes for both electrodes could be explained in terms of the coverage of the electrode surface by adsorbed oxygen species, which follows a Temkin isotherm in the low current density region and a Langmuir isotherm in the higher current density region, meaning that the adsorption conditions are the same on both electrodes.

Based on literature data,[1–3,9] the ORR on platinum in aqueous solutions has generally been explained by a mechanism involving two parallel paths: in the main one, oxygen is reduced directly to OH^- by a four-electron transfer and in the second one, HO_2^- is first formed by a two-electron transfer process, followed by its further reduction. Numerous investigations of the ORR were performed using of rotating ring-disk electrode, because it is practically the only reliable way to propose the mechanism of the ORR. Therefore, Koutecky–Levich analy-

sis presents an alternate way to rotating ring-disk electrode measurements in the analysis of the actual reaction path. On the basis of this analysis, according to the number of electrons exchanged, the direct four electron mechanism, or at least that the reduction of H_2O_2 is a very fast process, can be proposed.

Lima and Ticianelli[31] reported that the four electron mechanism predominates for Pt/C catalysts with more than 20 % of platinum on carbon. The same conclusion was drawn by Genies *et al.*,[13] who proved that oxygen reduction on carbon was mainly a two-electron process but that on platinum particles, the importance of this path was so small that it was difficult to be fully characterized by RRDE experiments.

The comparison of the specific activities of Pt/C and Pt electrodes for the ORR (Fig. 6) reveals a small enhancement of the catalytic activity for Pt/C. This result seems to be related to the weak adsorption of oxygenated species on the small particles, as the effect of corner and edge atoms, the proportion of which increases for small particles. The present results are in agreement with the results of Markovic *et al.*,[32] who also showed that, the Pt (111) face is the most active for the OOR in alkaline solution. Since the proportion of (111) *vs.* (100) increases for smaller particles, they predicted a slight increase in activity for these particles.

CONCLUSIONS

A highly dispersed carbon supported Pt catalyst with a loading of 20 wt. % Pt was successfully synthesized. Comparison with polycrystalline Pt showed a slight enhancement in the catalytic activity for the oxygen reduction reaction, expressed through the electrochemically active surface area. Kinetics and mechanism of the reaction at Pt/C catalyst were found to be the same as in a case of polycrystalline Pt. The results presented above did not show a promising increase in the specific catalytic activity but illustrated that Pt nanoparticles supported on carbon cryogel can be employed as a catalyst for the ORR.

Acknowledgement: The authors are indebted to the Ministry of Science and Environment Protection Republic of Serbia for the financial support of this work under the Contract number 142038

И З В О Д

ЕЛЕКТРОХЕМИЈСКА РЕАКЦИЈА РЕДУКЦИЈЕ КИСЕОНИКА НА НАНОЧЕСТИЦАМА ПЛАТИНЕ НА УГЉЕНИЧНОМ НОСАЧУ У АЛКАЛНОМ РАСТВОРУ

Н. Р. ЕЛЕЗОВИЋ[1], Б. М. БАБИЋ[2], Љ. М. ВРАЧАР[3] и Н. В. КРСТАЈИЋ[3]

[1]Центар за мултидисциплинарне студије Универзитета у Београду, Београд, [2]Институт за нуклеарне науке "Винча", Београд и [3]Технолошко–металуршки факултет Универзитета у Београду, Србија

Кинетика реакције редукције кисеоника је испитивана на наночестицама платине диспергованим на угљеничном носачу, у 0.1 mol dm^{-3} NaOH, на 25 °C. За синтезу Pt катализатора (Pt/C) је примењена модификована полиол метода из раствора етилен гликола, док је као носач коришћен угљенични криогел. Тако добијени катализатор је окарактерисан применом BET методе, дифракције X-зрака (XRD) и трансмисионе електронске микроскопије (TEM).

Добијени резултати су показали веома хомогену расподелу наночестица Pt, са просечном величином честица око 2,7 nm. За испитивање кинетике реакције редукције кисеоника су коришћене стационарна поларизациона метода и метода цикличне волтаметрије. Показано је да област малих густина струје на кривој поларизације карактерише вредност Тафеловог нагиба око –60 mV dek^{-1}, док је у области већих густина струје ова вредност блиска –120 mV dek^{-1}. Према доијеним резултатима, главни реакциони пут у механизму редукције кисеоника је директна четвороелектронска измена, при чему је ступањ који одређује укупну брзину реакције пренос првог електрона. Поређењем каталитичке активности, изражене преко густине струје по реалној површини катализатра, констатована је нешто већа активност Pt/C катализатора у односу на поликристалну Pt, што је последица доминације (111) равни у кристалној структури дисперговане платине.

(Примљено 19. октобра 2006, ревидирано 17. јануара 2007)

REFERENCES

1. S. Gottsfeld, T. A. Zawodzinski, *Advances in Electrochemical science and Engineering*, R. C. Alkire, D. M. Kolb, Eds., Vol. 5, Wiley–VCH, Weinhim (1997)
2. M. R. Tarasevich, *Elektrokhimiya* **9** (1973) 599
3. P. N. Ross, *J. Electrochem. Soc*. **126** (1979) 78
4. D. B. Šepa, M. V. Vojnović, A. Damjanović, *Electrochim. Acta* **25** (1980) 1491
5. D. B. Šepa, M. V. Vojnović, Lj. M. Vračar, A. Damjanović, *Electrochim. Acta* **31** (1986) 91
6. T. J. Schmidt, V. Stamenković, M. Arenz, N. M. Marković, P. N. Ross, *Electrochim. Acta* **47** (2002) 3765
7. M. D. Obradović, B. N. Grgur, Lj. M. Vračar, *J. Electroanal. Chem.* **548** (2003) 69
8. J. Prakash, H. Joachin, *Electrochim. Acta* **45** (2000) 2289
9. U. A. Paulus, T. J. Schmidt, H. A. Gasteiger, R. J. Behm, *J. Electroanal. Chem*. **495** (2001) 134
10. J. Zhang, Y. Mo, M. B. Vukmirovic, R. Klie, K. Sasaki, R. R. Adzic, *J. Phys. Chem. B* **108** (2004) 10955
11. T. J. Schmidt, V. Stamenkovic, P. N. Ross Jr., N. M. Markovic, *Phys. Chem. Chem. Phys*. **5** (2003) 400
12. K. Tammevski, M. Arulepp, T. Tenno, C. Ferrater, J. Claret, *Electrochim. Acta* **42** (1997) 2961
13. J. Perez, E. R. Gonzalez, E. A. Ticianelli, *Electrochim. Acta* **44** (1998) 1329
14. L. Genies, R. Faure, R. Durand, *Electrochim. Acta* **44** (1998) 1314
15. L. Genies, Y. Bultel, R. Faure, R. Durand, *Electrochim. Acta* **48** (2003) 3879
16. Lj. M. Vračar, N. V. Krstajić, V. R. Radmilović, M. M. Jakšić, *J. Electroanal. Chem*. **587** (2006) 99
17. A. Damjanović, D. B. Šepa, M. V. Vojnović, *Electrochim. Acta* **24** (1979) 887
18. D. B. Šepa, M. V. Vojnović, Lj. M. Vračar, A. Damjanović, *Electrochim. Acta* **32** (1987) 129
19. J. R. Varcoe, R. C. T. Slade, in *Fuel Cells*, Vol. 5, Issue 2, Wiley–VCH, 2005, p.187
20. K. Matsuoka, Y. Iriyama, T. Abe, M. Matsuoka, Z. Ogumi, *J. Power Sources* **150** (2005) 27
21. B. Babić, D. Đokić, N. Krstajić, *J. Serb. Chem. Soc*. **70** (2005) 21
22. B. M.Babic, Lj. M. Vračar, V. Radmilović, N. V. Krstajić, *Electrochim. Acta* **51** (2006) 3820
23. V. Radmilovic, T. J. Richardson, S. J. Chen, P. N. Ross, *J. Catal.* **232** (2005) 99
24. N. R. Elezović, B.M. Babić, N. V. Krstajić, Lj. M. Gajić–Krstajić, Lj. M. Vračar, *Int. J. Hydrogen Energy* (2006) in press
25. G. Tamizhmani, J. P. Dodelet, D. Guay, *J. Electrochem. Soc*. **143** (1996) 18
26. K.Kinoshita, *J. Electrochem. Soc*. **137** (1990) 845
27. S. Mukejee, *J. Appl. Electrochem*. **20** (1990) 537

28. C. H. Hamann, A. Hamnett, W. Vielstich, *Electrochemistry*, Wiley–VCH, 1998, p. 245
29. R. C. Weastled, *Handbook of Chemistry and Physics* 55th Ed. R. C West, Cleveland, Oh., 1984.
30. S. Mukejee, S. Srinivasan, *J. Electroanal. Chem.* **350** (1993) 201
31. F. H. B. Lima, E. A.Ticianelli, *Electrochim. Acta* **49** (2004) 4091
32. N. Markovic, H. Gasteiger, P. N. Ross, *J. Electrochem. Soc*.**144** (1997)1591.

J. Serb. Chem. Soc. 72 (7) 709–712 (2007) UDC 547.261+66.094.3+544.032.4:541.124
JSCS–3604 *Extended abstract*

EXTENDED ABSTRACT

The kinetics and mechanism of methanol oxidation on Pt and PtRu catalysts in alkaline and acid media*

JELENA LOVIĆ#

ICTM–Department of Electrochemistry, Njegoševa 12, 11001 Belgrade, Serbia

(Received 29 January 2007)

Abstract: The kinetic of methanol electrochemical oxidation for a series of platinum and platinum–ruthenium catalysts was investigated. A correlation between the beginning of OH_{ad} adsorption and methanol oxidation was demonstarated on Pt single crystals and Pt nanocatalyst. The activity of the nano-structured Pt catalyst was compared with single crystal platinum electrodes assuming the Kinoshita model of nanoparticles. The ruthenium-containing catalysts shifted the onset of methanol oxidation to more negative potentials. The effect was more pronounced in acid than in alkaline media. Based on the established diagnostic criteria, the reaction between CO_{ad} and OH_{ad} species according to the Langmuir–Hinshelwood mechanism was proposed as the rate determining step in alkaline and acid media on Pt and PtRu catalysts.

Keywords: methanol oxidation, role of anions, temperature effect, reaction mechanism.

Electrochemical oxidation of methanol is the topic of fundamental research representing the prototype of the oxidation of small organic molecules as well as being applicable to research in the scope of direct methanol fuel cells. The reaction of methanol electro-oxidation on Pt involves several adsorption steps, including the formation of chemisorbed species leading to a decrease in the catalytic activity of the electrode surface. Scientific discussions were focused on the nature of the intermediates and the reaction products[1–8] and on the modification of the platinum surface in order to improve its catalytic activity and sensitivity regarding poisoning species.[9–12] CO_{ad} species were detected as the adsorbed intermediates acting as poisoning species at lower potentials or reactive intermediates in the presence of OH_{ad} species, which were also proposed as participants in the oxidation reaction.[2,11,13,14] OH_{ad} species originate from the discharge of OH^- anions in alkaline solution or from the dissociation of H_2O mole-

* Invited lecture at the Meeting of Electrochemical Section of the Serbian Chemical Society held on 23 December 2006. E-mail: jlovic@tmf.bg.ac.yu

Serbian Chemical Society member.

doi: 10.2298/JSC0707709L

cule in acid solution. Ru is mostly used as a promoter of Pt surfaces, in the form of Ru_{ad} on Pt or as PtRu alloys with different ratios of Ru to Pt. The effect of PtRu catalysts was described by the bifunctional mechanism,[9] when Ru promotes the oxidation of strongly bond CO_{ad} on Pt sites by supplying the oxygen source at lower potentials compared to pure Pt, or by the ligand effect,[12] when Ru changes the electronic properties of the surface and weakens the binding strength of CO_{ad}.

Methanol oxidation was investigated on Pt single crystals, polycrystalline Pt and supported platinum catalyst (Pt/C) and at two types of PtRu materials, *i.e.*, polycrystalline Pt modified with Ru adatoms in the process of electrochemical deposition (Pt/Ru) and a supported catalyst (PtRu/C). The reaction kinetics were investigated in alkaline and in acid media from the viewpoint of the influence of anion, pH and temperature. The reaction parameters were established and the rate determining step is suggested.

The quality of the electrode surfaces and the purity of the system were tested for Pt single crystal surfaces, polycrystalline Pt and a Pt/Ru electrode using cyclic voltammetry. In the case of the Pt/Ru electrode, this method enables the determination of the Ru surface coverage on polycrystalline Pt.[9] The nanocatalyst layer was also characterized by cyclic voltammetry in order to determine the reproducibility of the deposition and, in the case of the Pt/C catalyst, to define the real surface area and the particle diameter. The particle diameter was confirmed using physical methods (XRD and STM). The XRD measurements besides the average crystallite size, allow the phase composition to be determined, which for the Pt/C catalyst was one Pt phase and for PtRu/C two phases, *i.e.*, a solid solution of Ru in Pt and the hexagonal phase of Ru. The STM method was used for the determination of the topography of the electrodes. Analysis of STM images for the Pt/C and PtRu/C catalysts showed the almost spherical shape of the nanoparticles and their relatively uniform distribution on the carbon support. The obtained results are in accordance with TEM measurements.[15]

According to all the available results regarding methanol oxidation, the presence of OH_{ad} species at the electrode surface is necessary for this reaction. Linear extrapolation of the charging curve, which represents the dependence of the charge for the adsorption of oxygen containing species on potential, enables an estimation of the potential for the incipient formation of OH_{ad} species and the potential for oxide formation.[16] According to this method, which was applied for each Pt electrode, the adsorption of OH_{ad} species begins in the hydrogen region at the same potential in both the NaOH and $HClO_4$ solutions. In these solutions, oxide formation also commences at the same potential. These facts indicate that the ClO_4^- anions do not interfere with the adsorption of OH_{ad} species and oxide formation, while in H_2SO_4 solution the anions from the supporting electrolyte shift these processes to more positive potentials.

Based on the linear extrapolation method and on potentiodynamic measurements, a correlation between the beginning of the adsorption of OH_{ad} species and methanol oxidation was established for all the investigated Pt electrodes. The reaction commences at potentials close to the onset of OH adsorption, while the maximum of the methanol oxidation rate corresponds to the transition of oxygen species from the reversible to irreversible state. The activity of the investigated electrodes for the oxidation of methanol in alkaline solution was almost one order of magnitude larger than in acid solution. The significant effect of pH on the rate of methanol oxidation was explained by the pH dependent adsorption of OH_{ad} species.

The effect of anions on methanol oxidation was examined in $HClO_4$ and H_2SO_4 solutions. Although the sulfate anions from the H_2SO_4 supporting electrolyte suppress the rate of methanol oxidation, they do not influence the reaction path.

The investigation of methanol oxidation on single crystal platinum surfaces showed the structural dependence of the reaction. The difference in the activities of single crystal platinum electrodes can be explained by the different surface coverage with OH_{ad} species. The Pt/C catalyst is described by the Kinoshita model as cubooctahedral particles consisting of (111) and (110) oriented facets with low coordinated (110) edge and corner sites.[17] The obtained results showed that Pt/C catalyst closely obey the activities of (111) and (110) surfaces. In alkaline solution, the activity increase in the sequence (111) < (110) ≈ Pt/C < (332), while in acid solution the activity increase in the sequence (110) < Pt/C < (111).

Comparison of the activities of Pt and PtRu bimetallic electrodes shows a promoted methanol oxidation on the PtRu electrodes, since the Ru sites nucleate oxygen containing species at lower potentials, shifting the onset of the reaction to more negative potentials. The shift of the initial potential of the reaction between Pt and PtRu electrodes is larger in acid solutions. In alkaline solutions, Pt atoms adsorbed OH_{ad} species at as low potentials as does Ru, hence Ru atoms are not the only source of oxygen species. Consequently, the role of Ru as a donor of oxygen species in alkaline solutions is not as remarkable as in acid solutions. At higher potentials, the Ru sites influence the Pt atoms to form irreversible oxygen species, thus decreasing the activity of bimetallic electrodes.

The similarities in the structure of the Pt/Ru and PtRu/C catalysts results in the qualitatively same behavior of these catalysts regarding the initial potential of reaction and the Tafel slope.

Increasing the temperature shifted the onset of methanol oxidation to more negative potentials with the supported platinum and platinum ruthenium catalysts. The reaction rate was much higher at evaluated temperatures. According to the quasi–steady state measurements at three different temperatures in alkaline and acid solutions, the apparent activation energies for the methanol oxidation reaction were established for both supported catalysts.

On the basis of the determined diagnostics criteria, such as Tafel slope, transfer coefficient, reaction order with respect to methanol, OH^- ions in alkaline so-

lution and H^+ ions in acid solution, the reaction between CO_{ad} and OH_{ad} species according to the Langmuir–Hinshelwood mechanism was suggested as the rate determining step in the overall methanol oxidation reaction on supported Pt and PtRu catalysts.

И З В О Д

КИНЕТИКА И МЕХАНИЗАМ ОКСИДАЦИЈЕ МЕТАНОЛА НА Pt И PtRu КАТАЛИЗАТОРИМА У АЛКАЛНОЈ И КИСЕЛОЈ СРЕДИНИ

ЈЕЛЕНА ЛОВИЋ

ИХТМ–Центар за електрохемију, Његошева 12, 11001 Београд, Србија

Кинетика електрохемијске оксидације метанола је испитивана на низу катализатора од платине и платине−рутенијума. Показана је веза између почетка адсорпције OH_{ad} честица и почетка оксидације метанола. Утврђено је да се наноструктурни Pt катализатор по активности може поредити са монокристалима платине, што је у складу са усвојеним моделом по коме се активност Pt нанокатализатора може повезати са уделима нискоиндексних равни на површини наночестице. Показано је да оксидација метанола почиње на негативнијим потенцијалима на катализаторима који садрже рутенијум, при чему је тај ефекат израженији у киселој него у алкалној средини. Испитиван је утицај pH, анјона и температуре, одређени су кинетички параметри, а за спори ступањ у оксидацији метанола предложена је реакција честица CO_{ad} и OH_{ad} према Ленгмир–Хиншелвудовом механизму.

(Примљено 29. јануара 2007)

REFERENCES

1. B. Beden, J.-M. Leger, C. Lamy, in *Modern Aspect of Electrochemistry*, No. 22, Eds. J. O'M. Bockris, B. E. Conway, R. E. White, Plenum Press, New York, 1992
2. T. Iwasita, in *Handbook of Fuel Cells–Fundamentals, Technology and Applications*, Vol. 2, Eds. W. Viestich, H. A. Gasteiger, A. Lamm, Wiley, New York, 2003.
3. R. J. Nichols, A. Bewick, *Electrochim. Acta* **33** (1988) 1691
4. Y. X. Chen, A. Miki, S. Ye, H. Sakai, M. Osawa, *J. Am. Chem. Soc.* **125** (2003) 3680
5. T.O. Pavela, *Ann. Acad. Sci. Fenn. Ser. K* **A2** (1954) 1
6. W. Vielstich, *Fuel Cells*, Wiley Interscience, London, 1970
7. E. Morallon, A. Rodes, J. L. Vasquez, J. M. Perez, *J. Electroanal. Chem.* **391** (1995) 149
8. H. Wang, C. Wingender, H. Baltruschat, M. Lopez, M. T. Reetz, *J. Electroanal. Chem.* **509** (2001) 163
9. M. Watanabe, S. Motto, *Electrochim. Acta* **60** (1975) 267
10. H. A. Gasteiger, N. Marković, P. N. Ross, E. Cairns, *J. Electrochem. Soc.* **141** (1994) 1795.
11. N. M. Marković, P. N. Ross Jr., *Surface Science Reports* **45** (2002) 117
12. T. Frelink, W. Visscher, J. A. R. van Veen, *Surface.Sci.* **335** (1995) 353
13. A. V. Tripković, K. Đ. Popović, B. N. Grgur, B. Blizanac, P. N. Ross, N. M. Marković, *Electrochim. Acta* **47** (2002) 3707
14. A.V. Tripković, K.Đ. Popović, J.D. Lović, V.M. Jovanović, A. Kowal, *J. Electroanal. Chem.* **572** (2004) 119
15. V. Radmilović, H. A. Gasteiger, P. N. Ross, *J. Catal.* **154** (1995) 98
16. T. J. Schmidt, P. N. Ross, N. M. Marković, *J. Phys. Chem. B* **105** (2001) 12082
17. K. Kinoshita in: J. O´Bockris, B. E. Conway, R. E. White, Eds. *Modern Aspects of Electrochemistry* Vol. 14, Plenum Press, New York, 1982, p.557.

J. Serb. Chem. Soc. 72 (7) 713–722 (2007) UDC 666.266+678.686:66–977:53.083.98
JSCS–3605 *Original scientific paper*

The influence of high and low temperatures on the impact properties of glass–epoxy composites

SLAVIŠA PUTIĆ[1]*, MARINA STAMENOVIĆ[1], BRANISLAV BAJČETA[1], PREDRAG STAJČIĆ[1] and SRĐAN BOŠNJAK[2]

[1]*Faculty of Technology and Metallurgy, Belgrade, Republic of Serbia and* [2]*Faculty of Mechanical Engineering, Belgrade, Republic of Serbia*

(Received 5 December 2005, revised 29 November 2006)

Abstract: The aim of this paper is to present the influence of high and low temperatures on the impact properties glass–epoxy composites. The impact strength a_n is presented for four different glass–epoxy composite structures at three different temperatures, *i.e.*, at room temperature t = 20 °C, at an elevated temperature t = +50 °C and at a low temperature t = –50 °C. Standard mechanical testing was carried out on the composite materials with specific masses of reinforcement of 210 g m^{-2} and 550 g m^{-2} and orientations 0°/90° and ±45°. Micromechanical analysis of the failure was performed in order to determine real models and mechanisms of crack and temperature influence on the impact properties.

Keywords: glass woven–epoxy composite material, impact test, high and low temperature impact tests, micromechanical analysis

INTRODUCION

A very common way of fabrication of composite materials is using glass fibers for reinforcement and an epoxy resin as the matrix, which results in materials characterized by good physical, chemical, thermal, and mechanical properties. Some of the most important technical characteristics of these materials are their static and dynamic properties, which are due to the structure of the composite and the specific mechanism of crack formation. However, in reality, during exploittation, a lot of construction parts are subjected to high and low temperatures. In these cases, the toughness of the material changes, which can cause cracking under the stress, which is different from the one obtained in standard testing.

For the past few decades many researchers have studied the mechanical properties of the composite materials themselves, as well as the changes of the properties of the materials with changing temperature, which represent the basis of the research presented in this paper.

* Author for correspondence. E-mail: slavisa@tmf.bg.ac.yu
doi: 102298/JSC0707713P

Howard and Hollaway[1] studied the highly elastic properties of an epoxy resin and showed how they influence the properties of the composite material itself, as well as the changes of the properties of the materials with changing temperature.

Shindo, Ueda and Nishiok[2] in their joint work dealt with the thermal mechanical response of non-metalic woven composites with temperature-dependant properties. The composite material in generalized plane strain was assumed. First, a finite element method was used to study the influence of crack formation, residual thermal stresses and weave curvature on the mechanical performance of glass–epoxy laminates at low temperatures. Subsequently, they examined the stress state at the free edge of the woven composites. Finally, they calculated the mechanical properties of the woven composites. Numerical results on the distribution of the stresses and the mechanical properties at different temperatures and the warp angles were obtained and presented in graphical form.

Myung–Gon Kim *et al.*[3] researched the tensile properties of a glass/epoxy composite which had been cycled with thermo-mechanical loads at low temperatures using an environmental test chamber. Thermo-mechanical tensile cyclic loading (up to 10 cycles) was applied to laminates from room temperature (r. t.) to –50 °C, to –100 °C, and to –150 °C (c. t.). The results showed that the tensile stiffness significantly increased with decreasing temperature, while thermo-mechanical cycling had little influence on it. The tensile strength, however, decreased as the temperature was decreased down to c. t., while the rate of strength decrease was reduced after c. t. cycling. For the analysis of the test results, the coefficients of thermal expansion of the laminate composite specimen, both at r. t. and c. t., were measured, and the interface between fiber and matrix was observed using SEM images.

Abdel–Magid *et al.*[4] studied the properties of E–glass/epoxy composites at 65 °C. The values of the module of elasticity, stress and strain were examined. They were compared with the values obtained at room temperature; a decrease in value of the module of elasticity was noticed as well as of the break elongation. As a result, these authors concluded that longer exposure of the samples to higher temperatures caused ductile breaks on E–glass/epoxy composites.

In their work, Sefrani and Berthelot[5] presented an analysis of the temperature effect on both the stiffness and the damping of glass fibre composite materials. The experimental results showed that the mechanical properties were appreciably maintained up to the glass transition temperature, where the damping increased sharply in a small temperature interval.

Khalid[6] tested aramid/epoxy composite samples reinforced with glass fibers by the Sharpy impact method. The composite samples were made manually and had the dimensions 50 mm×10 mm×10 mm. The testing was performed in temperature interval + 40 to –40 °C with 10 °C steps. The volume fractions of fibers were 0.45, 0.55 and 0.65. The effects of the volume fraction of fiber and the tem-

perature on the impact toughness of the composite samples were tested. Damage of the tested samples was observed using a microscope at a magnification of 100. The results showed a slight increase of the impact toughness of the composite samples with increasing temperature in the interval –40 °C to –10 °C. This was followed by a larger increase of the value of the impact toughness with increasing temperature in interval –10 °C to 40 °C. It is shown that the aramid/epoxy has a higher impact toughness than glass/epoxy at all the tested temperatures. On the other hand, breaking of the fibers was found in the composite sample and the appearance of damage as a coma in the sample itself. Increasing the volume fraction of fiber decreased the impact toughness of the glass and aramid/epoxy.

Ray[7] suggested the need for investigating and characterizing the freeze-thaw response of polymer composites under different loading rates and also at ambient and sub-ambient temperatures. The presented experiments were performed with three weight fractions (*i.e.*, 0.55, 0.6 and 0.65) of glass fibers reinforced polyester composites. The specimens were suddenly exposed to a temperature of –80 °C for 2 h and then either immediately tested at that temperature or after allowing the samples to thaw to ambient temperature for 1 h.

According to the previous review, it is obvious that many scientists analyzed the properties of polymer composite materials at different temperatures. However, only a few of them tested their properties on impact loading and made conclusions about the change of their impact properties with changing temperature. That was one of the main reasons for the experiments reported in this paper.

In order to determine the properties of composites of different structures under extreme conditions, the impact tests were performed at +20 °C, +50 °C and –50 °C. By fractographic analysis of the crack surfaces, a complete picture was formed of the fabricated glass woven–epoxy composite materials, as well as of models and mechanisms of damage and crack initiation and propagation under load conditions.

EXPERIMENTAL

The composite materials were fabricated under laboratory conditions at the Faculty of Technology and Metallurgy in Belgrade, Serbia. The selected fiber reinforcement was woven roving E–glass (Tables I and II), produced by Tehnotex, Sombor, which is based on silicate glass containing up to 1 % alkali. The selected glass fibers have good mechanical, hydro-thermal and dielectrical properties. Two specific weights of glass woven reinforcement were used (C = 210 g m^{-2}, D = 550 g m^{-2}) and two orientations (0º/90º and ±45º). The glass woven was made by classical procedures of spinning on different kinds of looms (Fig. 1).

The matrix material was a polycondensation product of 2,2-bis-(4-hydroxyphenyl) propane (bisphenol A) and epichlorhydrin (Epidijan 6 made by Zaktady Chemiczne “Organika–Sarzyna” S.A) with the structure shown in Sheme 1.

3-Aminomethanol-3,5,5-trimethanolcyclohexylamine, a modified cycloaliphate amine of the same producer, was used for fixing. The properties of the employed resin were taken from the producer’s catalog and are presented in Table III.

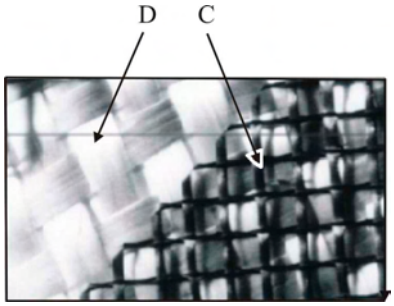

Fig. 1. A view of used types of woven glass.

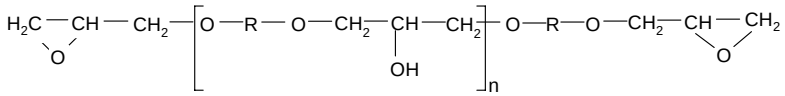

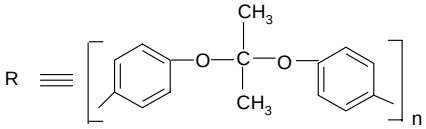

Scheme 1. Polycondensation product of 2,2-bis-(4-hydroxyphenyl) propane (bisphenol A) and epichlorhydrin.

TABLE I. Structural components of E–glass

Structural component	Content / %
Silicium(IV)-oxide	52 – 56
Aluminium(III)-oxide	12 – 16
Boron(III)-oxide	5 – 10
Sodium(I)-oxide, Potasium(I)-oxide	0 – 2
Magnezium(II)-oxide	0 – 5
Calcium(II)-oxide	16 – 25
Titanium(IV)-oxide	0 – 1.5
Iron(III)-oxide	0 – 0.8
Iron	0 – 1

The epoxy–amine mixtures were prepared by heating the resin in an oil bath to 70 °C, adding the curing agent and continuously stirring until a clear homogeneous solution was obtained. Each laminate was fabricated by hand in a wet lay-up. Alternate layers of fiber reinforcement plies and liquid resin were placed inside a dam on a flat mould plate. The mould plate[8,9,10] consisting of an upper and bottom metal board of dimensions 292 mm×230 mm×13 mm was tightened with four screws to obtain the necessary pressure force of 67 N. The materials were cured for 48 h at room temperature, followed by 5 h at 90 °C and a final slow cooling. The structures of the fabricated composites are given in Table IV.

The impact test was performed on an impact test machine with a pendulum for Sharpy experiments in accordance with ASTM[11] on cut specimens (the cutting was in two directions, with orie-

ntation 0°/90° and ±45°) of fabricated composite materials. All combinations of the specimens with dimensions (55 mm×10 mm×2 mm) are given in Table IV. The specimens were machined from flat panels using a high speed diamond saw with liquid cooling. This machining operation resulted in very smooth, square cuts. One edge of each specimen was polished so that cracks and delamination could be readily discerned.

TABLE II. Physical properties of E–glass fiber

Specific weight	2.6 N m^{-3}
Tension strength	2400 MPa
Modulus of elasticity	73 GPa
Extension	3.3 %
Thermal extension	5×10^{-6} K^{-1}
Thermal installing	1 W mK^{-1}
Dielectrical constant	6.7
Specific electrical resistance	10^{14} Ω cm
Absorbing moisture, at 20 °C → 65 %	0.1

TABLE III. Catalog properties of epoxy resin

Properties	Specification	Analysis results
Appearance	Viscous yellow liquid	Viscous yellow liquid
Epoxy number/ val/100 g	0.51– 0.54	0.520
Epoxy equivalent	196– 185	192
Density/ g cm^{-3}	–	1.26
Viscosity at 25 ºC/ Pa s	10–15	13700
Color according to *Gardner*	3	less than 3
Contents of unelaborated components/ % min	99	99.5
Contents of organic chlorine/ % max	0.3	0.17

TABLE IV. The structure of fabricated composite materials

Sample	Number of reinforcement layers	Specific mass of reinforcement/ g m^2	Orientation of reinforcement	Mass fraction of reinforcement/ %
I–C–1	5	210	0°/90°	34.2
I–D–1	4	550		56.7
I–C–2	5	210	±45°	35.4
I–D–2	4	550		58.4

Five test specimens for each of the studied materials and test temperatures were used for the experiments. The heating and cooling of the test specimens for study at the high and low temperature was conducted in small closed chambers for the temperature regulation and subsequently they were set on the test machine. The temperature was measured with a digital thermometer and at the moment when the expected temperature was reached, the test specimens were set in the testing device and tested.

Scanning with an electronic microscope (SEM–Jeol JSM 5300) was performed on the fracture surfaces of mechanically failed specimens to study the mechanism of crack formation. The fracture surfaces were vapor coated with a thin layer of gold to enhance the image.

RESULTS AND DISCUSSION

Impact test at t=*20 °C*

The values of impact energy were directly read on the scale of the testing device. According to it and the dimensions of the test specimens, the impact strength was calculated from Eq. (1):

$$a_n = \frac{A_n}{bh} \tag{1}$$

where: a_n, J m^2, is the impact strength of the test specimen; A_n, J, is the impact energy that the specimen absorbs; b, m, is the width of specimen and h, m, is the thickness of specimen.

The average values (five tested specimens) of the impact strength are given in Fig. 2.

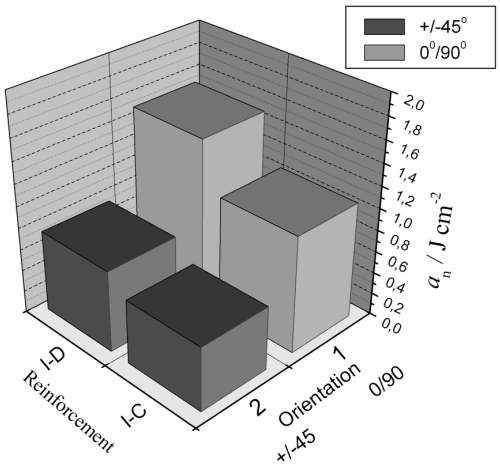

Fig. 2. Impact strength, average values at 20 °C.

Based on the experimental results presented in Fig. 2, it can be concluded that the impact properties increased for both types of orientation of the reinforcement with increasing specific mass of the glass woven reinforcement in the sample, although the results were better in case of orientation 0°/90° (samples C–1 and D–1) than in case of orientation ±45° (samples C–2 and D–2). In both cases (0°/90° and ±45°), a greater impact strength was observed for the samples with reinforcement of the type D, which confirms the assumption that a greater specific mass fraction of reinforcement imparts a better impact strength on composite materials.[8,9,10] Also, a second explanation of these results is the type of reinforcement cloth. The employed reinforcement cloth D (Fig. 1) has small spaces between the plaits of weaving. This means that spaces without resin (in other words with air bubbles) do not exist. In the other case, when the reinforcement was type C (with large spaces between the plaits of weaving, Fig. 1) the situation was different. In this case, the area between the plaits of weaving contained a lot

of air bubbles, which caused the decrease of impact strength. This conclusion will be proved in the micromechanical analysis in this paper.

*The impact test at elevated (*t = *+50 °C) and low (*t = *–50 °C) temperatures*

In order to determine the influence of temperature on the value of the impact strength, studies were performed at +50 °C and –50 °C. The procedure of the study, the calculation (Eq. (1)) and the employed device were the same as for the procedure of the study at room temperature. For a better comparison of the results, Fig. 3 shows the average calculated values of the impact strength at the three test temperatures. Comparison of test results was conducted in relation to results of the study at room temperature.

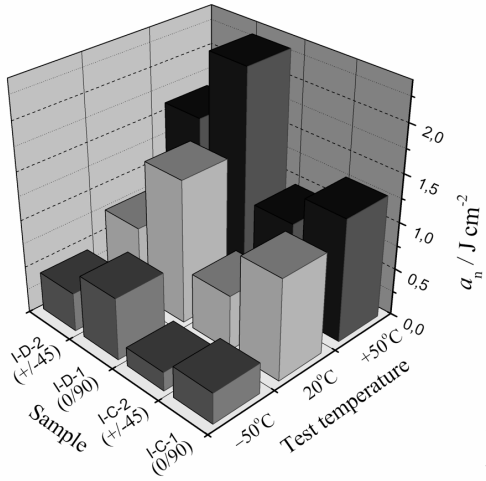

Fig. 3. Impact strength, average values for all test temperatures.

Micromechanical analysis of failure

An impact load crack was initiated in all the test specimens on the side of the outer layer which was subjected to tension (Fig. 4). The break occurred at the moment a critical state of stress in the material was reached, which caused the occurrence of a critical value of crack and its progressive growth. The location of the critical crack is related to fiber–matrix debonding (Fig. 5), after which the fibers cracked. It is obvious that on the spot where the first break appeared (outer layer) more broken fibers existed which had previously been debonded and pulled out from the matrix. Crack propagation leads through to the inner surface of test specimen in the transversal direction of the test specimen. Lateral on this crack, cracks and delamination in test specimens appeared (Fig. 6) as a result of shear stresses in the layers. The existence of shear stresses is characteristic for the impact test, especially in the case when the orientation of the glass woven reinforcement was ±45°. The inner layers which were loaded on impact were exposed to great axial stresses. The final crack was in the vertical plane of the test specimen.

It is very interesting that the broken test specimens tested at a temperature of –50 °C had a completely different appearance to those tested at +50 °C. This is totally understandable bearing in mind the two specific types of deformations characteristic for a polymer matrix subjected to different test temperatures: viscous flow and elastic deformation. These two types of deformations in the material directly influence the final properties of a polymer composite material. After the experiment, the specimens tested at the higher temperature showed characteristics of ductile fracture (Fig. 7), whereas those tested at the lower temperature had a brittle crack (Fig. 8).

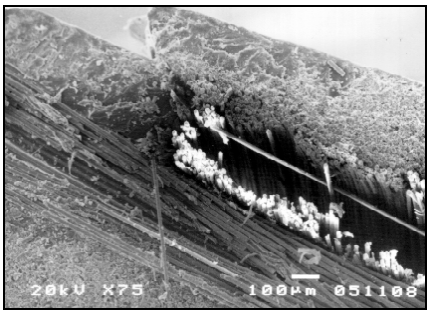

Fig. 4. SEM Micrograph of the cracking of outer layer of specimen subjected to impact load on enlargement ×75; test sample I–D–1.

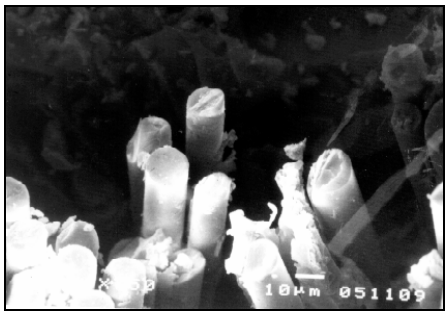

Fig. 5. SEM Micrograph of the fiber–matrix debonding on enlargement ×350; test sample I–D–1.

Fig. 6. Delaminations between layers in test sample I–C–2.

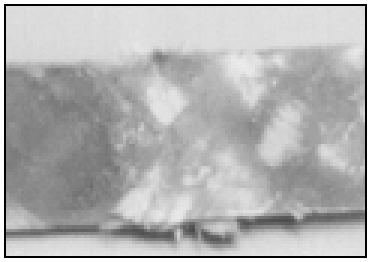

Fig. 7. A view of impact cracked test specimen at t = +50 °C (the appearance of ductile fracture); test sample I–D–2.

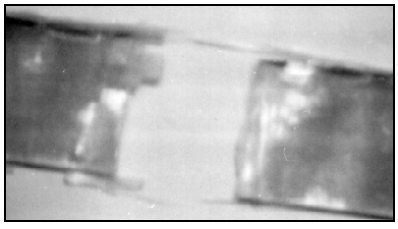

Fig. 8. A view of impact cracked test specimen at t = –50 °C (the appearance of brittle crack); test sample I–D–1.

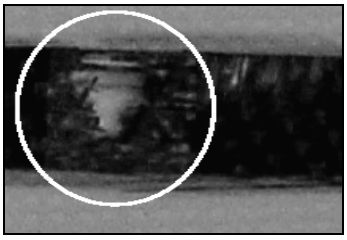

Fig. 9. Delamination and failure fracture surface on elevated temperature.

Cracks such as that shown in Fig. 9 verify that at the elevated temperature delamination of the specimens occurred to a greater extent than at room temperature. The edge replicas also indicate a greater amount of fiber/matrix debonding in the specimens tested at the elevated temperature, but the edge replicas should be considered with caution since they show only a small section of the specimens.

CONCLUSIONS

In this study the impact strength of glass woven–epoxy composite materials at 20, –50 and +50 °C were determined. The test materials were glass woven/epoxy composite materials with two different specific masses of glass woven reinforcement and two different orientations.

It was shown that materials with reinforcement of higher specific mass (type D of woven glass → ρ = 550 g m^{-2}) exhibited better impact properties. The impact strength obtained at the elevated temperature was greater than that at room temperature. On the other hands, the test results showed minimal values of impact strength at the low temperature, with characteristics brittle cracks.

In order to obtain a better picture of the quality of the fabricated composite materials, micromechanical analysis was performed. The SEM micrographs of the fracture surfaces confirmed the models and the mechanisms of impact crack known in the literature for similar structures and materials, such as fiber crack, matrix crack, fiber debonding and delamination.

И З В О Д

УТИЦАЈ ВИСОКИХ И НИСКИХ ТЕМПЕРАТУРА НА УДАРНА СВОЈСТВА СТАКЛЕНО−ЕПОКСИДНИХ КОМПОЗИТА

СЛАВИША ПУТИЋ[1], МАРИНА СТАМЕНОВИЋ[1], БРАНИСЛАВ БАЈЧЕТА[1], ПРЕДРАГ СТАЈЧИЋ[1] и СРЂАН БОШЊАК[2]

[1]Технолошко-металуршки факултет, Београд и [2]Машински факултет, Београд, Србија

Циљ овог рада је да прикаже утицај високих и ниских температура на ударна својства стаклено-епоксидних композита. Ударна јачина a_n приказана је за четири различите структуре стаклено−епоксидних композита на три различите температуре, тј. на собној t = 20 °C, повишеној t = +50 °C и ниској температури t = –50 °C. Стандардно механичко тестирање обављено је за композите са масама ојачања 210 g m^{-2} и 550 g m^{-2} и орјентације 0°/90° и ±45°. Микромеханичка анализа оштећења изведена је са циљем да се одреде реални модели и механизми лома и утицаја температуре на ударна својства.

(Примљено 5. децембра 2005, ревидирано 29. новембра 2006)

REFERENCES

1. M. Howard, L. Hollaway, *Composites* **18** (1987) 317
2. Y. Shindo, S. Ueda, Y. Nishioka, *Fusion Engin. Design* **20** (1993) 469
3. M.–G. Kim, S.–G. Kang, C.–G. Kim, C.–W. Kong, *Composite Structures*, in Press.
4. B. Abdel–Magid, S. Ziaee, K. Gass, M. Schneider, *Composite Structures* **71** (2005) 326
5. Y. Sefrani, J.–M. Berthelot, *Composites Part B: Engineering* **37** (2006) 346

6. A. Khalid, *Materials & Design* **27** (2006) 499
7. A.C. Ray, *J. Reinforced Plastics Composites* **24** (2005) 713
8. M. Krivokuća (Stamenović), M.Sc. Thesis, Faculty of Technology and Metallurgy, University of Belgrade, Belgrade 1999 (in Serbian)
9. M. Hadud, M.Sc. Thesis, Faculty of Technology and Metallurgy, University of Belgrade, Belgrade, 2003
10. M. Krivokuća (Stamenović), S. Putić, P. Uskoković, Č. Lačnjevac, R. Aleksić, *TEHNIKA–Novi materijali* **7** (1998) 9 (in Serbian)
11. ASTM D256–06, "Standard Test Methods for Determining the Izod Pendulum Impact Resistance of Plastics", Annual Book of ASTM Standards, Vol. 15.03, American Society for Testing and Materials, Philadelphia, PA, USA, 1999.

J. Serb. Chem. Soc. 72 (7) 723–735 (2007) UDC 66.094.3+678.664+621.78.063+544.478
JSCS–3606 *Original scientific paper*

Thermo-oxidative stability of waterborne polyurethanes with catalysts of different selectivity evaluated by non-isothermal thermogravimetry

SUZANA M. CAKIĆ*, GORAN S. NIKOLIĆ# and JAKOV V. STAMENKOVIĆ

Faculty of Technology, Bulevar oslobođenja 124, 16000 Leskovac, Serbia

(Received 11 January 2006, revised 12 March 2007)

Abstract: Thermogravimetry was used for the evaluation of the thermo-oxidative stability of waterborne polyurethanes (wbPUR) containing catalysts of different selectivity. From Arrhenius plots, activation energies of between 50 and 120 kJ mol^{-1} for wbPUR were determined, depending on the temperature interval, selectivity of the catalyst and degree of degradation. Waterborne polyurethanes without catalyst showed lower thermal stability than waterborne polyurethanes with catalysts of different selectivity. Non-isothermal thermogravimetry indicated the presence of different degradation processes and enabled the kinetics parameters at higher degrees of degradation to be evaluated.

Keywords: waterborne polyurethanes, thermo-oxidation, thermogravimetry, thermal stability, activation energy.

INTRODUCTION

Two-pack paint systems are used in various segments of the industrial coatings market. The performance of these systems is, in general, surprisingly good. Gloss, appearance, chemical resistance and mechanical properties are on the level of solvent-borne products. However, the application window of these water-borne, two-pack polyurethanes is rather small and this impedes the breakthrough of this technology in some segments of the industrial coatings market. It is, for example, difficult to obtain a high layer thickness without surface defects with these two-pack systems.[1]

The main aspect in the development of waterborne polyurethanes is at first to find methods for preventing undesired secondary reactions with water and achieving the best crosslinking. One novel approach to control the water side reaction is the use of catalysts which selectively catalyze the isocyanate–polyol reaction and not the isocyanate–water reaction (Scheme 1). This reaction is reduced to a minimum by use of non-tin catalysts.[2]

* Corresponding author. E-mail: suzana@yahoo.com
# Serbian Chemical Society member.
doi: 10.2298/JSC0707723C

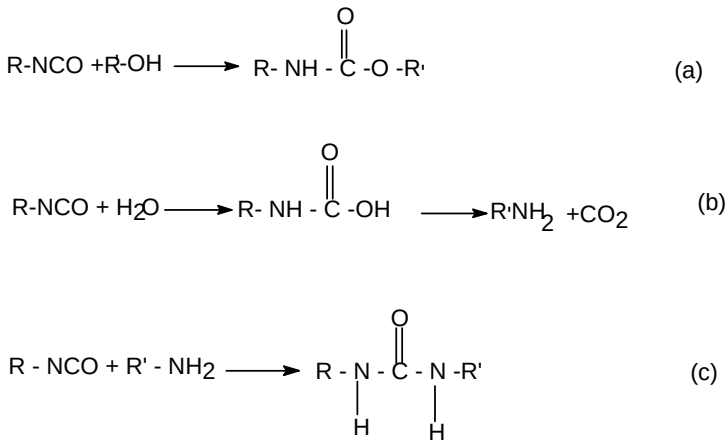

Scheme 1. Isocyanate reactions with alcohol (a) and with H_2O (b,c).

The reactions of isocyanate, especially aliphatic isocyanate, with hydroxyl or water are relatively slow at ambient temperature in the absence of a catalyst. Organo–metallic compounds or tertiary amines are normally required to catalyze the crosslinking of isocyanate with hydroxyl groups for ambient cure applications.[2,3]

Blank[3] examined the selectivity of various compounds to model compounds. Butyl isocyanate and 2-ethyl-1-hexanol were selected as model compounds because of their similarities with aliphatic polyisocyanates and hydroxyl resins, as well as because of the simplicity of their FTIR spectra. The relative selectivity (S), which can be obtained from Eq. (1), was measured as the urethane IR peak area (P_{urethane})/urea IR peak area (P_{urea}) ratio:

$$S = P_{\text{urethane}}/P_{\text{urea}} \quad (1)$$

After integration of the characteristic absorption maxima of urethane and urea, the relative selectivity was calculated.

Complexes of Mn(III)-diacetylacetonatomaleate with various ligands based on acetylacetonate and maleic acid showed high selectivity for the isocyanate–hydroxyl reaction.[4,5]

Several thermogravimetry methods have been used to study the thermal stability of polymeric materials both under oxidative and non-oxidative conditions. Kinetics parameters can be derived from isothermal and dynamic data, as reported by various researchers.[6–12]

The prediction of the lifetime service of polymeric materials under accelerated degradation conditions using thermogravimetry (TG) was reviewed by Flynn.[13] From the kinetics of degradation, the activation energy can be calculated from an Arrhenius correlation,[8,10,11,13,14] and this parameter can be useful for predicting the stability of a material. Also, the 5 % weight loss is a reasonable criterion for defining the lifetime of a material at service temperatures. Similarly, the acti-

vation energy can also be evaluated from dynamic experiments at different heating rates, whereby various percents of degradation can be considered. In the case of polyurethane materials, only the initial weight loss (up to 10 and, in some cases, 40 %) can be used to calculate the apparent activation energies[11,20] because the reaction becomes too complex at higher percents of degradation to evaluate the kinetics parameters and the interpretation is not easy. In fact, the mechanism of polyurethane degradation is very complicated, involving the disruption of the urethane bond at about 210 °C with the formation of isocyanate and alcohol groups,[14] as was confirmed by spectroscopic analysis. The thermal degradation of polyurethane materials has been examined by several researchers.[15,17] In particular, the composition of polyurethane, *i.e.*, the type of isocyanate/polyol and the chain extender or crosslinker, was found to directly influence the thermal stability[11,12,18,19] and, in some cases, degradation curves have been proposed as "fingerprints" to identify commercial polyurethanes.[20]

The objective of the present study was to evaluate the resistance to thermo-oxidation of different classes of waterborne polyurethanes (wbPUR) by thermogravimetry, using catalysts of different selectivity.

Kinetic Analysis

The thermoxidation experiments are generally described by the percentage of weight loss, $W_{\%}$, and the degree of degradation, α, defined as

$$W_{\%} = 100(w_0 - w)/w_0 \quad (2a)$$

$$\alpha = (w_0 - w)/w_0 \quad (2b)$$

where w_0 and w are the initial and the actual weight of the sample, respectively.

In the dynamic method,[14] several heating rates, β, are used which are related to the temperature at which a definite percent of weight loss occurs, according to

$$\log \beta = \log A_{DYN} - E_{act-DYN}/2.303RT_{\alpha} \quad (3)$$

where A_{DYN} is the pre-exponential factor, $E_{act-DYN}$ the activation energy and T_{α} the absolute temperature at which the degree of degradation α is attained. The value of A_{DYN} formally represents the heating rate β at which a certain percent of weight loss occurs at infinite temperature; the lower its value, the higher the stability of the material. The kinetics of the thermo-oxidation process depends on both activation energy and the pre-exponential factor.

EXPERIMENTAL

The polyols and polyisocyanates employed in this study were commercial materials which were used without further purification. The two polyol components with a hydroxyl number above 130 used in this study were: an acrylic dispersion in a water–butanol mixture, (Macrynal VSM 2521 w/42 WAB, Solutia Austria GmbH) and an acrylic resin as a water dispersion (Macrynal VSM 6299 w/42 WA, Solutia Austria GmbH). The content of dry matter in both these dispersions was 42 %.

As suitable hardeners for these dispersions, aliphatic polyfunctional isocyanates based on hexamethylene diisocyanates were employed, *i.e.*, Bayhydur VP LS 2319 (18.2 % NCO), Bayhydur VP

LS 2336 (16.2 % NCO), Bayhydur VP LS 2150 (13.4 % NCO) and Desmodur 3600 (23 % NCO), purchased from Bayer AG Germany. All the applied hardeners were without an organic solvent (100 %), except Bayhydur VP LS 2150 (70 %).

The Zirconium catalyst (ZrCAT) was a proprietary zirconium tetra-dionato complex 21 in a reactive diluent with a metal content of 0.4 %.

The manganese catalyst, the complex Mn(III)-diacetylacetonatomaleate, has shown unusually high selectivity for the isocyanate–polyol reaction in comparison with commercially available zirconium catalyst 4.5. The manganese catalyst (MnCAT) was in a reactive diluent with a metal content of 0.4 %.

Catalyst concentrations of 2 % and 4 %, relating to the coating hardener, were added to component B.

The Tables I and II show the composition of the employed components.

TABLE I. Composition of the two-component waterborne polyurethane (wbPUR1) based on the polyol Macrynal VSM 6299 w/42 WA (coating hardness 32.5 %)

Component A / weight %	Control	ZrCAT	MnCAT
Polyol VSM 6299	44.1	44.1	44.1
Water	41.2	41.2	41.2
Component B / wt. %			
Bayhydur VP LS 2319	5.88	5.88	5.88
Dezmodur N 3600	5.88	5.88	5.88
Methoxypropyl acetate	2.94	2.94	2.94
Zr Catalyst, 2 % (4%) on resin solids	No catalyst	0.65 (1.30)	–
Mn Catalyst, 2 % (4%) on resin solids	No catalyst	–	0.65 (1.30)
Total	100.00	100.6	100.6

TABLE II. Composition of the two-component waterborne polyurethane (wbPUR2) based on the polyol Macrynal VSM 2521 w/42 WAB (coating hardness 40.2 %)

Component A / weight %	Control	ZrCAT	MnCAT
Polyol VSM 2521	56.2	56.2	56.2
Water	22.6	22.6	22.6
Component B / weight %			
Bayhydur VP LS 2336	9.8	9.8	9.8
Bayhydur VP LS 2150 BA	9.8	9.8	9.8
Methoxypropyl acetate	1.1	1.1	1.1
Zr Catalyst, 2 % (4%) on resin solids	No catalyst	0.8 (1.60)	–
Mn Catalyst, 2 % (4%) on resin solids	No catalyst	–	0.8 (1.60)
Total	99.5	100.3	100.3

The waterborne polyurethanes were finally stored at room temperature and used without any drying treatment. The films were, however, dried for 4 – 8 h.

The thermograms were recorded on a Perkin–Elmer DSC 4 instrument. The samples were prepared using aluminum pans with cover gap for the passage of gas. The sample weight was 360 mg. In the case of the dynamic method, heating rates of 0.5, 1, 2, 5, and 10 °C min^{-1} were employed in the range of 30 – 500 °C, and degradations up to 0.025, 0.05, and 0.10 were investigated. The instrument had an autocalibration and linear regulation of the chosen temperature gradient.

RESULTS AND DISCUSSION

Tables III and IV summarize the experimental data of the thermo-oxidation of the different waterborne polyurethanes measured by dynamic methods.

TABLE III. Temperatures at which degradations of 0.025, 0.05 and 0.10 occurred during dynamic heating at different heating rates

β Heating Rate °C min^{-1}	α Degradation	wbPUR1–Control °C	wbPUR1–ZrCAT 2 %, °C	wbPUR1–MnCAT 2 %, °C	wbPUR1–ZrCAT 4 %, °C	wbPUR1–MnCAT 4 %, °C
0.5	0.025	127	139	153	150	164
	0.05	163	173	188	185	200
	0.10	181	190	205	202	217
1	0.025	131	144	157	155	168
	0.05	175	186	199	198	211
	0.10	181	192	205	204	217
2	0.025	143	154	169	166	180
	0.05	178	188	203	199	214
	0.10	192	201	216	213	228
5	0.025	174	184	199	195	210
	0.05	221	228	245	240	257
	0.10	248	254	271	266	283
10	0.025	181	191	205	202	217
	0.05	265	271	287	283	300
	0.10	277	282	299	294	312

TABLE IV. Temperatures at which degradations of 0.025, 0.05 and 0.10 occurred during dynamic heating at different heating rates

β Heating Rate °C min^{-1}	α Degradation	wbPUR1–Control °C	wbPUR2–ZrCAT 2 %, °C	wbPUR2–MnCAT 2 %, °C	wbPUR2–ZrCAT 4 %, °C	wbPUR2–MnCAT 4 %, °C
0.5	0.025	141	153	176	164	178
	0.05	178	188	203	199	214
	0.10	190	199	214	211	226
1	0.025	150	161	179	173	190
	0.05	181	190	210	202	222
	0.10	203	211	232	223	244
2	0.025	165	176	190	187	201
	0.05	215	223	239	235	251
	0.10	220	228	244	240	256

TABLE IV. Continued

β Heating Rate °C min^{-1}	α Degradation	wbPUR1–Control °C	wbPUR2–ZrCAT 2 %, °C	wbPUR2–MnCAT 2 %, °C	wbPUR2–ZrCAT 4 %, °C	wbPUR2–MnCAT 4 %, °C
5	0.025	169	180	193	191	204
	0.05	224	232	246	244	258
	0.10	251	258	272	270	285
10	0.025	192	199	215	211	227
	0.05	273	276	294	288	307
	0.10	290	292	311	304	323

From the dynamic degradation, the lower thermal stability the two-pack the waterborne polyurethanes without catalyst is immediately evident as a fixed degree of degradation is attained at a considerable lower temperature than waterborne polyurethanes with a catalyst.

During dynamic thermo-oxidation, it was also possible to detect the presence of different stages of degradation as illustrated in Figs. 1 and 2, which show the TG curves of wbPUR1and wbPUR2, respectively. The change in the slope in the interval 100 – 300 °C is due to a change in mechanism and confirms the different activation energy measured at degrees of degradation of 0.025, 0.05, and 0.10. Below 100 °C, a weight loss of about 1 % was observed resulting from the evaporation of equilibrium moisture or other volatile products.

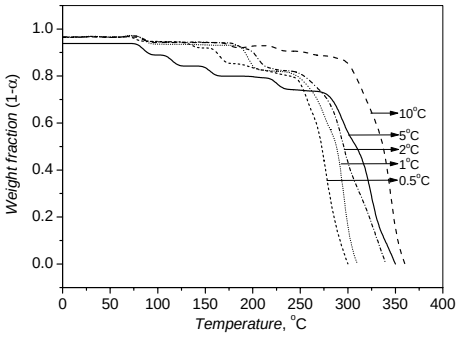

Fig. 1. Weight fraction (1–α) of wbPUR1 with MnCAT (2 %) *versus* temperature during dynamic thermo-oxidation at different heating rates.

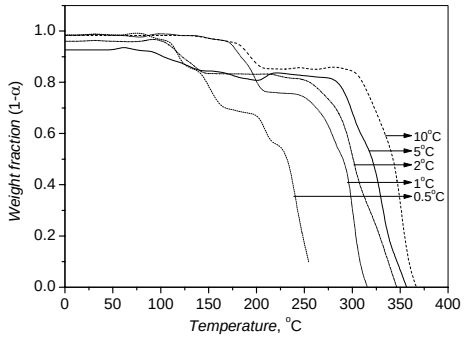

Fig. 2. Weight fraction (1–α) of wbPUR2 with MnCAT (2 %) *versus* temperature during dynamic thermo-oxidation at different heating rates.

From the derivative curve of the degree of degradation, dα/dT, a single degradation process can readily distinguished, as shown in Figs. 3 and 4 in the case of samples heated at 10 °C min^{-1}. This curve represents the rate of degradation of the material under the particular experimental conditions. The main data are summarized in Tables V and VI.

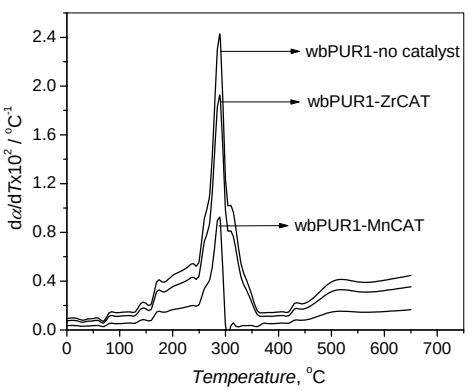

Fig. 3. Rate of mass loss of wbPUR1 with different catalysts *versus* temperature, obtained at a heating rate of 10 °C min^{-1}.

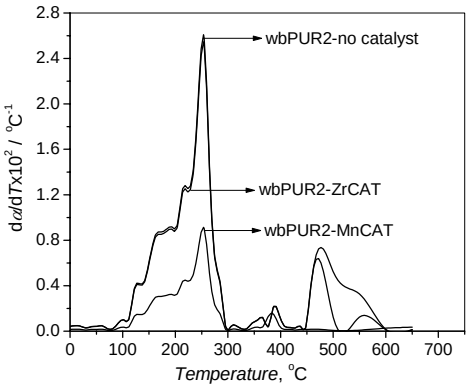

Fig. 4. Rate of mass loss of wbPUR2 with different catalysts *versus* temperature, obtained at a heating rate of 10 °C min^{-1}.

TABLE V. Data evaluated from the DTG curves of wbPUR1 obtained at a heating rate of 10 °C min^{-1}

		Low-temperature peak		Main Peak		High-temperature peak	
	t_{onset}/°C	t/°C	$\frac{d\alpha}{dt}\times100$/°C^{-1}	t/°C	$\frac{d\alpha}{dt}\times100$/°C^{-1}	t/°C	$\frac{d\alpha}{dt}\times100$/°C^{-1}
wbPUR1–Control	140.0	171.6	0.40	287.6	2.43	430.9	0.22
wbPUR1–MnCAT	144.2	172.7	0.14	288.6	0.92	433.3	0.08
wbPUR1–ZrCAT	144.4	171.6	0.33	288.6	1.92	432.3	0.17

TABLE VI. Data evaluated from the DTG curves of wbPUR2 obtained at a heating rate of 10 °C min^{-1}

		Low-temperature peak		Main peak		High-temperature peak	
	t_{onset}/°C	t/°C	$\frac{d\alpha}{dt}\times100$/°C^{-1}	t/°C	$\frac{d\alpha}{dt}\times100$/°C^{-1}	t/°C	$\frac{d\alpha}{dt}\times100$/°C^{-1}
wbPUR2–Control	150.1	201.0	0.91	253.2	2.60	389.5	0.22
wbPUR2–MnCAT	160.5	198.6	0.31	253.2	0.90	383.5	0.14
wbPUR2–ZrCAT	150.5	198.6	0.88	253.2	2.54	389.5	0.21

The onset temperature, evaluated from the initial part of the derivative curve, revealed that wbPUR1 without catalyst and those with catalysts which also started to degrade at a similar temperature (140 °C) were less stable with respect to wbPUR1 with the selective catalyst (144 °C). In particular, waterborne PUR1 without catalyst and with catalysts showed the same position of the main peak at

288 °C. According to the maximum of the peak, the waterborne polyurethane (wbPUR1) with the MnCAT (4 %) catalyst had the lowest rate of decomposition $d\alpha/dT$, (0.92×102 °C^{-1}), whereas waterborne polyurethane (wbPUR1) with ZrCAT (4 %) catalyst exhibited the highest degradation rate (1.92×102 °C^{-1}), and the waterborne polyurethane (wbPUR1) without catalyst exhibited a value of about 2.43×102 °C^{-1}. The sample wbPUR2 showed the same decreasing trend of degradation rate with the MnCAT (Fig. 4).

The presence of more than one peak in the $d\alpha/dt$ curve attests to the various steps of degradation. For example, in the case of the oxidative degradation of a waterborne polyurethane with similar polyester–polyol components, the dynamic method proposed by Fambri *et al.*[14] gave three peaks.

In this case, the secondary peak at low temperatures, exhibited in the range of 170 °C for the waterborne PUR1 only, is attributable to the degradation of lateral groups. On the other hand, the main peak is related to the thermo-oxidation of the main polymer backbone, whereas the secondary peak at high temperature corresponds to the degradation of the final 20 % of the residual material (degree of degradation from 0.8 to 1). Using dynamic methods, the degradation kinetics can be studied at very high percent of weight losses, very close to complete thermo-oxidation. However, these latter data are quite time consuming and the kinetic data could be the result of the superposition of various reaction stages. The heating rate showed its upper limit of application at about 10 °C min^{-1}, depending on the stability of the material.

The procedure for the evaluation of the kinetics from the experimental data from dynamic experiments is exemplified in Figs. 1 and 2 for the waterborne polyurethanes wbPUR1 and wbPUR2, respectively. From this analysis, the temperatures were achieved at degradations of 0.025, 0.05, and 0.10. The correspondent Arrhenius plots were determined from Eq. (3) and are given in Figs. 5a and b, respectively.

Activation energy

The activation energies and their standard deviations were calculated from the slope of the best-fitting linear regression according to Eq. (3). Values in the range of 53 – 120 kJ mol^{-1} were found for both samples, as a function of the material, the degree and of the degradation.

In particular, in the initial stage of thermo-oxidation, the activation energy ranged between 53 and 86 kJ mol^{-1} for wbPUR1 and between 64 and 120 kJ mol^{-1} for wbPUR2, as shown in Figs. 6a and b. Both samples showed the tendency of increased activation energy for all degree of degradation on addition of the more selective catalyst. Then the values of the activation energy of 53 – 62 kJ mol^{-1} and 64 – 78 kJ mol^{-1} for wbPUR1 and wbPUR2, respectively, at $\alpha = 0.10$ were found.

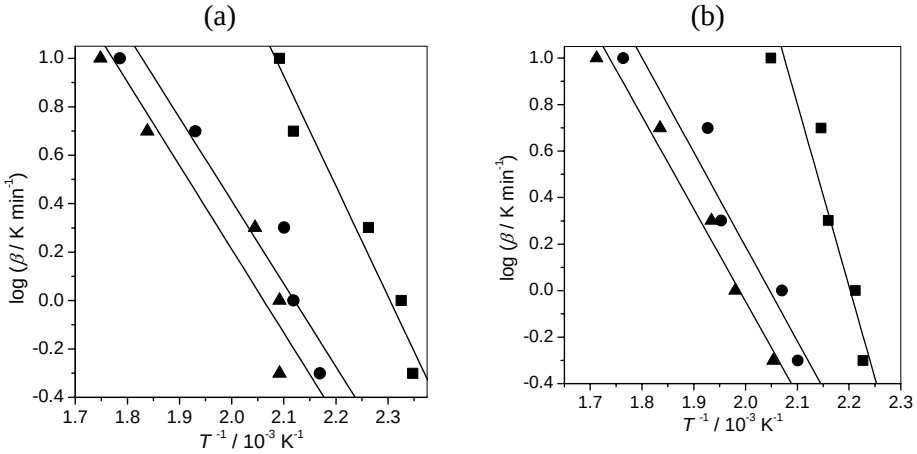

Fig. 5. (a) Arrhenius plot of wbPUR1 with catalyst MnCAT (2 %) derived from dynamic curves at 0.025 (■), 0.05 (●), and 0.10 (▲) of degradation according to Eq. (3). (b) Arrhenius plot of wbPUR2 with catalyst MnCAT (2 %) derived from dynamic curves at 0.025 (■), 0.05 (●), and 0.10 (▲) of degradation according to Eq. (3).

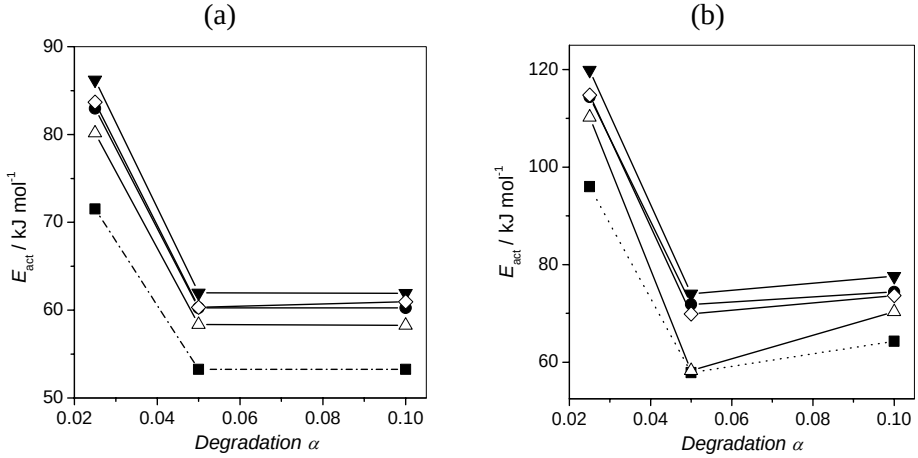

Fig. 6. (a) Activation energies evaluated at various percents of degradation of wbPUR1, without catalyst (■), wbPUR1 with catalyst ZrCAT (2 %) (△), wbPUR1 with catalyst ZrCAT (4 %) (◇), wbPUR1 with catalyst MnCAT (2 %) (●), wbPUR1 with catalyst MnCAT (4 %) (▼). (b) Activation energies evaluated at various percents of degradation of wbPUR2, without catalyst (■), wbPUR2 with catalyst ZrCAT (2 %) (△), wbPUR2 with catalyst ZrCAT (4 %) (◇), wbPUR2 with catalyst MnCAT (2 %) (●), wbPUR2 with catalyst MnCAT (4 %) (▼).

Pre-exponential factors

The pre-exponential factors could provide information on intrinsic thermal stability because they formally describe the behavior at infinite temperature. The

higher is the tendency to thermal oxidize at infinite temperature, the higher is the dynamic pre-exponential factor. As indicated in Table VII, the dynamic pre-exponential factors tend to decrease with increasing degree of degradation.

TABLE VII. Pre-exponential fdactors calculated from the Arrhenius plot obtained from dynamic thermogravimetry for different degrees of degradation

	$\log A_{DYN}$		
α	0.025	0.05	0.10
wbPUR1–Control	9.16	6.24	6.06
wbPUR1–MnCAT (2 %)	9.98	6.69	6.69
wbPUR1–ZrCAT (2 %)	9.96	6.68	6.49
wbPUR1–MnCAT (4 %)	10.13	6.72	6.53
wbPUR1–ZrCAT (4 %)	10.14	6.75	6.62
wbPUR2–Control	11.84	6.59	7.03
wbPUR2–MnCAT (2 %)	13.29	7.70	7.73
wbPUR2–ZrCAT (2 %)	13.24	6.48	7.56
wbPUR2–MnCAT (4 %)	13.59	7.75	7.87
wbPUR2–ZrCAT (4 %)	13.44	7.57	7.73

Moreover, the pre-exponential factors evaluated by dynamic methods predict that wbPUR1 has a greater thermal stability than wbPUR2.

Hence, the activation energy is a more useful parameter for comparing the thermal stability of materials and is the dominant factor with respect to the pre-exponential factor.

Also results of the Könning hardness[5] and of the activation energy show that the wbPUR2 sample was more stable than wbPUR1.

The more selective catalyst favors the reaction between isocyanate and the polyol component. This increased the percent of urethanic bonds and degree of hardness in the films formed from two-component, waterborne polyurethane lacquers. The polyol Macrynal VSM 2521, based on the single step synthesis route, is superior in pot-life and hardness relating to the polyol Macrynal VSM 6299 based on multistep synthesis route.[22]

The obtained results show that the performances of the two component waterborne polyurethane coatings depend on the polymer structure of the polyols as well as of the selectivity of the employed catalyst.[23,24]

The addition of the selective catalyst and favoring the isocyanate–polyol reaction contribute to obtaining the greater hardness of the formed films, also showed higher thermo-oxidative stability.

Data – collection times

The total experimental times required to collect the TG data during the kinetics analysis of the degradation were compared by the dynamic method.

Tables VIII and IX show the times during the dynamic experiments at which degradations of 0.025, 0.05, and 0.10 had occurred; from each series, the activation energies and the pre-exponential factors were calculated using Eq. (3).

TABLE VIII. Total time required to attain various degrees of degradation during the dynamic thermo-oxidation of wbPUR1

Method	α Degradation	wbPUR1–Control/min	wbPUR1–ZrCAT 2 %/min	wbPUR1–MnCAT 2 %/min	wbPUR1–ZrCAT 4 %/min	wbPUR1–MnCAT 4 %/min
Dynamic from 30 °C	0.025	395.4	440.9	493.8	483.2	535.7
	0.05	546.7	584.7	640.2	629.8	685.4
	0.10	602.3	637.5	693.1	683.1	738.8
Dynamic from 100 °C	0.025	129.4	174.9	227.8	217.2	269.7
	0.05	280.7	318.7	374.2	363.8	419.4
	0.10	336.3	371.5	427.1	417.1	472.8

The total times for dynamic experiments, τ_{dyn}, for each degradation degree can be evaluated from the data reported in Tables III and IV, taking into consideration the temperature at which a certain degradation occurred, t_r, the heating rate, r (°C min^{-1}), and the starting temperature, t_s (30 or 100 °C), according to

$$\tau_{dyn} = \sum_{r=0.5}^{10} \frac{(t_r - t_s)}{r} \tag{4}$$

TABLE IX. Total time required to attain various degrees of degradation during the dynamic thermo-oxidation of wbPUR2

Method	α Degradation	wbPUR1–Control/min	wbPUR2–ZrCAT 2 %/min	wbPUR2–MnCAT 2 %/min	wbPUR2–ZrCAT 4 %/min	wbPUR2–MnCAT 4 %/min
Dynamic from 30 °C	0.025	453.5	496.9	572.1	539.8	596.0
	0.05	602.6	637.5	700.1	681.1	743.8
	0.10	658.2	689.8	753.5	735.4	799.3
Dynamic from 100 °C	0.025	187.5	230.9	306.1	273.8	330.0
	0.05	336.6	371.5	434.1	415.1	477.8
	0.10	392.2	423.8	487.5	469.4	533.3

For example, in the case of wbPUR1 – control (without catalyst), a degradation of 0.025 at 0.5 °C min^{-1} was reached at a temperature of 140 °C, taking into consideration the contributions of the various heating rates, the resulting total time was 395.4 min.

When MnCAT (2 % and 4 %) as more selective catalyst was used, the resulting total time was longer for all degrees of degradation.

Also, in case of the sample wbPUR2, a similar increase of the resulting total time was observed. This fact shows that the wbPUR1 sample was thermally less stabile than the sample wbPUR2.

CONCLUSIONS

Dynamic thermogravimetry was used to study the thermal stability of waterborne polyurethane materials. The dynamic method is quite time-consuming, especially for degradations up to 0.05, but it allows the examination of the highest percentage of weight loss until almost complete thermo-oxidation of the material. Different degradation stages could be observed using the derivative of the degree of degradation after dynamic experiments. According to the dynamic method, the activation energy was more useful to assess the thermal stability than the pre-exponential factor.

The waterborne polyurethanes (wbPUR2) based on polyol Macrynal 2521 component with the more selective catalyst (MnCAT) showed higher thermal stability and higher activation energies than the waterborne polyurethane (wbPUR1) based on polyol Macrynal 6299 component also with the more selective catalyst (MnCAT).

И З В О Д

ТЕРМООКСИДАТИВНА СТАБИЛНОСТ ВОДЕНИХ ПОЛИУРЕТАНА ИЗРАЧУНАТА ПОМОЋУ ДИНАМИЧКЕ МЕТОДЕ КОРИШЋЕЊЕМ КАТАЛИЗАТОРА РАЗЛИЧИТЕ СЕЛЕКТИВНОСТИ

СУЗАНА М. ЦАКИЋ, ГОРАН С. НИКОЛИЋ и ЈАКОВ В. СТАМЕНКОВИЋ

Технолошки факултет, Булевар Ослобођења 124, 16000 Лесковац, Србија

За израчунавање отпорности према термооксидацији водених полиуретана коришћена је термогравиметријска анализа. Водени полиуретани (wbPUR) са катализаторима различите селективности били су окарактерисани методом динамичког загревања. У динамичкој методи, биле су коришћене брзине загревања од 0,5; 1; 2; 5; и 10 °C min^{-1} у опсегу од 30 – 500 °C при чему су разматране деградације од 0,025; 0,05; и 0,10. Из Аренијусових графика, израчунате активационе енергије за водене полиуретане кретале су се између 50 и 120 kJ mol^{-1} зависно од температурног интервала, селективности катализатора и степена деградације. Водени полиуретани без катализатора су показали нижу термичку стабилност од водених полиуретана са катализаторима различите селективности. Приказана динамичка метода указује на присуство различитих деградационих процеса, и она је погодна за израчунавање кинетичких параметара код високих степена деградације.

(Примљено 11. јануара 2006, ревидирано 12. марта 2007)

REFERENCES

1. E. Brinkman, P. Vandevoorde, *Progr. Org. Coatings* **34** (1997) 21
2. W. J. Blank, Z. A. He, E. T. Hessell, *Progr. Org. Coatings* **35** (1999) 19
3. Z. A. He, W. J. Blank, M. E. Picci, *J. Coatings Technol.* **74** (2002) 31

4. J. Stamenković, S. Cakić, G. Nikolić, *Hem. Ind.* **57** (2003) 559
5. J. Stamenković, S. Cakić, S. Konstantinović, S. Stoilković, *Facta Univer.* **2** (2004) 243
6. Z. S. Petrović, Z. Zavargo, *J. Appl. Polym. Sci.* **32** (1986) 4353
7. A. Jimenez, V. Berenguer, J. Lopez, A. Sanchez, *J. Appl. Polym. Sci.* **50** (1993) 1565
8. Z. S. Petrović, Z. Zavargo, J. H. Flynn, W. MacKnight, *J. Appl. Polym. Sci.* **51** (1994) 1087
9. B. L. Denq, W. Y. Chiu, K. F. Lin, *J. Appl. Polym. Sci.* **66** (1997) 1855
10. A. Pegoretti, A. Penati, J. Kolarik, *J. Therm. Anal.* **41** (1944) 1441
11. L. Fambri, A. Pegoretti, J. Kolarik, C. Gavazza, A. Penati, *J. Therm. Anal.* **52** (1998) 789
12. J. W. Park, S. C. Oh, H. P. Lee, T. K. Hee, K. O. Yoo, *Polym. Degrad. Stab.* **67** (2000) 535
13. J. H. Flynn, *J. Therm. Anal.* **37** (1991) 293
14. L. Fambri, A. Pegoretti, C. Gavazza, A. Penati, *J. Appl. Polym. Sci.* **81** (2001) 1216
15. R. B. Barendregt, P. Berg, *Thermochim. Acta* **38** (1980) 181
16. A. Ballistreri, S. Foti, P. Maravigna, G. Montaudo, E. Scamperrino, *J. Polym. Sci. Polym. Chem. Ed.* **18** (1980) 1923
17. F. Gaboriaud, J. P. Vantelon, *J. Polym. Sci. Polym. Chem. Ed.* **20** (1982) 2063
18. F. E. Rogers, T. J. Ohlemiller, *J. Macromol. Sci. Chem., Part A.* **15** (1981) 169
19. R. D. A. Paulmer, C. S. Shah, M. J. Patni, M. V. Pandya, *J. Appl. Polym. Sci.* **43** (1991) 1953
20. A. K. Sircar, T. G. Lamond, *Rubber Chem. Technol.* **45** (1972) 329
21. K–KAT® XC–6212 a product of King Industries Inc. Norwalk, CT 06852, USA, *U.S. Patent* 5 846 897
22. B. Johann, W. Werner, "New Low VOC Acrylic Polyol Dispersionsfor Two-Component Polyurethane Coatings", 79th Annual Meeting of the FSCT", 5–7 November, Atlanta, 2001
23. S.Cakić, Č. Lačnjevac, Lj. Rašković, *Facta Univer.* **2** (2005) 393
24. S.Cakić, Č. Lačnjevac, M. Rajković, Lj. Rašković, J. Stamenković, *Sensors* **6** (2006) 536.